

University of St Andrews



Full metadata for this thesis is available in
St Andrews Research Repository
at:

<http://research-repository.st-andrews.ac.uk/>

This thesis is protected by original copyright

**FIRST PRINCIPLES HARTREE-FOCK
STUDIES OF
MANGANESE & TITANIUM OXIDES**



ELIZABETH ANN WILLIAMSON

**SUBMITTED TO THE UNIVERSITY OF ST. ANDREWS AS PART OF THE
REQUIREMENT FOR THE DEGREE OF DOCTOR OF PHILOSOPHY IN THE FACULTY
OF SCIENCE, DEPARTMENT OF CHEMISTRY**

OCTOBER 1997



In submitting this thesis to the University of St. Andrews I understand that I am giving permission for it to be made available for use in accordance with the regulations of the University Library for the time being in force, subject to any copyright vested in the work not being affected thereby. I also understand that the title and abstract will be published, and that a copy of the work may be made and supplied to any *bona fide* library or research worker.

date

signature of candidate

Acknowledgements

I would principally like to thank my supervisor, Dr. William C. Mackrodt, for his continuous guidance, patience and enthusiasm throughout this work. I would also like to thank Dr. Neil L. Allan and Dr. Nicholas M. Harrison for their valuable collaborations. Thanks must also be extended to Jim Bews and Carol Jackson who provided prompt and reliable technical support in times of need.

On a more personal note, I would like to thank my husband, Paul, for his support and understanding over the course of this Ph.D. and also Susan Blake, Joanne Rankin and Maryjane Tremayne for making my time in St. Andrews very enjoyable.

For financial support, I must thank the University of St. Andrews, School of Chemistry for the award of a studentship and also the former Polar Solids Group of the Royal Society of Chemistry for the award of two bursaries.

Abstract

First principles periodic Hartree-Fock calculations have been carried out for the manganese oxides, MnO, MnO₂, LiMnO₂, MnFe₂O₄, including Li doped MnO and the first electron addition and first ionised states of MnO and MnO₂, in order to investigate the nature of the formal valence charge states of Mn. As part of a separate study of MnO, possible high pressure phases have been investigated in light of a recently observed phase transition at 90GPa. Calculations have also been carried out for TiO₂ rutile to investigate the surface structures and energetics of its low index surfaces and the electronic structure of its electron excess states.

Contents

Chapter 1	Introduction	1
Chapter 2	Theory and Computation	12
Chapter 3	The Electronic Structure And Magnetism Of The Hole And Electron Addition States In MnO	
3.1	Introduction	30
3.2	Results	31
3.2.1	<i>Neutral MnO</i>	31
3.2.2	<i>Hole states in MnO</i>	33
3.2.3	<i>Li:MnO</i>	44
3.2.4	<i>Electron addition states in MnO</i>	52
3.3	Discussion	53
3.4	Conclusions	56
Chapter 4	MnO at High Pressure	
4.1	Introduction	59
4.2	Results	60
4.2.1	<i>Low pressure phase</i>	60
4.2.2	<i>High pressure phase</i>	62
4.3	Discussion	69
4.4	Conclusions	72
Chapter 5	The Valence Charge States In MnO₂ Rutile	
5.1	Introduction	74
5.2	Results	74
5.2.1	<i>Ground state of MnO₂</i>	74
5.2.2	<i>First ionised state of MnO₂</i>	79
5.2.3	<i>First electron addition state of MnO₂</i>	81
5.3	Discussion	84
5.4	Conclusions	86

Chapter 6	The Electronic Structure Of Monoclinic C2/m Li_xMnO_2	
	($1 \leq x \leq 0$)	
6.1	Introduction	88
6.2	Results	89
6.2.1	LiMnO_2	89
6.2.2	Li_xMnO_2 ($x < 1$)	94
6.3	Discussion	97
6.4	Conclusions	101
Chapter 7	The Cation Valence Charge States In MnFe_2O_4	
7.1	Introduction	103
7.2	Results	103
7.3	Discussion	111
7.4	Conclusions	112
Chapter 8	The Non Defective Surfaces Of TiO_2 Rutile	
8.1	Introduction	114
8.2	Results	115
8.3	Discussion	123
8.4	Conclusions	126
Chapter 9	The Electron Excess Gap States in TiO_2 Rutile	
9.1	Introduction	128
9.2	Results	130
9.2.1	<i>Non defective bulk</i>	130
9.2.2	<i>Non defective {110}, {100} and {001} surfaces</i>	131
9.2.3	<i>One electron addition</i>	132
9.2.4	<i>Two electron addition</i>	136
9.2.5	<i>Oxygen deficient bulk and surface</i>	138
9.3	Discussion	141
9.4	Conclusions	144
Appendix		147
Publications		152

Chapter 1

Introduction

The first *ab initio* periodic Hartree-Fock study in this area of magnetic oxides was in 1993 with an investigation of the ground state properties of VO, MnO and NiO compared with the non magnetic oxide CaO¹ using the CRYSTAL² suite of programs, which included for the first time the spin unrestricted procedure (UHF) introduced into molecular calculations by Pople and Nesbit³. These transition metal oxides were all found to be high spin insulating and largely ionic in nature with Mulliken charges of $\pm 1.9e$, which is close to the formal charge of ± 2 . The 3d populations were also found to be close to the formal values of 3, 5 and 8 respectively, with local magnetic moments close to measured values. Full structural optimisations were carried out for all oxides by direct energy minimisation leading to calculated lattice parameters for CaO, MnO and NiO which were $\sim 2.5\%$ larger than the experimental values. This error of $\sim 2.5\%$ is similar to that found previously for a wider range of ionic and semi ionic oxides. The error in the lattice parameter of VO, however, was $\sim 10\%$ larger than the experimental value. This discrepancy was attributed to the fact that VO is highly defective with large concentrations of cation and anion vacancies and might also be non stoichiometric, neither of which were included in the calculations which were for the fully stoichiometric non defective material. The calculated densities of states (DOS) were examined as these provide additional information on the electronic structure. The calculated DOS of CaO corresponded closely to that of a classical ionic system, with a valence band of O(2p) states separated by an overestimated gap from the conduction band of mixed O and Ca states. It should be emphasised that all gaps between bands (levels) of unequal occupancy are overestimated in Hartree-Fock theory which is due to the inconsistent treatment of the self interaction. Thus Hartree-Fock calculations estimate correctly gaps between filled bands, notably those between the 2s and 2p and also those between empty bands. The calculated valence band structures of NiO, MnO and VO all differed from CaO in that their valence bands were not constructed solely from O(2p) states but had a significant contribution from M(3d) states (where

M= Ni, Mn, V). In the case of NiO and MnO though, the upper edges of their valence bands were found to be dominated by O(p) states while the VO upper edge was predominately V(3d). In view of these findings a preliminary investigation was also carried out into the nature of the hole states in these three transition metal oxides by substituting one of the metal atoms by a Li atom. For 25% Li substitution of the unrelaxed materials, Mulliken population analyses indicated that the hole states were all O(p) in nature, ie $d^5\bar{L}$. This was an unexpected result for VO as the states at the upper edge of the valence band were V(3d), so that assuming a rigid band model, hole states were expected to be d^2 . Therefore, it was concluded that this initial investigation into the nature of the hole states did not provide valid results due to the high Li concentration in the doping regime. However VO, NiO and MnO were all found to be high spin antiferromagnetic (AF) insulators in complete agreement with experiment.

This first study led to a subsequent paper by Towler *et al*⁴ which investigated non defective MnO and NiO in more detail. Towler *et al*⁴ confirmed the findings of the initial investigation, namely that, MnO and NiO are high spin insulators, but with an antiferromagnetic, AF₂, spin arrangement, which consists of alternate ferromagnetic (FM) {111} planes aligned antiferromagnetically in the solid. This AF₂ spin arrangement is also known to give rise to a spin lattice interaction or a magnetostriction effect which results in a rhombohedral contraction normal to the FM planes. This distortion, in terms of the change in cubic angle, was estimated by Towler *et al*⁴ to be 0.47° and 0.075° for MnO and NiO respectively, which compared with values of 0.62° and 0.1° found experimentally. The elastic and vibrational properties of MnO and NiO were also investigated and found to be in reasonable agreement with experiment, where data of sufficient quality was available. Apart from confirming the essentially ionic high spin insulating nature of VO, MnO and NiO, this original work provided indirect evidence for the nature of valence band holes in these systems, which following the discovery of high temperature superconductivity, had become an area of intense experimental and theoretical interest. This early work on NiO was followed up two years later by two papers. The first of these presented for the first time direct evidence that valence band holes in Li doped NiO (Li:NiO) at doping levels of 12.5% and 25%

Li were O(2p) in nature⁵. The second paper⁶, also provided direct evidence that the first ionised state of undoped NiO was essentially $d^5\bar{L}$ but that the first ionised state of Fe doped NiO consisted essentially of Fe(3d), as deduced by Springhorn and Schmalzried⁷ from their conductivity measurements. The direct evidence which supported these findings came from the charge and spin density distributions projected onto a suitable plane of the doped materials. Unlike the Mulliken charge populations which are arbitrary, although reasonably defined, charge and spin density distributions are obtained directly from the wavefunction. However, in both cases the results of Mulliken charge and spin population analyses were entirely consistent with the charge and spin density distributions. Further direct evidence also came from a comparison of the atom projected densities of unoccupied states of non defective NiO and the first ionised or Li doped systems. The creation of a hole leads to new unoccupied states, which when projected onto Ni and O are shown to consist entirely of O(p) states exactly as predicted from Mulliken population analyses and the charge and spin distributions. The band gap in NiO was estimated as the gap between the new empty O(p) states at the upper valence band edge and the lower edge of the conduction band, giving a value of $\sim 3.5\text{eV}$, which compared with the experimental value of 3.7eV .

Moving away from calculations of defect states, there followed three quite distinct *ab initio* periodic Hartree-Fock investigations of NiO solid solutions with MgO, two of which included MnO/MgO solid solutions. The first, by Heath *et al*⁸, was concerned with the calculation of the enthalpies of mixing of NiO/MgO and of MnO/MgO. From this study, which combined electronic structure and lattice free energy calculations, it was suggested that while positive enthalpies of mixing, such as that for MnO/MgO, were amenable to direct calculation by both methods, the unique case of NiO/MgO with a negative enthalpy of mixing, required electronic structure methods to account for the subtle changes of electronic structure that are responsible for the negative deviation from ideality. The second of these studies by Towler *et al*⁹ used the CRYSTAL program to calculate the equilibrium surface geometries and electronic properties of NiO/MgO thin films. The third investigation, also by Towler *et al*¹⁰, was

concerned with the electronic structure and in particular the single particle DOS of solutions of the type, $M_xMg_{1-x}O$ (where $M=Ni, Mn$) as a function of x . The densities of M states were found to be largely unaffected by concentration up to MO , with such changes that did occur being of the same order of magnitude as those associated with changes in the magnetic state. From these results it was suggested that independent ion behaviour characterises the electronic properties of NiO and that Hartree-Fock theory predicts the correct ground state properties of magnetic insulators such as this because the important onsite Coulombic interactions of essentially localised electrons are described correctly.

Catti and coworkers^{11, 12} then reported UHF calculations of the trivalent magnetic oxides, $\alpha-Fe_2O_3$ ¹¹ and Cr_2O_3 ¹², both of which have the corundum structure. In the study of $\alpha-Fe_2O_3$ the effects of basis set type were investigated by a comparison of the optimised structural parameters derived from two different basis sets. The first was an all electron basis of the type previously used for $\alpha-Al_2O_3$ ¹³, MnO and NiO ; the second was a valence only set in conjunction with the large core Durand-Barthélat pseudopotentials. Three structural variables, which consisted of the ratio of lattice constants, c/a , the z coordinate of the Fe atom, $z(Fe)$, and the x coordinate of the O atom, $x(O)$, were optimised for a number of fixed volumes ranging from -10% to +8% of the experimental volume. The optimised values were found to vary linearly with the change in volume. The optimisation was done in this way in order to observe the effect of pressure on the lattice structure. Although the structural parameters, so calculated, depend on the volume, they can be transformed to a pressure dependence by differentiation of the Hartree-Fock energy with respect to the volume ($p=-dE/dV$). The pressure dependence of the structural parameters was plotted and from the c/a ratio versus pressure dependence, it was deduced that $\alpha-Fe_2O_3$ was more compressible than isostructural $\alpha-Al_2O_3$ ¹³ studied previously. For the calculated zero pressure, or equilibrium values, it was found that better agreement between experimental and computed structural parameters was obtained from the all electron basis. However the errors in the lattice parameters from the valence only set were still within the usual 2.5%, typical of UHF calculations. For $\alpha-Fe_2O_3$, the $R\bar{3}$ AF spin arrangement was calculated to be the most stable, in agreement with

experiment, and 0.036eV lower in energy than the FM state. The AF state, which is stabilised through superexchange interactions, is highly sensitive to the Fe-O-Fe bond angles, which the all electron basis set calculates to within 1% of their experimental values. From the calculated DOS α -Fe₂O₃ is predicted to be a wide band gap insulator, with a band gap which is spanned by O(p) states at the upper valence band edge and Fe(d) states at the lower edge of the conduction band. This investigation concluded that α -Fe₂O₃ is more covalent than MnO and NiO but slightly more ionic than α -Al₂O₃¹³.

The other magnetic sesquioxide to be investigated was Cr₂O₃¹² and it was found to have a different ground state antiferromagnetic spin arrangement from α -Fe₂O₃. All electron basis set calculations predicted the R3c AF spin configuration to be the most stable, which was in complete agreement with experiment. Overlap population analyses suggested that Cr₂O₃ is much more of a covalent system than α -Fe₂O₃. The effect of pressure on the lattice structure was investigated as before from which plots of a/a_0 , c/c_0 , V/V_0 and $(c/a)/(c_0/a_0)$ versus pressure, where V is volume and the subscript indicates the equilibrium values, were in good agreement with experimental data over the common pressure range. It was also predicted from the pressure dependence of the c/a ratio that Cr₂O₃ was less compressible than α -Fe₂O₃.

The geometry of the basal {0001} surface of Cr₂O₃ was investigated in a separate study¹⁴ by direct energy minimisation of a six layer infinite two dimensional slab. Structural optimisations using the FM and AF spin arrangements resulted in geometries which were practically identical, with differences in displacements of less than 0.002Å. However, the AF spin arrangement was still lower in energy. The charge of the central Cr was monitored during relaxation and only very small changes, less than 0.01e, were found from the bulk value. Overall then, large inward relaxations of the surface Cr ions were observed which reduced the surface energy from 9Jm⁻² to 3Jm⁻².

The UHF method has been shown to deal effectively with degenerate open shell systems, where, in order to achieve the ground state solution of the Hartree-Fock equations, the degeneracies of the orbitals must be removed. The first such study which confirmed this was carried out on the magnetic fluoride rutile, FeF₂¹⁵. The

electronic configuration of the d orbitals of Fe^{2+} is $t_{2g}^4 e_g^2$ which requires a distortion to remove the degeneracy of the t_{2g} orbitals to give an insulating state. Prior to this investigation, only MnO, NiO and VO magnetic oxides had been studied¹, all of which have non degenerate t_{2g} and e_g filled states. The FeF_2 investigation predicted an optimised structure with a Jahn Teller distortion of the FeF_6 octahedra. The calculated distortion was in good agreement with experiment, with two Fe-F bond lengths calculated as 2.052Å and 2.148Å, which compared with the experimental values of 2.003Å and 2.117Å respectively. The AF spin arrangement of FeF_2 was found to be lower in energy than the FM arrangement which is also in agreement with experiment. The Mulliken charges of FeF_2 were found to be very close to that in MgF_2 with the calculated spin moment on Fe of $3.93\mu_B$, which compares with the experimental value of $3.75\mu_B$. All of the fundamental electronic properties of FeF_2 were predicted correctly including the d-d gap and the Jahn Teller distortion of the FeF_6 octahedra.

Other magnetic fluorides with more complex structures have been investigated. The first of these was KNiF_3 perovskite¹⁶, then in a parallel paper, K_2NiF_4 ¹⁷ with a structure similar to La_2CuO_4 , and finally KCuF_3 perovskite¹⁸. The ground state magnetic properties of all of these fluorides were correctly predicted by the *ab initio* periodic Hartree-Fock program, CRYSTAL. They were all confirmed as highly ionic, insulating materials with wide band gaps and AF spin arrangements. In all cases, the superexchange interactions were investigated in detail. The calculated distortion found in KCuF_3 , resulting from the d^9 electronic configuration of Cu^{II} , was estimated in close agreement with the Jahn Teller distortion found from experimental structure determination.

Moving away from fluorides and returning once again to magnetic oxides and, in particular, to two studies which have been carried out on systems which contain heavy metal ions, which necessitate the use of pseudopotentials to represent the inner cores, tungsten trioxide, WO_3 ¹⁹, and molybdenum trioxide, αMoO_3 ²⁰. The purpose of these calculations was to determine the structural and ground state electronic properties of these oxides. Tungsten trioxide is constructed from corner sharing octahedra, WO_6 , which are distorted such that W is shifted from its lattice position at the centre of the octahedra, towards one oxygen atom,

resulting in a stable tetragonal phase. Although the cubic phase of WO_3 had not been observed experimentally, both the hypothetical cubic and tetragonal phases of WO_3 were investigated. The stabilisation of the tetragonal phase was then attributed to the fact that as the W was displaced from its central position in the hypothetical cubic structure the bond between it and the nearest neighbour oxygen became more covalent. This resulted in an energy difference of 0.8eV between the cubic and tetragonal phases. Even when the tetragonal phase was put under pressure by a reduction in the unit cell volume, it still remained the most stable phase. Although $\alpha\text{-MoO}_3$ is also constructed from distorted MoO_6 octahedra, it exists in a symmetry reduced orthorhombic structure. Mo ions are displaced from their central octahedral position but this time in a slightly different direction, towards two of the six surrounding oxygen atoms. Optimisation of the structural parameters gave values which were in good agreement with those determined experimentally. It was found that $\alpha\text{-MoO}_3$ is similar to WO_3 in that Mo forms a strong covalent bond with a single O atom of the surrounding octahedra, which is even stronger than that previously observed in WO_3 . This study also predicted that $\alpha\text{-MoO}_3$ is insulating as opposed to the semiconducting behaviour of WO_3 .

Another further study involving a heavy metal and the use of core pseudopotentials was carried out by Harrison *et al*²¹ on PbS. The purpose of this study was to investigate the effect of various approximations on the structural properties of rocksalt PbS. In this investigation, four different types of pseudopotential were employed in combination with two different optimised valence electron basis sets for Pb and the all electron basis sets of S. The effect of these combinations was assessed by comparing the subsequent optimised structural parameters with the corresponding experimental values. It was found that variation in the pseudopotentials produced large differences in the calculated lattice parameter and bulk modulus, whereas varying the basis set apparently made very little difference to these calculated values. From the Mulliken population analyses it was concluded that PbS was fairly ionic with Mulliken charges of $\pm 1.8e$. This was confirmed by the atom projected DOS which showed the effect of very weak covalency due to the hybridisation of Pb 6s and 6p bands

with the S 3p band. The calculated DOS was in acceptable agreement with an ultra-violet photoelectron spectrum which revealed the width of the Pb 6p and S 3p peaks as 6.0eV which compared with calculated values of 5.9eV and 6.4eV respectively.

From this wide range of studies it is evident that *ab initio* spin unrestricted periodic Hartree-Fock calculations as implemented in the CRYSTAL code provide an accurate description of the ground state electronic and magnetic properties of ionic and partially ionic systems. The major reason for this is the exact treatment of both the onsite and non local exchange. The former is largely responsible for the essentially localised nature of the d electrons in the first row transition metal oxides, while the latter is responsible for the prediction of the correct AF states which are stabilised by superexchange. A further important reason for the success of the CRYSTAL program is the very high level of numerical accuracy, without which the identification of different magnetic states would be impossible.

The results of chapter 3 follow naturally from the investigation into the defect states of NiO, as a detailed investigation of the electronic structure and magnetism of the free and Li bound hole states and of the electron addition states in MnO is presented. Chapter 4 is concerned with an investigation of the high pressure properties of MnO in view of the recently observed phase transition at 90GPa which has been suggested as being B1-B2. Previously there have been a number of successful Hartree-Fock high pressure studies on MgO²², CaO²³ and SrO²⁴. The phase transition pressures which were calculated for CaO and SrO, 68GPa and 42GPa respectively were in good agreement with the experimental values of ~60GPa and ~36GPa. More recently, Hartree-Fock calculations have been carried out to determine the phase transition pressures of the alkali halides and alkaline earth oxides²⁵, with pressures found close to the measured values. Chapters 5, 6 and 7 evolve directly from chapter 3 and are concerned with the valence state of Mn in higher oxides. Chapters 8 and 9 address the rutile phase of TiO₂, which has recently been the subject of much experimental investigation. In chapter 8 the relaxed surface geometries are investigated while chapter 9 focuses

on the electronic structure of both the stoichiometric and non stoichiometric surfaces and bulk material.

References

1. W.C.Mackrodt, N.M.Harrison, V.R.Saunders, N.L.Allan, M.D.Towler, E.Aprà and R.Dovesi, *Philosophical Magazine A*, 1993, **68**(4), 653
2. R.Dovesi, V.R.Saunders and C.Roetti, M.Causà, N.M.Harrison, R.Orlando and E.Aprà, *CRYSTAL 95, User Manual* (Università di Torino and CCLRC Daresbury Laboratory, 1995)
3. J.A.Pople and R.K.Nesbet, 1954 *J.Chem.Phys.* **22**, 571
4. M.D.Towler, N.L.Allan, N.M.Harrison, V.R.Saunders, W.C.Mackrodt and E.Aprà, *Physical Review B*, 1994, **50**(8), 5041
5. W.C.Mackrodt, N.M.Harrison, V.R.Saunders, N.L.Allan, M.D.Towler, *Chemical Physics Letters*, 1996, **250**, 66
6. W.C.Mackrodt, *Ber. Bunsenges. Phys. Chem*, 1997, **101**, 169
7. C.Springhorn and H.Schmalzried, 1994 *Ber. Bunsenges. Phys. Chem.* **98**, 746
8. K.D.Heath, W.C.Mackrodt, V.R.Saunders, M.Causa, *Journal of Materials Chemistry*, 1994, **4**(6), 825
9. M.D.Towler, N.M.Harrison, M.I.McCarthy, *Physical Review B*, 1994, **52**(7), 5375
10. M.D.Towler, N.L.Allan, N.M.Harrison, V.R.Saunders and W.C.Mackrodt *Journal of Physics: Condensed Matter*, 1995, **7**, 6231
11. M.Catti, G.Valerio and R.Dovesi, *Physical Review B*, 1995, **51**(12), 7441
12. M.Catti, G.Sandrone, G. Valerio and R.Dovesi, *Journal of Physics and Chemistry of Solids*, 1996, **57**(11), 1735
13. L.Salasco, R.Dovesi, R.Orlando, M.Causà and V.R.Saunders, *Molecular Physics*, 1991, **72**(2), 267
14. C.Rehbein, N.M.Harrison and A.Wander, *Physical Review B*, 1996, **54**(19), 14066
15. G.Valerio, M.Catti, R.Dovesi and R.Orlando, *Physical Review B*, 1995, **52**(4), 2422
16. J.M.Ricart, R.Dovesi, C.Roetti and V.R.Saunders, *Physical Review B*, 1995, **52**(4), 2381

17. R.Dovesi, J.M.Ricart, V.R.Saunders and R.Orlando, *Journal of Physics: Condensed Matter*, 1995, **7**, 7997
18. M.D.Towler, R.Dovesi and V.R.Saunders, *Physical Review B*, 1995, **52**(14), 10150
19. F.Corà, A.Patel, N.M.Harrison, R.Dovesi and C.R.A.Catlow, *Journal of the American Chemical Society*, 1996, **118**, 12174
20. F.Corà, A.Patel, N.M.Harrison, C.Roetti and C.R.A.Catlow, *Journal of Materials Chemistry*, 1997, **7**(6), 959
21. M.Mian, N.M.Harrison, V.R.Saunders and W.R.Flavell, *Chemical Physics Letters*, 1996, **257**, 627
22. M.Causà, R.Dovesi, C.Pisani, and C.Roetti, *Physical Review B*, 1986, **33**, 1308
23. P.D'Arco, L-H.Jolly, and B.Silvi, *Phys.Earth and Planetary Interiors*, 1992, **72**, 286
24. A.Zupan, I.Petek, M.Causà, and R.Dovesi, *Phys.Rev. B*, 1993, **48**, 799
25. C.E.Sims, G.D.Barrera, N.L.Allan, and W.C.Mackrodt, 1997 - To be submitted

Chapter 2

Theory and Computation

This chapter outlines the basic equations, approximations and simplifications used in Hartree-Fock theory with particular emphasis on its implementation in CRYSTAL¹, the linear combination atomic orbital (LCAO) self consistent field (SCF) periodic Hartree-Fock program, which has been used throughout this thesis.

The electronic structure of an N-electron system can be calculated if the fundamental problem of finding a solution to the N-electron Schrödinger equation,

$$H(1, \dots, N)\Psi(1, \dots, N) = E\Psi(1, \dots, N) \quad 2.1$$

in which N electrons move in the Coulombic field of M nuclei with charges of $\{Z_A\}$, can be overcome. If for the system under investigation the Born-Oppenheimer approximation is assumed to be valid, $H(1, \dots, N)$ is given by

$$H = \sum_i^N \left\{ -\frac{1}{2} \nabla_i^2 - \sum_A^M \frac{Z_A}{|\mathbf{r}_i - \mathbf{R}_A|} + \sum_{j>1}^N \frac{1}{|\mathbf{r}_i - \mathbf{r}_j|} \right\} \quad 2.2$$

in atomic units, where $\{\mathbf{r}_i\}$ and $\{\mathbf{R}_A\}$ are the electronic and fixed nuclear coordinates respectively. The N electron wavefunction, $\Psi(1, \dots, N)$, is then functionally dependent on $\{\mathbf{r}_i\}$ and parametrically dependent on $\{\mathbf{R}_A\}$. The kinetic and nuclear attraction energies are represented by the one electron terms while the two electron term represents the repulsive interaction between the electrons.

Any attempt to find a solution to the N particle Schrödinger equation must involve a fundamental approximation to $\Psi(1, \dots, N)$ as its exact functional form is unknown. In reality the only approximation which can be used with any generality is the single particle approximation, where it is assumed that the N electron wavefunction can be written as a product of N single particle functions, $\{\Psi_i\}$,

$$\Omega(1, \dots, N) \equiv \Omega[\{\psi_i\}] \quad 2.3$$

A general form of $\Omega(1, \dots, N)$ is

$$\Omega(1, \dots, N) = \sum_k C_k \Phi_k \quad 2.4$$

where Φ_k is a determinantal function of $\{\psi_i\}$ and as a result of the requirement that the total wavefunction must be antisymmetric with respect to the interchange or permutation of any two electrons,

$$\Phi_k = \hat{A} \prod_i^k \psi_i \quad 2.5$$

The most general definition of the Hartree-Fock approximation is that it is the best single determinant of single particle functions, Φ_0 , to which $\Omega(1, \dots, N)$ approximates. The variational principle is used to determine Φ_0 , where the expectation value of $H(1, \dots, N)$ is varied with respect to Φ_0 until a minimum is obtained, ie

$$\min\{W\} = \min\{\langle \Phi_0 | H(1, \dots, N) | \Phi_0 \rangle\} \quad 2.6$$

subject to the orthonormality constraint

$$\langle \Phi_0 | \Phi_0 \rangle = N \quad 2.7$$

$\min\{W\}$ is obtained from

$$\frac{\partial W}{\partial \Phi_0} = 0 \quad 2.8$$

As Φ_0 is given by

$$\Phi_0 = \hat{A} \prod_i \psi_i \quad 2.9$$

the single extremum,

$$\frac{\partial W}{\partial \Phi_0} = 0 \quad 2.10$$

is replaced by N coupled extrema

$$\frac{\partial W}{\partial \psi_i} = 0 \quad \text{for all } i \quad 2.11$$

subject to the orthonormality constraints

$$\langle \psi_i | \psi_j \rangle = \delta_{ij} \quad 2.12$$

Thus equations 2.11 and 2.12 contain the Hartree-Fock equations in their most general form.

Equations 2.2 and 2.9 for $H(1, \dots, N)$ and Φ_0 respectively lead to an expression for W given by

$$W = \sum_{i=1}^N \left\{ h_i + \sum_{i < j}^N J_{ij} - K_{ij} \right\} \quad 2.13$$

The one electron terms, h_i , are of the form

$$h_i = \langle \psi_i | \hat{h}_i | \psi_i \rangle \quad 2.14$$

$$h_i = \left\langle \psi_i \left| -\frac{1}{2} \nabla_i^2 - \sum_A^M \frac{Z_A}{|r_i - R_A|} \right| \psi_i \right\rangle \quad 2.15$$

$$= \int d\tau(1) \psi_i^*(1) \left\{ -\frac{1}{2} \nabla_i(1) - \sum_A^M \frac{Z_A}{|r_i - R_A|} \right\} \psi_i(1) \quad 2.16$$

where (1) denotes that the integral is over the total coordinates of electron (1).

The two electron terms, J_{ij} and K_{ij} are given by

$$J_{ij} = \left\langle \psi_i \psi_j \left| \frac{1}{r_{ij}} \right| \psi_i \psi_j \right\rangle \quad 2.17$$

$$= \iint d\tau(1) d\tau(2) \psi_i^*(1) \psi_j^*(2) \left| \frac{1}{r_{ij}} \right| \psi_i(1) \psi_j(2) \quad 2.18$$

and

$$K_{ij} = \left\langle \psi_i \psi_j \left| \frac{1}{r_{ij}} \right| \psi_j \psi_i \right\rangle \quad 2.19$$

$$= \iint d\tau(1) d\tau(2) \psi_i^*(1) \psi_j^*(2) \left| \frac{1}{r_{ij}} \right| \psi_i(2) \psi_j(1) \quad 2.20$$

The N electron Hamiltonian as represented in equation 2.2 does not contain any explicit spin-dependency, ie there are no spin orbit terms. Therefore, the single particle functions, ψ_i , which are formally functions of space and spin variables, can be separated into space only, ϕ_i , and spin only, σ_i functions,

$$\psi_i = \phi_i \times \sigma_i \quad 2.21$$

with separate orthonormality constraints,

$$\langle \phi_i | \phi_j \rangle = \delta_{ij} \quad 2.22$$

$$\langle \sigma_i | \sigma_j \rangle = \delta_{ij} \sigma_j \quad 2.23$$

Equation 2.22 implies a definable, unspecified type of integral over unspecified spin variables. Now, h_i , J_{ij} , and K_{ij} are given by

$$h_i = \langle \phi_i | \hat{h}_i | \phi_i \rangle \quad 2.24$$

$$J_{ij} = \left\langle \phi_i \phi_j \left| \frac{1}{r_{ij}} \right| \phi_i \phi_j \right\rangle \quad 2.25$$

$$K_{ij} = \left\langle \phi_i \phi_j \left| \frac{1}{r_{ij}} \right| \phi_j \phi_i \right\rangle \delta_{\sigma_i \sigma_j} \quad 2.26$$

The Coulomb and exchange operators, \hat{J}_j and \hat{K}_j can be defined as

$$\hat{J}_j(2)\chi(1) = \left(\int d\tau(2) \frac{|\phi_j(2)|^2}{r_{12}} \right) \chi(1) \quad 2.27$$

and

$$\hat{K}_j(2)\chi(1) = \left(\int d\tau(2) \frac{\phi_j^*(2)\chi(2)}{r_{12}} \right) \phi_j(1) \quad 2.28$$

the expectation values of which are conventionally used to express J_{ij} and K_{ij} .

Thus W can now be written in the form

$$W = \sum_{i=1}^N \left\{ h_i + \sum_{i>j} [J_{ij} - K_{ij}\delta_{\sigma_i\sigma_j}] \right\} \quad 2.29$$

$$= \sum_i \left\langle \phi_i \left| \hat{h}_i + \sum_{i>j} [\hat{J}_j - \hat{K}_j\delta_{\sigma_i\sigma_j}] \right| \phi_i \right\rangle \quad 2.30$$

$$= \sum_i \left\langle \phi_i | \hat{F}_i | \phi_i \right\rangle \quad 2.31$$

$$= \sum_i \hat{F}_i \quad 2.32$$

where \hat{F}_i is the Fock operator given by

$$\hat{F}_i = \hat{h}_i + \sum_{i>j} (\hat{J}_j - \hat{K}_j\delta_{\sigma_i\sigma_j}) \quad 2.33$$

and since $J_{ii} = K_{ii}$ for all i ,

$$\hat{F}_i = \hat{h}_i + \sum_j (\hat{J}_j - \hat{K}_j\delta_{\sigma_i\sigma_j}) \quad 2.34$$

Equations 2.11 and 2.12 can now be written as

$$\frac{\partial W}{\partial \psi_i} = \partial \sum_i \left\langle \phi_i | \hat{F}_i | \phi_i \right\rangle = 0 \quad 2.35$$

subject to

$$\sum_i \left\langle \phi_i | \phi_i \right\rangle = \delta_{ij} \text{ for all } i, j \quad 2.36$$

which, on applying the method of Lagrange multipliers can then be written as

$$= \sum_i \left\{ \left(\left\langle \delta\phi_i \left| \hat{F}_i - \sum_j \epsilon_{ij} \right| \phi_j \right\rangle \right) + \left(\left\langle \delta\phi_i \left| \hat{F}_i - \sum_j \epsilon_{ji} \right| \phi_j \right\rangle^* \right) \right\} = 0 \quad 2.37$$

which gives

$$\hat{F}_i \phi_i = \sum_j \epsilon_{ij} \phi_j \quad 2.38$$

$$\hat{F}_i \phi_i = \sum_j \epsilon_{ji}^* \phi_j \quad 2.39$$

for a set of completely independent variables, $\delta\phi_i$.

As $\epsilon \{ \epsilon_{ij} \}$ can be chosen such that it is Hermitian, equations 2.38 and 2.39 are identical and, on applying a unitary transformation, can be reduced further to give the canonical Hartree-Fock equations,

$$\hat{F}_i \phi_i = \epsilon_i \phi_i \quad 2.40$$

Therefore the optimum set of single particle functions, $\{ \phi_i \}$, are eigenfunctions of the N-particle Fock operator. For atoms the radial Hartree-Fock equations can be derived from equation 2.40 and solved exactly by numerical integration, first carried out by Hartree², as ϕ_i can be separated into radial and spherical components,

$$\phi_i = R_{il}(r) Y_{ml}(\theta, \varphi) \quad 2.41$$

For molecules and solids, however, the corresponding three dimensional integro-differential equations cannot be evaluated numerically and therefore a further approximation is required, the LCAO approximation, where ϕ_i are expressed as linear combinations of atomic orbitals, $\{ \varphi_r \}$, which are centred at the nuclear positions

$$\phi_i = \sum_r c_{ir} \varphi_r \quad 2.42$$

or

$$\phi = \mathbf{c}\varphi \quad 2.43$$

The problem has now changed from determining a set of eigenfunctions, $\{\phi_i\}$, of the Fock operator to finding the set of expansion coefficients, $\{c_{ir}\}$ or \mathbf{c} . Roothaan³ was the first to formulate the Hartree-Fock equations in terms of $\{c_{ir}\}$ or \mathbf{c} in compact matrix notation, an outline of which follows here with a slight variation based on the single particle density matrix.

The density matrix, \mathbf{P} , is defined by

$$\mathbf{P} = \mathbf{C}\mathbf{C}^\dagger \text{ or } P_{rs} = \sum_{i=1}^N C_{ri}C_{is}^* \quad 2.44$$

which on differentiation gives,

$$\delta P_{rs} = \sum_i \left(\delta C_{ri}C_{is}^* + C_{ri}\delta C_{is}^* \right) \quad 2.45$$

For closed shell systems with $2N$ electrons, the total energy can be written as,

$$E = 2 \sum_{i=1}^N \left\langle \phi_i \left| \hat{h}_i + \hat{J}_i - \frac{1}{2} \hat{K}_i \right| \phi_i \right\rangle \quad 2.46$$

which on substituting for ϕ_i , (equation 2.42) and invoking equation 2.44 can be written as

$$E = \text{Tr}\mathbf{P}\mathbf{h} + \frac{1}{2} \text{Tr}\mathbf{P}\mathbf{G}[\mathbf{P}] \quad 2.47$$

In this notation, \mathbf{h} represents the matrix of monoelectronic energies and \mathbf{G} the matrix of bielectronic interaction energies which is a functional of the density matrix, \mathbf{P}

$$\mathbf{G}[\mathbf{P}]_{rs} = \mathbf{J}[\mathbf{P}]_{rs} - \frac{1}{2} \mathbf{K}[\mathbf{P}]_{rs} \quad 2.48$$

where the matrix representations of the Coulomb and exchange operators are $\mathbf{J}[\mathbf{P}]$ and $\mathbf{K}[\mathbf{P}]$ shown below.

$$\mathbf{J}[\mathbf{P}]_{rs} = \sum_{t,u} P_{tu} \iint dr_1 dr_2 \varphi_r^*(r_1) \varphi_u^*(r_2) \frac{1}{r_{12}} \varphi_s(r_1) \varphi_t(r_2) \quad 2.49$$

$$\mathbf{K}[\mathbf{P}]_{rs} = \sum_{t,u} P_{tu} \iint dr_1 dr_2 \varphi_r^*(r_1) \varphi_u^*(r_2) \frac{1}{r_{12}} \varphi_t(r_1) \varphi_s(r_2) \quad 2.50$$

Variation of the coefficients results in changes in the density matrix and total energy,

$$\delta\mathbf{P} = \delta\mathbf{C}\mathbf{C}^\dagger + \mathbf{C}\delta\mathbf{C}^\dagger \quad 2.51$$

$$\delta E = \text{Tr}\delta\mathbf{P}\mathbf{h} + \frac{1}{2} \text{Tr}\delta\mathbf{P}\mathbf{G}[\mathbf{P}] + \frac{1}{2} \text{Tr}\mathbf{P}\mathbf{G}[\delta\mathbf{P}] \quad 2.52$$

which simplifies to

$$\delta E = \text{Tr}\delta\mathbf{P}\mathbf{h} + \text{Tr}\delta\mathbf{P}\mathbf{G} \quad 2.53$$

or

$$\delta E = \text{Tr}\delta\mathbf{P}\mathbf{F} \quad 2.54$$

Substituting for \mathbf{P} (from equation 2.45) leads to

$$\delta E = \sum_{i,s} (\delta C_{ri} C_{is}^* + C_{ri} \delta C_{is}^*) F_{sr} \quad 2.55$$

$$= \sum_{i,s} (C_{is}^* F_{rs} \delta C_{ri} + \delta C_{is}^* F_{sr} C_{ri}) \quad 2.56$$

Since the atomic orbital basis set, $\{\varphi_r\}$, is multi centred, the orthogonality constraint on each φ_r is now

$$\langle \varphi_s | \varphi_r \rangle = S_{rs} \quad 2.57$$

where $\{S_{rs}\}$ are the elements of the overlap matrix, \mathbf{S} .

As before, the method of Lagrangian multipliers combines equation 2.56 and 2.57 to give,

$$\sum_{s,r} \left(F_{sr} C_{sa} - S_{sr} \sum_i C_{ri} \epsilon_{ia} \right) = 0 \quad 2.58$$

or in matrix form as,

$$\mathbf{F}\mathbf{C} = \epsilon\mathbf{S}\mathbf{C} \quad 2.59$$

The coefficients of the one particle basis functions are determined from solution of these equations. This is achieved, as before, by an iterative process which is carried out until self consistency is reached. The process starts with an initial guess for the density matrix, \mathbf{P} , which gives \mathbf{G} and then \mathbf{F} . The Hartree-Fock equations are diagonalised to give the total energy and a new density matrix. This whole process is then repeated until self consistency is reached.

For open shell systems, the corresponding Hartree-Fock equations and their method of solution are basically the same, but without the constraint that the space functions for two electrons of a doubly occupied orbital are the same.

Now, Φ_0 takes the more general form,

$$\Phi = \frac{1}{\sqrt{N!}} \left| \psi_1^\alpha(1)\alpha(1), \dots, \psi_{n_\alpha}^\alpha(n_\alpha)\alpha(n_\alpha), \psi_1^\beta(n_\alpha + 1)\beta(n_\alpha + 1), \dots, \psi_{n_\beta}^\beta(N)\beta(N) \right| \quad 2.60$$

and the total energy is given by the expression,

$$E = \sum_k \left\langle \psi_k^\alpha \left| \hat{h} + \frac{1}{2} (\hat{J} - \hat{K}^\alpha) \right| \psi_k^\alpha \right\rangle + \sum_m \left\langle \psi_m^\beta \left| \hat{h} + \frac{1}{2} (\hat{J} - \hat{K}^\beta) \right| \psi_m^\beta \right\rangle \quad 2.61$$

In the LCAO approximation,

$$\psi_k^\alpha = \sum_q \varphi_q C_{qk}^\alpha \quad 2.62$$

$$\psi_k^\beta = \sum_q \varphi_q C_{qk}^\beta \quad 2.63$$

or in matrix form,

$$\psi^\alpha = \varphi C^\alpha \quad 2.64$$

$$\psi^\beta = \varphi C^\beta \quad 2.65$$

The α - and β -spin density matrices are defined as before,

$$P_{rs}^\alpha = \sum_k^{n_\alpha} (C_{sk}^\alpha)^* C_{rk}^\alpha \quad \text{or in matrix form, } \mathbf{P}^\alpha = \mathbf{C}^\alpha \mathbf{C}^{\alpha\dagger} \quad 2.66$$

$$P_{rs}^{\beta} = \sum_m^{n_{\beta}} (C_{sm}^{\beta})^* C_{rm}^{\beta} \quad \text{or in matrix form, } \mathbf{P}^{\beta} = \mathbf{C}^{\beta} \mathbf{C}^{\beta\dagger} \quad 2.67$$

From these the total density matrix, \mathbf{P}^{tot} and net spin density matrix, \mathbf{P}^{spin} , are given by

$$\mathbf{P}^{\text{tot}} = \mathbf{P}^{\alpha} + \mathbf{P}^{\beta} \quad 2.68$$

$$\mathbf{P}^{\text{spin}} = \mathbf{P}^{\alpha} - \mathbf{P}^{\beta} \quad 2.69$$

The total energy can now be written as,

$$E = \text{Tr} \mathbf{P}^{\alpha} \mathbf{h} + \frac{1}{2} \text{Tr} \mathbf{P}^{\alpha} \mathbf{J}[\mathbf{P}^{\text{tot}}] - \frac{1}{2} \mathbf{P}^{\alpha} \mathbf{K}[\mathbf{P}^{\alpha}] + \text{Tr} \mathbf{P}^{\beta} \mathbf{h} + \frac{1}{2} \text{Tr} \mathbf{P}^{\beta} \mathbf{J}[\mathbf{P}^{\text{tot}}] - \frac{1}{2} \mathbf{P}^{\beta} \mathbf{K}[\mathbf{P}^{\beta}] \quad 2.70$$

$$= \text{Tr} \mathbf{P}^{\text{tot}} \mathbf{h} + \frac{1}{2} \text{Tr} \mathbf{P}^{\text{tot}} \mathbf{J}[\mathbf{P}^{\text{tot}}] - \frac{1}{2} \text{Tr} \mathbf{P}^{\alpha} \mathbf{K}[\mathbf{P}^{\alpha}] - \frac{1}{2} \text{Tr} \mathbf{P}^{\beta} \mathbf{K}[\mathbf{P}^{\beta}] \quad 2.71$$

After a first order variation and introduction of the orthonormality constraint by the method of Lagrangian multipliers, the final equations for the α and β states are,

$$\mathbf{F}^{\alpha} \mathbf{C}_i^{\alpha} = \varepsilon_i^{\alpha} \mathbf{S} \mathbf{C}_i^{\alpha} \quad 2.72$$

$$\mathbf{F}^{\beta} \mathbf{C}_i^{\beta} = \varepsilon_i^{\beta} \mathbf{S} \mathbf{C}_i^{\beta} \quad 2.73$$

where

$$\mathbf{F}^{\alpha} = \mathbf{F} - \mathbf{Z} \quad 2.74$$

$$\mathbf{F}^{\beta} = \mathbf{F} + \mathbf{Z} \quad 2.75$$

and in the notation used previously,

$$\mathbf{F} = \mathbf{h} + \mathbf{G} \quad 2.76$$

$$\mathbf{Z} = \frac{1}{2} \mathbf{K}[\mathbf{P}^{\text{spin}}] \quad 2.77$$

$$\mathbf{G} = \mathbf{J}[\mathbf{P}^{\text{tot}}] - \frac{1}{2} \mathbf{K}[\mathbf{P}^{\text{tot}}] \quad 2.78$$

The equations derived thus far are for non periodic systems, but it can be extended to periodic systems of any dimension by exploiting the associated translational symmetry. The unit cell of the direct lattice is spanned by the set of basis translation vectors, $\mathbf{a}_1, \mathbf{a}_2, \mathbf{a}_3$, from which the general lattice point, \mathbf{R}_0 , corresponding to the unit cell position, \mathbf{r}_0 , is given by

$$\mathbf{R}_0 = \mathbf{r}_0 + N_1\mathbf{a}_1 + N_2\mathbf{a}_2 + N_3\mathbf{a}_3, \quad 2.79$$

where N_1, N_2 and N_3 are integers in the range $-\infty \rightarrow +\infty$ including zero. The space group is a set of symmetry operations which describes the symmetry of the crystal system. This set consists of point symmetry operations, p , translational vectors, \mathbf{t} , or fractional translational vectors, \mathbf{v} . The complete set of translations, \mathbf{t} , form an Abelian group which means that the operations of the group commute, and the irreducible representations of the group are indexed by a wave vector, \mathbf{k} , such that the operation, \mathbf{t}_n can be expressed as $\exp(i\mathbf{k}\cdot\mathbf{t}_n)$. Periodic boundary conditions apply and the \mathbf{k} vectors form a lattice which is known as the reciprocal lattice in \mathbf{k} space. In this reciprocal lattice, the equivalent of the unit cell of the direct lattice is known as the Brillouin Zone (BZ). Any general reciprocal lattice vector, \mathbf{K} , is given by,

$$\mathbf{K} = n_1\mathbf{b}_1 + n_2\mathbf{b}_2 + n_3\mathbf{b}_3, \quad 2.80$$

where the basis set, $\{\mathbf{b}_i\}$, in reciprocal space is defined by

$$\mathbf{a}_i \cdot \mathbf{b}_j = 2\pi\delta_{ij} \quad 2.81$$

and must satisfy the condition,

$$\exp(i\mathbf{K}\cdot\mathbf{t}_n) = 1 \text{ for all } \mathbf{t}_n \quad 2.82$$

For periodic systems the spin orbitals of equation 2.21, which are appropriately called crystalline orbitals, are expressed as linear combination of Bloch functions, $\{\chi_j(\mathbf{r}, \mathbf{k})\}$, where the Bloch functions are written as a linear combination of local atomic functions, $\{\phi_j\}$, centred at the nuclear positions,

$$\chi_j(\mathbf{r}, \mathbf{k}) = \sum_{\mathbf{G}} \varphi_j(\mathbf{r} - \mathbf{G} - \mathbf{r}_j) \exp(-i\mathbf{k} \cdot \mathbf{G}) \quad 2.84$$

The local atomic functions, $\{\varphi_j\}$, are mostly given as products of Gaussian functions and solid harmonics of the type

$$\varphi_j(\mathbf{r} - \mathbf{G} - \mathbf{r}_j) = \sum_{k=1}^m d_{kj} g_k(\mathbf{r} - \mathbf{G} - \mathbf{r}_j) \quad 2.85$$

and

$$g_k(\mathbf{r}) = N_{lm}(\alpha_k) Y_{lm}(\theta, \phi) r^l \exp(-\alpha_k r^2) \quad 2.86$$

$$\phi_a^\sigma(\mathbf{r}, \mathbf{k}) = \sum_{j=1}^m c_{ja}^\sigma(\mathbf{k}) \chi_j(\mathbf{r}, \mathbf{k}) \quad 2.87$$

The coefficients, $\{c_{ja}^\sigma\}$, are obtained by solution of the Hartree-Fock equations, given in matrix notation by,

$$\mathbf{F}^\sigma(\mathbf{k}) \mathbf{C}^\sigma(\mathbf{k}) = \mathbf{S}(\mathbf{k}) \mathbf{C}^\sigma(\mathbf{k}) \boldsymbol{\varepsilon}(\mathbf{k}) \quad 2.88$$

for any \mathbf{k} -point in the BZ, where, in equation 2.88, $\mathbf{F}^\sigma(\mathbf{k})$ is the Fock matrix in reciprocal space, $\mathbf{S}(\mathbf{k})$, the overlap matrix which spans the Bloch functions and $\boldsymbol{\varepsilon}(\mathbf{k})$ the diagonal energy matrix.

The Fock operator in reciprocal space can be converted to the corresponding operator in direct space by a straight forward Fourier transform, thus,

$$F_{12}^\sigma(\mathbf{k}) = \sum_{\mathbf{T}} F_{12}^{\mathbf{T}} \exp(i\mathbf{k} \cdot \mathbf{T}) \quad 2.89$$

Therefore, in the case of open shell periodic systems, the contributions to the Fock matrix in direct space become,

$$F_{12}^\alpha(\mathbf{t}) = F_{12}(\mathbf{t}) + Z_{12}(\mathbf{t}) \quad 2.90$$

$$F_{12}^\beta(\mathbf{t}) = F_{12}(\mathbf{t}) - Z_{12}(\mathbf{t}) \quad 2.91$$

The matrix elements of \mathbf{F} and \mathbf{Z} then are expressed as

$$F_{12}(\mathbf{t}) = h_{12}(\mathbf{t}) + G_{12}(\mathbf{t}) \quad 2.92$$

$$Z_{12}(\mathbf{t}) = \frac{1}{2} K_{12}(\mathbf{t}) [P^{\text{spin}}] \quad 2.93$$

$$G_{12}(\mathbf{t}) = J_{12}(\mathbf{t}) [P^{\text{tot}}] - \frac{1}{2} K_{12}(\mathbf{t}) [P^{\text{tot}}] \quad 2.94$$

The matrix elements of $\mathbf{J}[\mathbf{P}]$ and $\mathbf{K}[\mathbf{P}]$ are

$$J_{12}(\mathbf{t})[\mathbf{P}] = \sum_{3,4;n} P_{34}(\mathbf{n}) \left[\sum_h \left(\chi_1^0 \chi_4^{h+n} \middle| \chi_2^g \chi_3^h \right) \right] \quad 2.95$$

$$K_{12}(\mathbf{t})[\mathbf{P}] = \sum_{3,4;n} P_{34}(\mathbf{n}) \left[\sum_h \left(\chi_1^0 \chi_4^{h+n} \middle| \chi_3^g \chi_2^h \right) \right] \quad 2.96$$

The bielectronic integrals are represented as follows,

$$\left(\chi_1^0 \chi_4^{h+n} \middle| \chi_3^g \chi_2^h \right) = \iint d\mathbf{r}_1 d\mathbf{r}_2 \chi_1^0(\mathbf{r}_1)^* \chi_4^{h+n}(\mathbf{r}_2)^* \frac{1}{r_{12}} \chi_2^g(\mathbf{r}_1) \chi_3^h(\mathbf{r}_2) \quad 2.97$$

The expression for the total energy is then,

$$\begin{aligned} E = & \sum_{1,2;t} P_{12}^{\text{tot}}(\mathbf{t}) h_{12}(\mathbf{t}) + \frac{1}{2} \sum_{1,2;t} P_{12}^{\text{tot}}(\mathbf{t}) J_{12}(\mathbf{t}) [P^{\text{tot}}] \\ & - \frac{1}{2} \sum_{1,2;t} P_{12}^{\alpha}(\mathbf{t}) K_{12}(\mathbf{t}) [P^{\alpha}] - \frac{1}{2} \sum_{1,2;t} P_{12}^{\beta}(\mathbf{t}) J_{12}(\mathbf{t}) [P^{\beta}] \end{aligned} \quad 2.98$$

or using the Fock matrix the expression for the total energy becomes,

$$E = \frac{1}{2} \sum_{1,2;t} P_{12}^{\text{tot}}(\mathbf{t}) h_{12}(\mathbf{t}) + \frac{1}{2} \sum_{1,2;t} P_{12}^{\alpha}(\mathbf{t}) F_{12}^{\alpha}(\mathbf{t}) + \frac{1}{2} \sum_{1,2;t} P_{12}^{\beta}(\mathbf{t}) F_{12}^{\beta}(\mathbf{t}) \quad 2.99$$

The matrices \mathbf{G} and \mathbf{Z} are substituted into the total energy expression to give,

$$E = \frac{1}{2} \sum_{1,2;t} P_{12}^{\text{tot}}(\mathbf{t}) h_{12}(\mathbf{t}) + \frac{1}{2} \sum_{1,2;t} P_{12}^{\alpha}(\mathbf{t}) G_{12}(\mathbf{t}) - \frac{1}{2} \sum_{1,2;t} P_{12}^{\text{spin}}(\mathbf{t}) Z_{12}(\mathbf{t}) \quad 2.100$$

The density matrix of a periodic system can now be written as,

$$\mathbf{P}_{ij}^{\sigma}(\mathbf{t}) = \sum_a \frac{1}{V_B} \int_{BZ} d\mathbf{k} c_{ai}^{\sigma}(\mathbf{k})^* c_{aj}^{\sigma}(\mathbf{k}) \exp(i\mathbf{k} \cdot \mathbf{t}) \vartheta[E_f - \epsilon_a^{\sigma}(\mathbf{k})] \quad 2.101$$

where $c_{aj}^{\sigma}(\mathbf{k})$ is the coefficient of the j^{th} Bloch function of the a^{th} crystalline orbital at the point \mathbf{k} with corresponding eigenvalue, $\epsilon_a^{\sigma}(\mathbf{k})$, ϑ is the step function which takes the value of 1 if $\epsilon_a^{\sigma}(\mathbf{k}) < E_f$, the Fermi energy, otherwise zero. The Fermi energy is the energy below which all the electron states are filled. It can be determined by imposing the condition that $N/2$ crystalline orbitals exist such that their eigenvalues are less than the Fermi energy, $\epsilon_a^{\sigma}(\mathbf{k}) < E_f$. Then the Fermi energy can be described by the following expression, where q is the number of electrons present in the unit cell.

$$q = \frac{2}{N} \sum_a \sum_{\mathbf{k}} \vartheta[E_f - \epsilon_a^{\sigma}(\mathbf{k})] = \frac{2}{V_B} \sum_a \int_{BZ} d\mathbf{k} \vartheta[E_f - \epsilon_a^{\sigma}(\mathbf{k})] \quad 2.102$$

Reciprocal space integration must be carried out at each cycle of the self consistent process in order to evaluate the Fermi energy and reconstruct the one electron density matrix. This is done by the determination of the eigenvalues, $c_{ai}^{\sigma}(\mathbf{k})$, and eigenvectors, $\epsilon_a^{\sigma}(\mathbf{k})$, at a certain number of sample points which belong to a lattice known as the Monkhorst net⁴. The Monkhorst net has basis vectors, $\mathbf{b}_1/s_1, \mathbf{b}_2/s_2, \mathbf{b}_3/s_3$, where $\mathbf{b}_1, \mathbf{b}_2, \mathbf{b}_3$ are the reciprocal lattice vectors and s_1, s_2 and s_3 are integers known as shrinking factors. The number of nonequivalent sample points is given by the product of shrinking factors divided by the order of the point group. A weighting factor, w_i is derived from each point from the known eigenvalues, $\epsilon_a^{\sigma}(\mathbf{k})$. In the case of insulating systems, where all bands are either fully occupied or vacant, E_f is easily determined and the expression for the density matrix becomes a weighted sum over n limited to occupied bands, of the integrand function. For conducting systems with partially filled bands this method is more complex and not described here.

The CRYSTAL code was originally developed in the University of Torino by Pisani, Dovesi and Roetti during the late 1970's and later in collaboration with Saunders at the Daresbury laboratories. It allows the calculation of the

wavefunction and properties of crystalline systems within the Hartree-Fock LCAO approximation based on the mathematical structure outlined earlier in this chapter.

The necessary CRYSTAL input consists of the symmetry properties of the system, the contraction coefficients and exponents of the Gaussian primitives and a set of computational parameters which control the accuracy of the calculation. The required symmetry information includes the space group number, the number and coordinate positions of the inequivalent atoms in the unit cell and the values of all lattice constants.

Since the cpu time is directly proportional to the number of basis functions used, an efficient calculation requires a basis set which gives a good description of the atomic orbitals using the least possible number of Gaussians.

The basis sets which were used to obtain the results presented in this thesis are described below, where the number in brackets indicates the number of Gaussian type functions used to describe each shell.

Li 1s(6) 2sp(1)

O 1s(8) 2sp(4) 3sp(1) 4sp(1)

O 1s(8) 2sp(4) 3sp(1) 4sp(1) 3d(1)

Ti:1s(8)2sp(6)3sp(4)4sp(1)5sp(1)3d(3)

Ti:1s(8)2sp(6)3sp(4)4sp(1)5sp(1)3d(4)4d(1)

Mn 1s(8) 2sp(6) 3sp(4) 4sp(1) 5sp(1) 3d(4) 4d(1)

Fe 1s(8) 2sp(6) 3sp(4) 4sp(1) 5sp(1) 3d(4) 4d(1)

Details of the exponents and contraction coefficients of the basis functions used to represent Mn, O, Fe and Li have been published previously in studies of MnO^6 , $\alpha\text{-Fe}_2\text{O}_3$ ⁷ and Li:NiO^8 , however, a full detailed listing of all exponents and contraction coefficients used in this thesis is given in the appendix. Where there are two different basis sets for the same atom, the smaller one was used most widely. For example, the larger oxygen basis set was only used in chapter 7 for the investigation of MnFe_2O_4 spinel and the larger Ti basis was only used in chapter 8 in the surface study of TiO_2 .

A set of computational parameters complete the input information required to run the CRYSTAL program. These are used to specify the degree of accuracy

required in the truncation of infinite series, the SCF cycle and integration procedures carried out in reciprocal space.

The program itself is divided into three main parts. In part one all mono and bielectronic integrals are calculated, then in part two the Hartree-Fock equations are solved during the SCF process and part three offers the opportunity to calculate various properties of the crystalline system such as densities of states and charge and spin distributions.

During part one of the program all the required monoelectronic and bielectronic integrals are evaluated. This can be a very time consuming process as a huge number of integrals must be considered, therefore a screening process is adopted for the bielectronic integrals. The expression for a bielectronic integral over primitive Gaussian functions can be represented as, $I = \langle ab|cd \rangle = S_{ab}S_{cd}T_{abcd}$, where S_{ab} is the radial overlap between the functions, χ_a and χ_b and T_{abcd} is the angular function which varies very slowly. In many cases the product of the overlap, $S_{ab}S_{cd}$, gives a good estimate of the magnitude of the integral. This process can be used to identify the integrals which fall below a threshold value and can, therefore, be ignored. The radial overlaps of all bielectronic integrals are calculated in fast algorithms using s-type Gaussian functions, known as adjoined Gaussians. The integrals which remain after the screening process are dealt with in a number of ways which depends on the distance between the interacting charge distributions. A finite zone can be defined where the two interacting distributions overlap, this is known as the B zone. Within this zone all Coulomb integrals are evaluated exactly. Outside this zone, the Coulomb terms are approximated by the Ewald method⁵. For the exchange series the overlapping distribution decays exponentially with the increase in distance between the interacting distributions and so the exchange series is naturally truncated after a few terms.

Part 2 of the program involves the use of the integrals evaluated in part 1 in solution of the Hartree-Fock equations by the iterative SCF process. The process can be summarised as follows for the UHF case. The Fock matrices, F_t^α and F_t^β are constructed from the monoelectronic and bielectronic integrals in direct

space. The Fock matrices are then converted to reciprocal space by the Fourier transform process. After conversion into \mathbf{k} space, the matrices, $\mathbf{F}(\mathbf{k})$ are then diagonalised, yielding the eigenvalues and corresponding eigenvectors. Finally the eigenvalues are used to evaluate the Fermi energy and the eigenvectors go into the reconstruction of the density matrices. The whole process is then repeated until self consistency is achieved. From the SCF process the eigenvectors, Bloch coefficients, are calculated which span the crystalline orbitals. From the crystalline orbitals the many body wavefunction can be evaluated.

Part 3 of CRYSTAL is used to calculate various properties of the crystalline system from the wavefunction calculated in part 2. These properties include the density of states (DOS) and the charge and spin density distributions. A correction to the total Hartree-Fock energy due to the effects of correlation between electrons can also be calculated in part 3 using a selection of functionals.

References

1. R.Dovesi, V.R.Saunders and C.Roetti, M.Causà, N.M.Harrison, R.Orlando and E.Aprà, *CRYSTAL 95, User Manual* (Università di Torino and CCLRC Daresbury Laboratory, 1995)
2. D.R.Hartree, *Proc. Camb. Phil. Soc.*, 1928, **24**, 89
3. C.C.J.Roothaan, *Rev. Mod. Phys.*, 1951, **23**, 69
4. J.H.Monkhorst, *Phys. Rev. B*, 1979, **20**, 1504
5. P.P.Ewald, *Ann. Phys. (Leipzig)*, 1921, **64**, 253
6. M.D.Towler, N.L.Allan, N.M.Harrison, V.R.Saunders, W.C.Mackrodt, E.Aprà and R.Dovesi, *Philosophical Magazine A*, 1993, **68**, 653
7. M.Catti, G.Valerio and R.Dovesi, *Physical Review B*, 1995, **51**(12), 7441
8. W.C.Mackrodt, N.M.Harrison, V.R.Saunders, N.L.Allan, M.D.Towler, *Chemical Physics Letters*, 1996, **250**, 66

Chapter 3

The Electronic Structure And Magnetism Of The Hole And Electron States In MnO

3.1. Introduction

Transition metal oxides are a most interesting class of solids as they form a variety of systems with properties which are often attributed to the variable valence of the transition metals¹. The manganese oxides are no exception and are often described formally in terms of Mn(I), Mn(II), Mn(III), ..., etc, or more usually, Mn^+ , Mn^{2+} , Mn^{3+} , ..., etc. MnO appears in the intermediate region of the Zaanen, Sawatzky and Allen² (ZSA) phase diagram of transition metal oxides, in which these authors proposed that the early members of the first row transition metal oxides are Mott-Hubbard (d-d) insulators, and the later members are charge transfer (p-d) insulators. An x-ray photoelectron and bremsstrahlung isochromat spectroscopic (BIS) study by van Elp *et al*³ of MnO confirmed its position, as did self-energy corrected (SIC) local spin density (LSD) calculations by Svane and Gunnarsson⁴, which were contrary to earlier band structure calculations⁵ which suggested a d-d gap.

Previous UHF calculations on antiferromagnetic (AF) and ferromagnetic (FM) MnO and NiO^{6,7} showed that the upper valence bands of both are dominated by oxygen 2p states suggesting that they are high spin charge transfer (p-d) insulators. More recently, *ab initio* UHF calculations have provided direct computational evidence from the charge and spin densities and unoccupied densities of states that the bound hole in Li doped NiO (Li:NiO)⁸ and the self trapped hole in NiO⁹ are oxygen 2p in nature. These findings are in agreement with an oxygen-k edge x-ray absorption spectroscopy study by Kuiper *et al*¹⁰ and a Ni 2p XPS by van Elp *et al*¹¹. Subsequent cluster calculations by van Elp *et al*¹² have also confirmed this. However, Springhorn and Schmalzried¹³ cast doubts as to the generality of the nature of these hole states from conductivity measurements of $Fe_xNi_{1-x}O$ and suggested that the observed conductivity was due to the hopping of Fe(d) holes rather than O(p) holes.

Subsequent UHF calculations on $\text{Fe}_{0.125}\text{Ni}_{0.875}\text{O}$ showed that indeed the main contribution to the valence band upper edge was Fe(d), and that the holes created were Fe 3d holes in complete agreement with the findings of Springhorn and Schmalzried¹³. From considerations of the type suggested by Towler *et al*¹⁴ related to UHF calculations on $\text{M}_x\text{N}_{1-x}\text{O}$ and of the parent oxides, NO and MO, it was predicted that FeO would be a Mott-Hubbard insulator, rather than a charge transfer insulator as suggested by the ZSA² phase diagram. Therefore this raises the question as to the nature of the hole states in MnO as it lies in the intermediate region of the ZSA phase diagram with FeO on the charge transfer side. In view of this important question an extensive range of calculations have been performed addressing this issue. This chapter presents the results of UHF calculations which were carried out on FM and AF MnO in both the neutral and first ionised states, on AF Li doped MnO (Li:MnO) and also on the first electron addition state of FM MnO.

The results presented later in this chapter have important implications for the electronic structure of the higher manganese oxides in general. For this reason the valence charge states of MnO_2 , Li_xMnO_2 and MnFe_2O_4 were also investigated and the results are presented in chapters 4, 5 and 6 respectively.

3.2. Results

3.2.1. Neutral MnO

For completeness, this section begins with a review of UHF calculations of neutral MnO ^{6,7}, the face centred cubic (fcc) lattice structure of which is shown in figure 3.1. The previously calculated lattice parameter, $a = 4.5239\text{\AA}$ ⁷ was used in the calculation of the ferromagnetic and two different antiferromagnetic spin states of MnO, referred to here after as FM, AF_{II} and AF_1 respectively. In the FM spin arrangement, all spins on the Mn are parallel, while in the AF_{II} arrangement, Mn_1 , Mn_5 , Mn_6 and Mn_7 (of figure 3.1) have opposite spins to Mn_2 , Mn_3 , Mn_4 and Mn_8 .

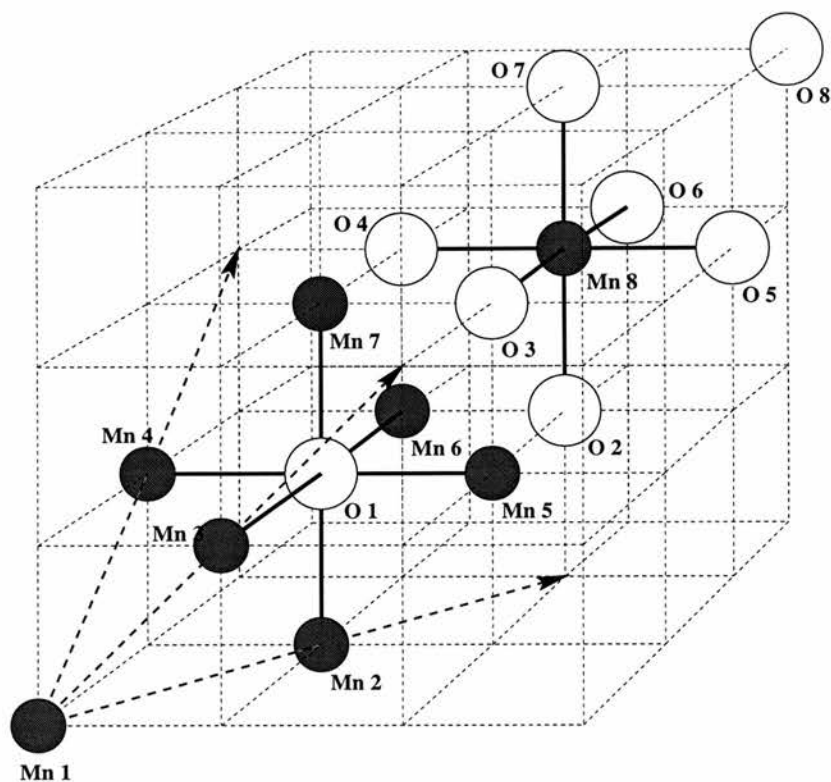


Figure 3.1. Lattice structure of MnO

The AF_{II} arrangement is found to be lowest in energy with the order of stability, $AF_{II} < FM < AF_{I}$ and the energy difference between the AF_{II} and FM spin arrangements $\approx 0.006\text{eV}$ per MnO which illustrates the high numerical accuracy of the CRYSTAL code. This energy difference seems to accord with the Néel temperature of $\sim 120\text{K}$ within a mean-field Ising model as pointed out by Towler *et al*⁷ previously. All three magnetic ground states are largely ionic with high spin d^5 electron configurations. For the AF_{II} arrangement, the total Mulliken charges are $\sim \pm 1.86e$, with a 3d population of 5.11, and Mn spin population of 4.92. A full analysis is shown in table 3.1 for both the AF_{II} and the FM spin states from which it is clear that the charge and spin populations are identical in the two states. The calculated valence band DOS of the AF_{II} and FM arrangements are shown in figure 3.2, where, as noted previously the upper valence band edge is dominated by oxygen 2p states, which suggests that within a rigid band approximation, electron holes are predominantly O(2p).

	FM	AF _{II}
q_M	± 1.86	± 1.86
n_{3d}	5.11	5.11
n_{MnO}	-0.02	-0.02
$n_s(Mn)$	4.92	± 4.92
$n_s(O)$	0.08	0.0

Table 3.1. Total Mn Mulliken charge, q_M ($|e|$), 3d population, n_{3d} (e), MnO overlap population, n_{MnO} , and local spin moments, n_s (μ_B), in the FM and AF_{II} states of MnO

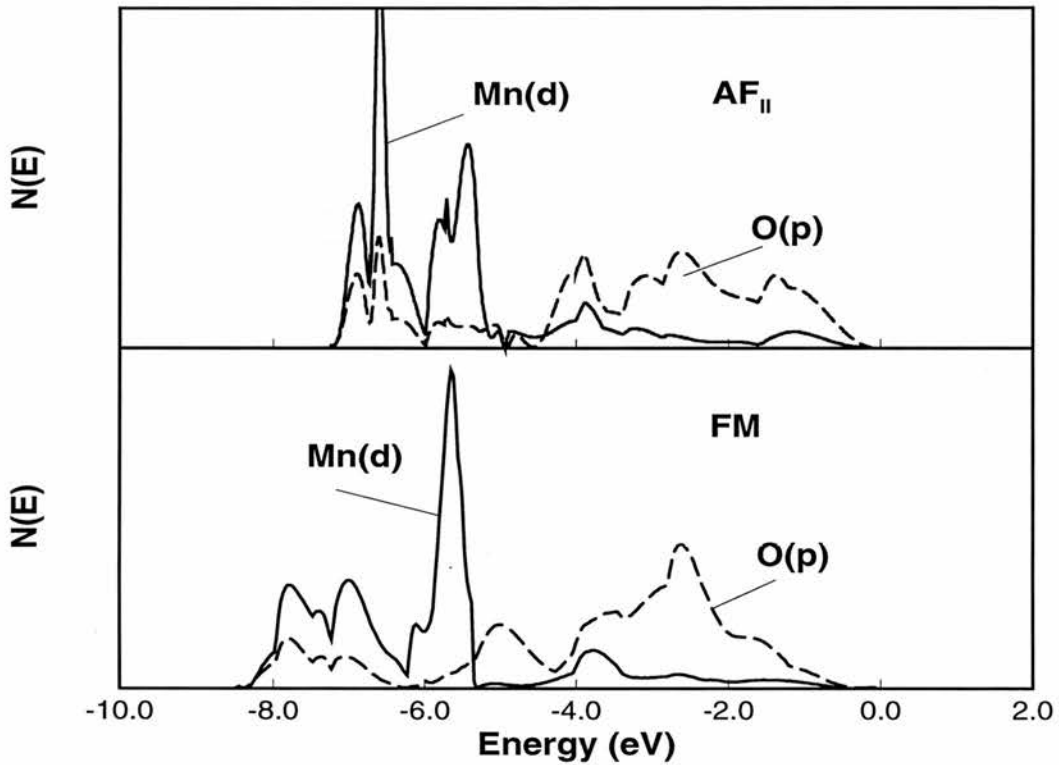


Figure 3.2. Valence band DOS of AF_{II} and FM MnO

3.2.2 Hole States in MnO

For calculations of hole states, supercells of composition $Mn_8O_8^+$ were used, the basic structure of which is shown in figure 3.1. Since the Coulombic interaction of periodic charged cells would result in infinite energy, a uniform background

charge of opposite sign and equal magnitude to the crystal potential must be added. Starting with the FM spin arrangement, one electron was removed to create a hole. This was found to distribute equally over the six symmetry equivalent oxygen atoms of the Mn_8O_8^+ lattice to minimise the kinetic energy of the hole. However, with reference to figure 3.1, on breaking the symmetry of the lattice by displacing Mn7 or one of the other five symmetry equivalent Mn atoms in the (001) (or equivalent) direction by an infinitesimal (0.001\AA) distortion, the hole localises at the O1 site leading to a local electron configuration which is close to O^- and a UHF solution which is lower in energy than that for the symmetric delocalised state. This energy difference, between the fully symmetric and the distorted states, is the self trapping energy referred to here after as the trapping energy.

For the FM Mn_8O_8^+ lattice, there are two possible spin arrangements which can be adopted. These are shown in figure 3.3(a) and figure 3.3(b). In the first of these (figure 3.3(a)), the unpaired spin of the central O^- atom is antiparallel to the spin on the lattice: this is referred to as the low spin ferromagnetic state (ls-FM). In the other spin arrangement (figure 3.3(b)), the unpaired spin of the central oxygen atom is parallel to the spin on the lattice and is referred to as the high spin ferromagnetic state (hs-FM).

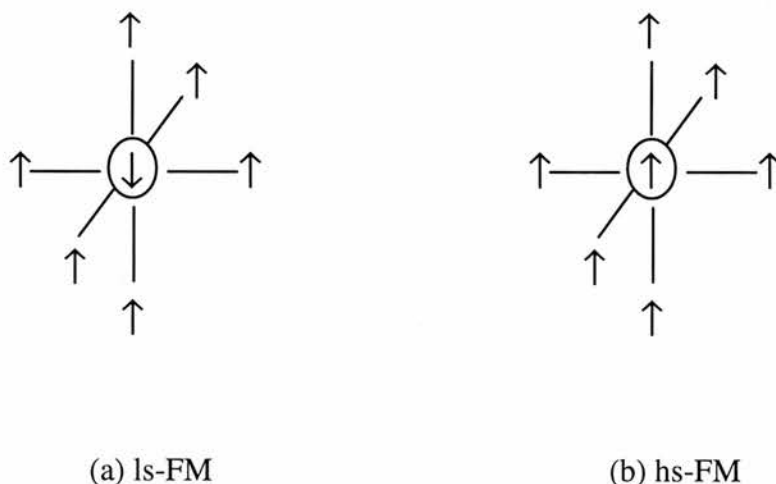


Figure 3.3. The ferromagnetic (a) low spin and (b) high spin, spin arrangements about the central unpaired electron of the oxygen hole state

For an infinitesimal displacement of Mn7 in the ls-FM and hs-FM arrangements, self trapping energies of 2.33eV and 2.45eV are obtained respectively, where ~80% of the hole is localised at the O1 site. The local moments at the O⁻ site are $-0.83\mu_B$ and $1.02\mu_B$ for the ls-FM and hs-FM $Mn_8O_8^+$ spin states respectively. The detailed changes in the Mulliken charges between the neutral and first ionised states for these 2 spin arrangements can be found in the second and third columns of table 3.2.

δq_M	ls-FM	hs-FM	AF _{II}	AF _{II} *	FM
Mn ₁	+ 0.02	0.0	+ 0.02	+ 0.02	- 0.03
Mn ₂	+ 0.01	0.0	+ 0.01	+ 0.50	- 0.02
Mn ₃	+ 0.01	0.0	+ 0.02	+ 0.02	- 0.02
Mn ₄	+ 0.02	+ 0.02	+ 0.01	+ 0.02	- 0.05
Mn ₅	+ 0.02	+ 0.02	+ 0.02	+ 0.02	- 0.76
Mn ₆	+ 0.01	0.0	+ 0.01	+ 0.02	- 0.02
Mn ₇	+ 0.01	0.0	+ 0.01	+ 0.02	- 0.02
Mn ₈	+ 0.02	0.0	+ 0.02	+ 0.04	- 0.03
O ₁	+ 0.76	+ 0.84	+ 0.81	+ 0.02	0.0
O ₂	+ 0.02	+ 0.02	+ 0.02	+ 0.01	- 0.01
O ₃	+ 0.02	+ 0.02	+ 0.01	+ 0.07	- 0.01
O ₄	+ 0.02	+ 0.02	+ 0.01	+ 0.07	0.0
O ₅	+ 0.02	+ 0.02	+ 0.01	+ 0.07	0.0
O ₆	+ 0.02	+ 0.02	+ 0.01	+ 0.07	- 0.01
O ₇	+ 0.02	+ 0.02	+ 0.02	+ 0.01	- 0.01
O ₈	+ 0.03	+ 0.03	+ 0.02	+ 0.02	0.0

Table 3.2. Changes in the total Mulliken charges, δq_M ($|e|$), for ls-FM, hs-FM and AF_{II} $Mn_8O_8^{(+)}$, where * denotes the excited configuration, and FM $Mn_8O_8^{(-)}$.

For the symmetry broken system a simple one dimensional relaxation of the structure was examined by direct energy minimisation with respect to further

displacing Mn7 for the 2 FM spin states. This results in minimum energy solutions at displacements of 0.16\AA for the ls-FM state and 0.20\AA for the hs-FM state with associated relaxation energies of 0.17eV and 0.33eV respectively. More extensive relaxations were ruled out on the grounds of the extensive computing time required.

Removing an electron from the AF_{II} lattice results in a hole, delocalised over the symmetry equivalent O atoms of the Mn_8O_8^+ lattice, as for the FM spin arrangement. In the case of the symmetry broken AF_{II} lattice, although there is only one spin arrangement which can be adopted, with the unpaired electron of the O^- atom parallel to the spin up sites and antiparallel to the spin down sites, there are two ways of breaking the symmetry which result in different solutions. Figures 3.3(c) and 3.3(d) show these two situations. The first of these is shown in figure 3.3(c) where Mn2, here surrounded by a square, with its spin parallel to that of the unpaired spin of the central oxygen atom, is displaced in the $(00\bar{1})$ direction, indicated by the bold arrow.

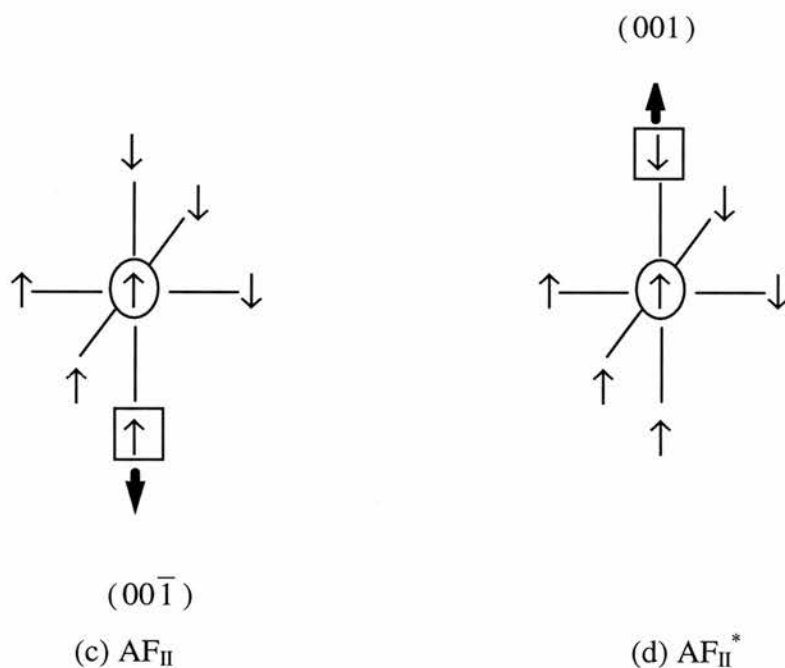


Figure 3.3. The antiferromagnetic (c) AF_{II} and (d) AF_{II}^* spin arrangements and displacements about the central unpaired electron of the oxygen hole state

This results in 79% of the hole localising in a p_σ orbital of O1 (see table 3.2), in a state which is 0.29eV higher in energy than the ls-FM state. The trapping energy is 2.51eV and the relaxation energy is 0.15eV for a 0.14Å relaxation of Mn2. The second type of displacement is shown in figure 3.3(d) where Mn7 (surrounded by a square) with a spin antiparallel to the unpaired spin of the central O⁻ electron, is displaced in the $(00\bar{1})$ direction as shown. This results in a completely different electronic state, referred to here as AF_{II}^* , in which 50% of the hole localises at Mn2, ~30% on 4 neighbouring oxygen atoms, and the remainder delocalising throughout the lattice (see table 3.2 for details). This state is 1.00eV higher in energy than the ls-FM state and has a trapping energy of 1.81eV. Tables 3.3 and 3.4 give details of the Mulliken analyses and energies associated with the electron holes of the FM and AF spin arrangements. The Pauli repulsion energy, introduced in table 3.4, is defined as the energy difference between the distorted hole states of MnO relative to ls-FM.

Hole State	ΔE
ls-FM	0.0
ls-FM (relaxed)	-0.17
ls-FM (symmetric)	+2.33
hs-FM	+0.71
hs-FM (relaxed)	+0.38
hs-FM (symmetric)	+3.16
AF_{II}	+0.29
AF_{II} (relaxed)	+0.14
AF_{II} (symmetric)	+2.80
excited state AF_{II}	+1.00

Table 3.3. Energies, ΔE (eV), of hole state configurations in MnO relative to the infinitesimally distorted low spin FM state, ls-FM.

State	E_T	E_P	E_R
ls-FM	2.33	0.0	0.17
hs-FM	2.45	0.71	0.33
AF _{II}	2.51	0.29	0.14

Table 3.4 Trapping, E_T , Pauli repulsion, E_P (relative to ls-FM), and lattice relaxation, E_R , energies (all in eV) for the hole states in MnO

In addition to the evidence presented so far from the Mulliken populations, direct evidence of the observed self trapped oxygen hole in MnO is obtained from the net spin and charge densities, which are calculated directly from the wavefunction. Figure 3.4(a) shows the net spin density in a {001} basal plane of neutral FM Mn_8O_8 . As might have been anticipated, the majority of spin is localised at the four Mn sites, with only a small dispersion over the oxygen atoms.

Turning now to the same {001} plane through ls-FM $Mn_8O_8^+$, which is shown in figure 3.4(b), it is clear that the central oxygen atom has undergone a major change in spin density, with the other atoms remaining more or less unchanged from the neutral system. This is entirely consistent with the Mulliken population analysis of ls-FM $Mn_8O_8^+$, as discussed earlier, which predicts a localised oxygen hole with an unpaired electron which is antiferromagnetic to the rest of the lattice.

Figure 3.4(c) illustrates the spin density in a similar {001} basal plane of hs-FM $Mn_8O_8^+$ where, as seen, the central oxygen atom exhibits an increase in positive spin density, in the shape of a p_σ orbital, indicating unpaired spin density which is ferromagnetic with the rest of the lattice. This also is consistent with the Mulliken picture of a localised oxygen hole. Again in the hs-FM state there is very little change in spin density elsewhere in the lattice.

The net spin density through a {001} basal plane of AF_{II} $Mn_8O_8^+$ is shown in figure 3.4(d). Here the antiferromagnetic arrangement of the high spin Mn atoms is clearly visible, with a striking p_σ shaped density at the central oxygen and very little dispersion on the other oxygen atoms. This illustrates the unpaired spin on

the central oxygen atom created by the oxygen hole. All of these spin density plots are completely consistent with the Mulliken spin population analyses.

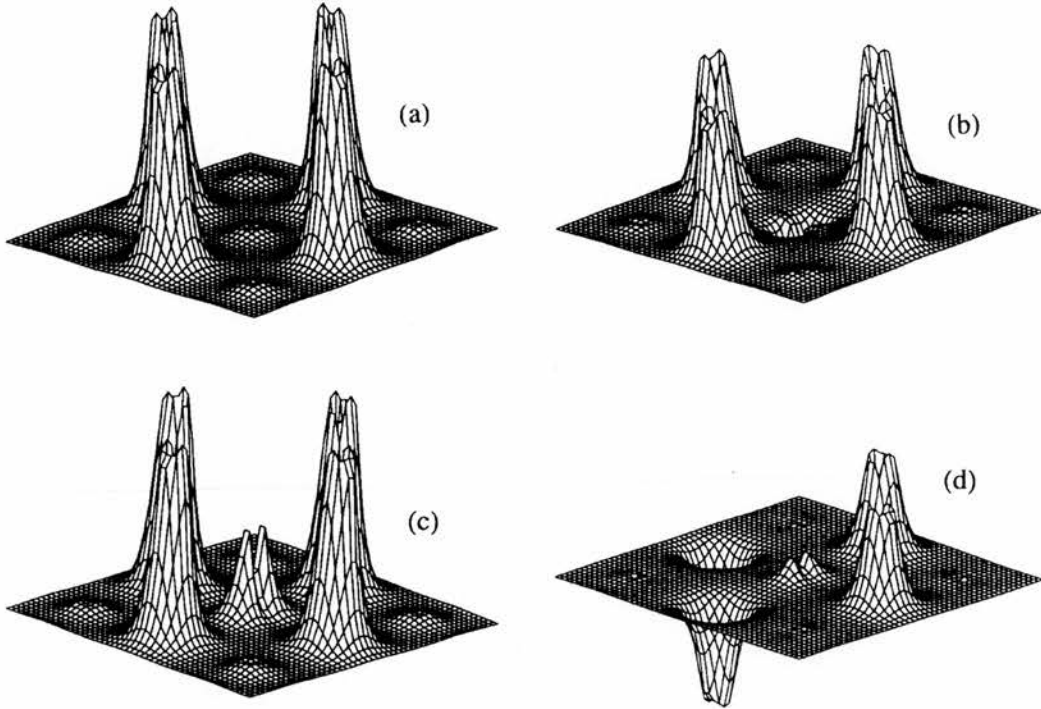


Figure 3.4. Net ($\uparrow - \downarrow$) spin density in the basal $\{001\}$ plane of (a) Mn_8O_8 , (b) (ls-FM) $\text{Mn}_8\text{O}_8^{(+)}$ (c) (hs-FM) $\text{Mn}_8\text{O}_8^{(+)}$ (d) (AF_{II}) $\text{Mn}_8\text{O}_8^{(+)}$

The single particle DOS provide further insight into the nature of the hole states of MnO. Figure 3.5 shows the projected empty oxygen p and manganese d states of FM Mn_8O_8 and ls-FM Mn_8O_8^+ . The middle panel illustrates the occurrence of new empty oxygen p states, $\sim 3\text{-}4$ eV below the conduction band edge, which are associated with ls-FM Mn_8O_8^+ . The upper panel shows that these states are localised almost exclusively at O1, the site of the self trapped hole from the Mulliken population analysis. The lower panel illustrates the very small manganese d contribution, which is almost negligible, to these new states in ls-FM Mn_8O_8^+ . Overall then this oxygen hole state in MnO corresponds exactly to the findings of similar UHF calculations of the self trapped hole in NiO^9 .

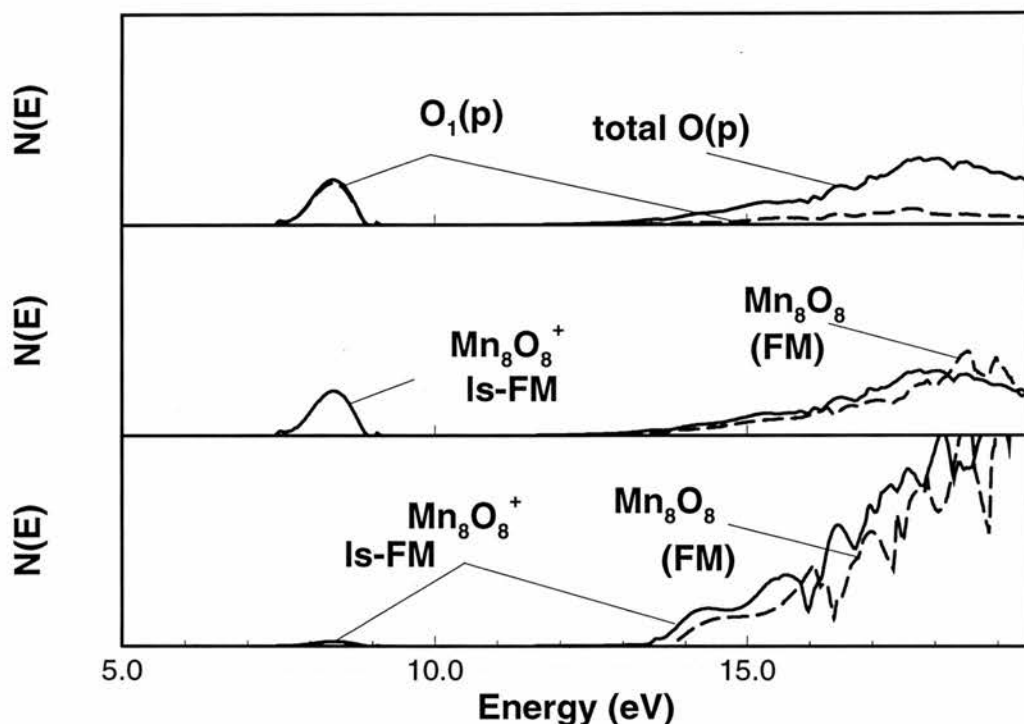


Figure 3.5. Upper panel - comparison of the total empty O(p) (full line) and O_1 projected empty p states (dashed line) of (Is-FM) $Mn_8O_8^{(+)}$; Middle panel - comparison of the total empty O(p) states of (FM) Mn_8O_8 (dashed line) and (Is-FM) $Mn_8O_8^{(+)}$ (full line) ; Lower panel - comparison of the total empty Mn(d) states of (Is-FM) $Mn_8O_8^{(+)}$ (full line) and (FM) Mn_8O_8 (dashed line)

Turning now to the filled valence band states, figure 3.6 shows these for neutral MnO (light dashed line) and Is-FM $Mn_8O_8^+$ (light full line). The states in heavy full and heavy dashed lines are the doubly occupied p_{π} and singly occupied p_{σ} hole site, states belonging to O_1 of Is-FM $Mn_8O_8^+$. It is clear that while these latter states have been shifted to lower energy due to the reduced on site Coulomb repulsion, very little perturbation of the p electrons on neighbouring atoms has taken place as the oxygen p DOS of the other atoms remain very close to those of the neutral system.

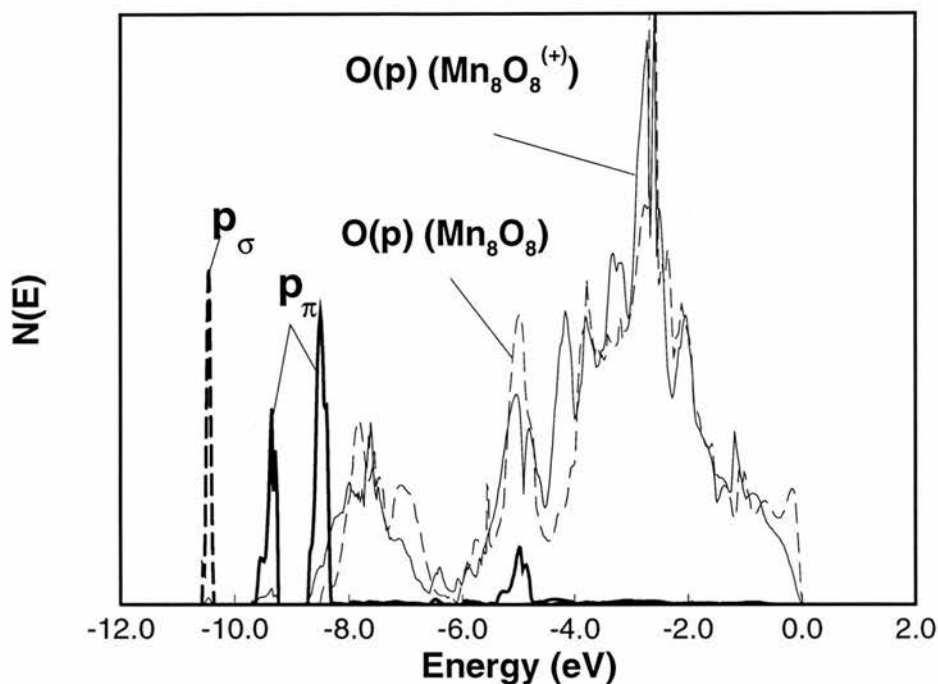


Figure 3.6. Comparison of the valence band (filled) O(p) DOS of (FM) Mn_8O_8 (Light dashed line) and (1s-FM) $Mn_8O_8^{(+)}$ (p_{σ} orbital - heavy dashed line, p_{π} orbital - heavy full line and O(p) - light full line)

Returning now to the AF_{II}^* state of $Mn_8O_8^+$, figures 3.7(a) and 3.7(b) show net charge and spin density plots through a $\{100\}$ basal plane. In figure 3.7(a) the difference in charge density between the neutral and first ionised states of the AF_{II}^* arrangements is plotted with Mn2 as the central atom. The majority of the charge is found on Mn2, but also a substantial distribution is found on the four in plane oxygen atoms. This reflects the Mulliken analysis of 50% charge on Mn2, and 30% on the other four in plane nearest neighbour oxygens. The spin density difference through the same plane is plotted in figure 3.7(b) and again the majority of the spin is found on the central Mn atom with some small dispersion on the other four in plane oxygen atoms.

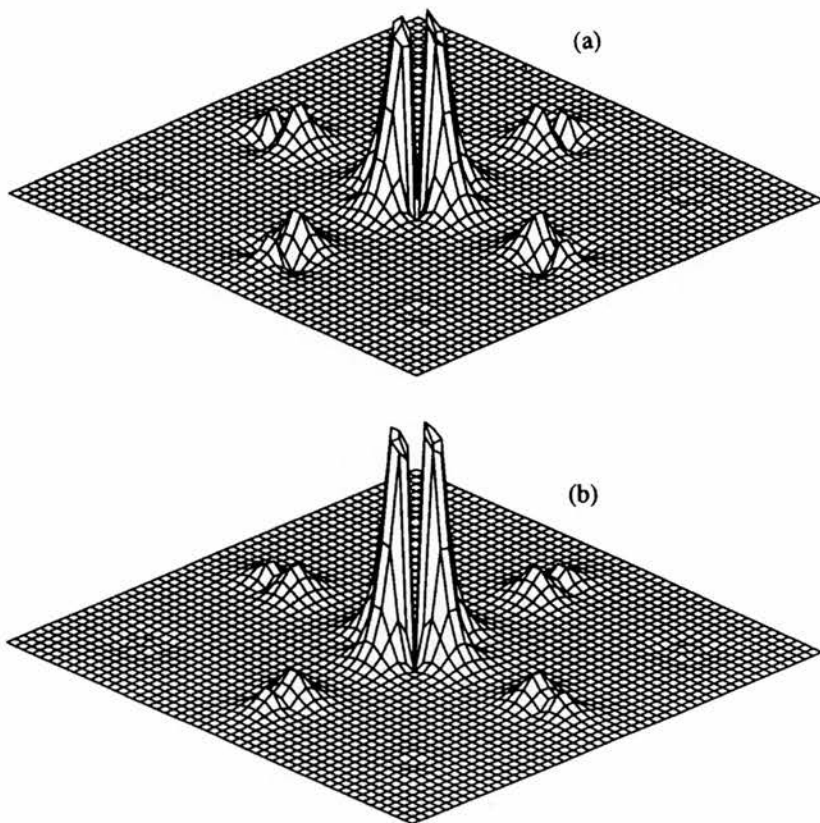


Figure 3.7. Difference in the charge (a) and spin (b) density distributions in a $\{100\}$ basal plane between $(AF_{II}) \text{Mn}_8\text{O}_8$ and $(AF_{II}^*) \text{Mn}_8\text{O}_8^{(+)}$

Turning now to the DOS of $AF_{II}^* \text{Mn}_8\text{O}_8^+$. Figure 3.8 shows a comparison of the empty oxygen p states (upper panel) and empty manganese d states (lower panel) of $AF_{II}^* \text{Mn}_8\text{O}_8^+$ compared with neutral Mn_8O_8 (dashed line). This figure illustrates that for $AF_{II}^* \text{Mn}_8\text{O}_8^+$, the majority of the new empty states, which occur at $\sim 3\text{-}4\text{eV}$ below the conduction band edge, are empty Mn d in nature, but with a small contribution from the empty oxygen p states, which is exactly as suggested by the Mulliken population analyses and the charge and spin density plots. This contrasts with the new states in $1s\text{-FM} \text{Mn}_8\text{O}_8^+$, which are almost exclusively oxygen 2p.

A comparison of the filled upper valence band states of Is-FM Mn_8O_8^+ (upper panel) and $\text{AF}_{\text{II}}^* \text{Mn}_8\text{O}_8^+$ (lower panel) is shown in figure 3.9. It should be noted here that in the upper panel, the oxygen p states have been shifted to lower energy due to the reduced onsite Coulomb repulsion, whereas in the lower panel, the empty d states have been shifted to lower energy. This provides further evidence of oxygen p holes in the ground state, FM-Is Mn_8O_8^+ and manganese d holes in the excited state, $\text{AF}_{\text{II}}^* \text{Mn}_8\text{O}_8^+$.

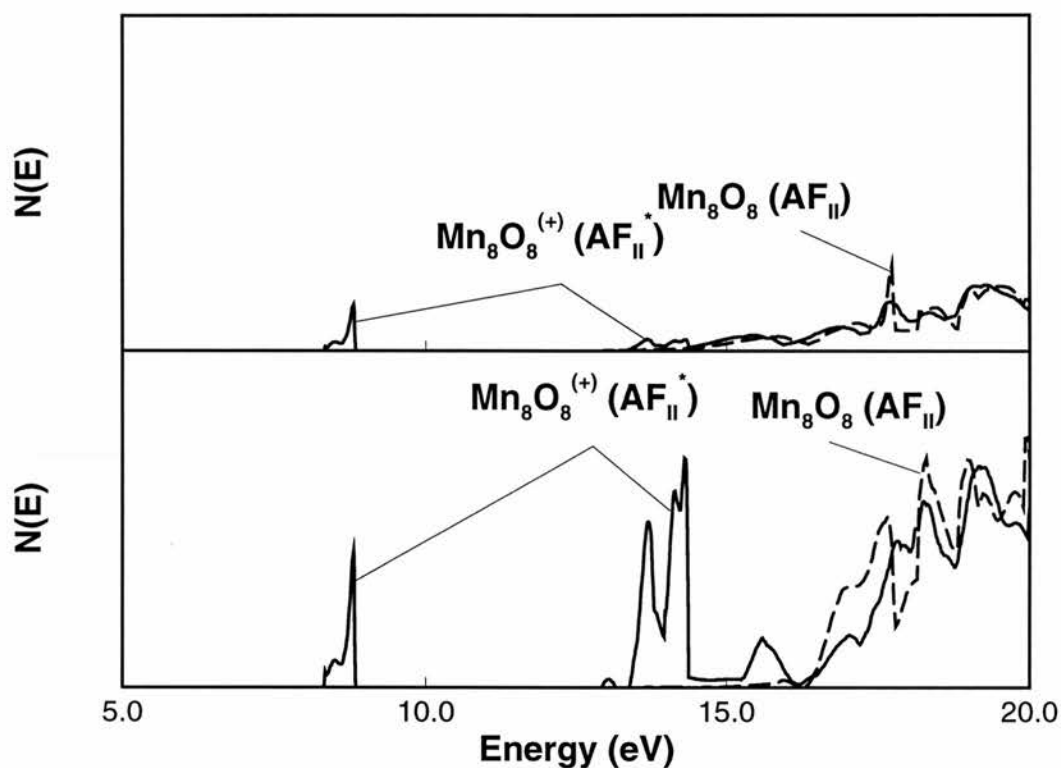


Figure 3.8. Comparison of empty O(p) (upper panel) and Mn(d) (lower panel) DOS of $(\text{AF}_{\text{II}}) \text{Mn}_8\text{O}_8$ and $(\text{AF}_{\text{II}}^*) \text{Mn}_8\text{O}_8^{(+)}$

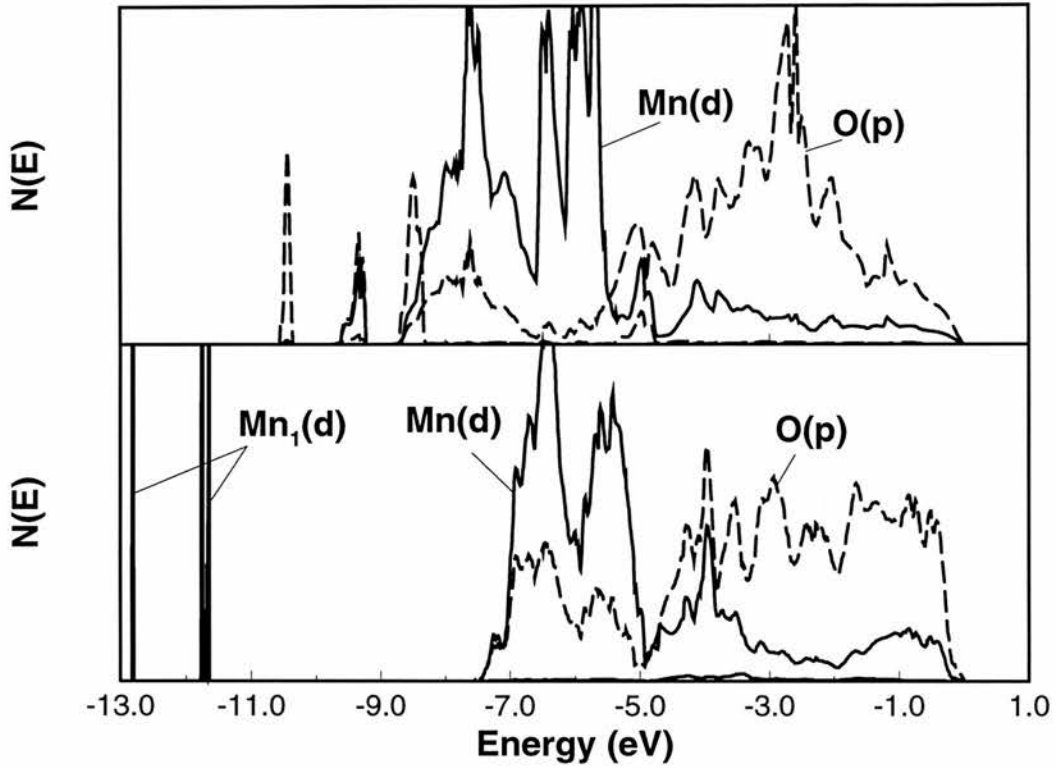
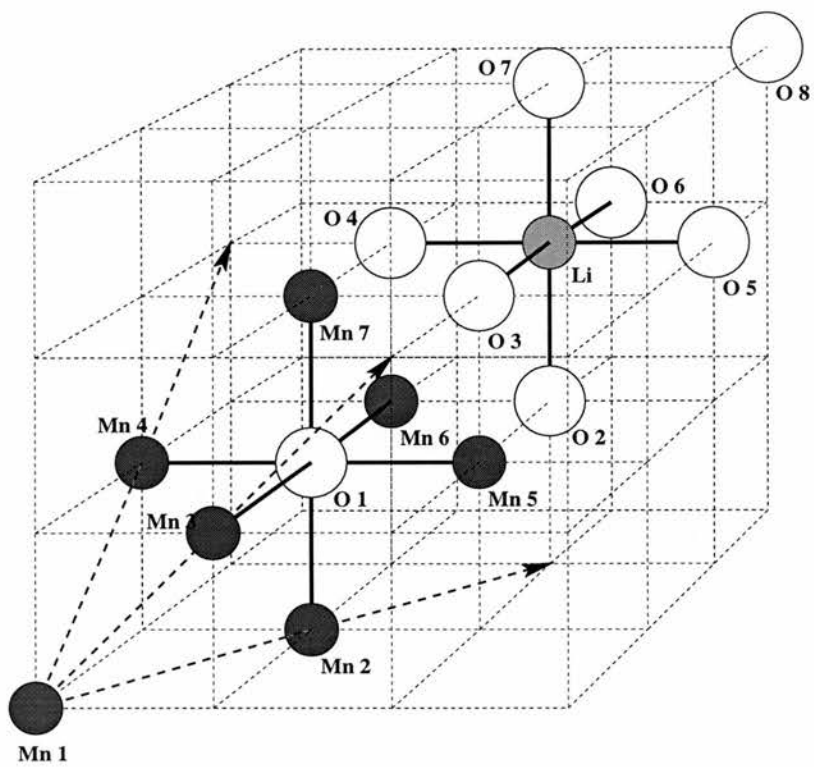


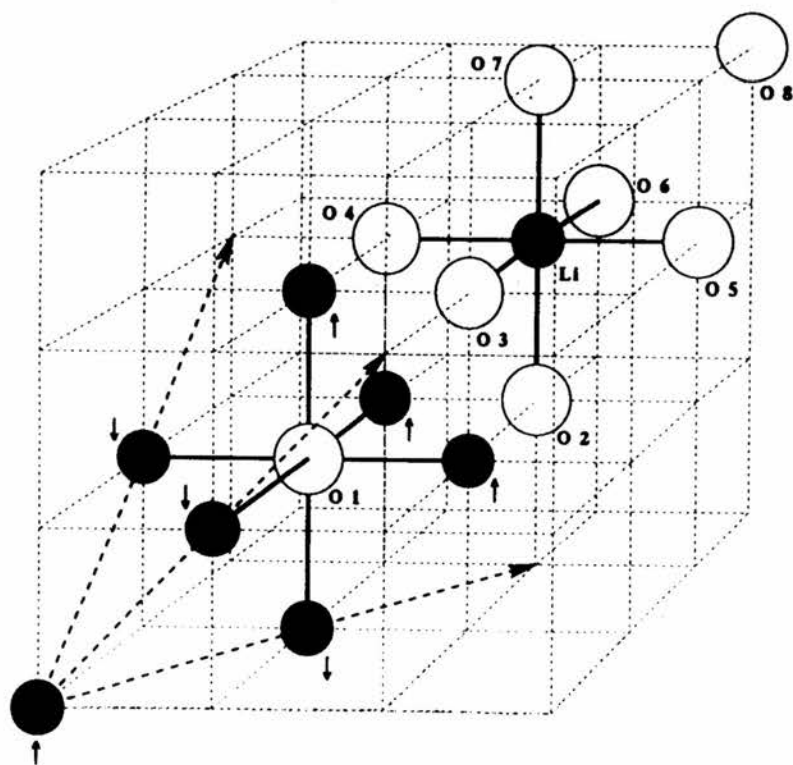
Figure 3.9. Comparison of the valence band DOS of (ls-FM) $\text{Mn}_8\text{O}_8^{(+)}$ (upper panel) and (AF_{II}^*) $\text{Mn}_8\text{O}_8^{(+)}$ (lower panel)

3.2.3 Li:MnO

As in the investigation of the self trapped hole, supercells of MnO were constructed containing eight formula units, with a single substitution of Mn by Li, as shown in figure 3.10(a), to give LiMn_7O_8 or $\text{Li}_{0.125}\text{Mn}_{0.875}\text{O}$. Although this concentration was known to be beyond the limit of solubility of Li_2O in MnO, previous studies on $\text{Mn}_x\text{Ni}_{1-x}\text{O}$ ($M=\text{Mg}$, $N=\text{Mn}$, Ni)¹⁴ and $\text{Li}:\text{NiO}$ ⁸ have suggested that the electronic structure of a more dilute solution would not be very different to $\text{Li}_{0.125}\text{Mn}_{0.875}\text{O}$. The antiferromagnetic spin arrangement (AF_{II}) was used, as shown in figure 3.10(b), where the total net spin of the LiMn_7O_8 supercell was four or six, depending on the direction of the unpaired spin at the hole site, labelled here as low spin (ls) and high spin (hs) respectively.



(a)



(b)

Figure 3.10 The lattice structure (a) and AF_{II} spin arrangement (b) of $LiMn_7O_8$

For the fully symmetric ground state of the $1s\text{-AF}_{II}$ arrangement of LiMn_7O_8 , the unpaired electron delocalises over the six nearest neighbour O atoms to Li in much the same way as it does in Mn_8O_8^+ . As before, breaking the symmetry of the system by an infinitesimal Li displacement in the (001) direction (or equivalent) results in a localised hole (or unpaired electron) in a p_σ orbital of the oxygen atom furthest from the displaced Li. This small displacement, 0.001\AA , reduces the local symmetry of this O site from O_h to C_{4v} and splits the p orbitals into σ and π with respect to Li, with a trapping/localisation energy of 1.37eV . Further relaxation of the Li in the same direction by 0.33\AA away from the hole leads to a relaxation energy of 0.29eV .

Table 3.5 shows the differences in Mulliken population between the neutral AF_{II} spin arrangement of Mn_8O_8 and the ground state LiMn_7O_8 .

δq_M	Ground	Excited
Mn ₁	0.0	+ 0.02
Mn ₂	- 0.04	-0.05
Mn ₃	- 0.01	0.0
Mn ₄	- 0.01	0.0
Mn ₅	- 0.01	0.0
Mn ₆	- 0.01	0.0
Mn ₇	- 0.01	+ 0.40
Li	-	-
O ₁	- 0.01	+ 0.04
O ₂	+ 0.81	- 0.03
O ₃	+ 0.03	+ 0.12
O ₄	+ 0.03	+ 0.12
O ₅	+ 0.04	+ 0.12
O ₆	+ 0.04	+ 0.12
O ₇	- 0.01	- 0.02
O ₈	+ 0.02	+ 0.02

Table 3.5. Differences in the total Mulliken charges, δq_M (e), between AF_{II} Mn_8O_8 and LiMn_7O_8 for the ground and excited hole states

From this it is clear that 80% of the hole is localised at the O2 site (of figure 3.10(a)) which has a local moment of $0.93\mu_B$. This again is very close to the spin moment of formal O^- . Importantly the Mn d^5 configuration remains more or less unchanged with a charge of 1.85e and a local moment of $\pm 4.91\mu_B$ which compares with values of 1.86e and $\pm 4.92\mu_B$ for the undoped system. As in the case of $Mn_8O_8^+$ more extensive relaxation would probably increase the trapping energy; however it is most unlikely that this would alter the Mulliken charges in any significant way.

Direct evidence of the oxygen hole state in Li:MnO is obtained from the charge and spin density plots, especially the spin density which is shown in figures 3.11(a) and 3.11(b). Figure 3.11(a) illustrates the net spin density distribution in a $\{001\}$ basal plane of neutral AF_{II} Mn_8O_8 . The antiferromagnetism is apparent from localised regions of positive and negative spin density which are associated with the four in plane Mn atoms: by symmetry there is no spin distribution at the O sites. Figure 3.11(b) illustrates the comparable spin distribution for ls-AF_{II} $LiMn_7O_8$. The Li substitution site is evident from the *missing* positive spin density compared with the spin density distribution of the undoped system. Now the central oxygen atom has acquired spin, in the characteristic p_e shape, as predicted by the Mulliken charge and spin population analyses. The spin density on the other Mn and O sites remains virtually unchanged.

More confirmation of the nature of the hole state in ls-AF_{II} $LiMn_7O_8$ is obtained from the single particle DOS. The middle panel of figure 3.12 shows a comparison of the empty p states of neutral Mn_8O_8 (dashed line) with ls-AF_{II} $LiMn_7O_8$ (full line). On Li substitution, new empty O(p) states occur $\sim 3-4eV$ below the conduction band edge with very little change in the conduction band from neutral Mn_8O_8 . The upper panel shows the total empty O(p) states of ls-AF_{II} $LiMn_7O_8$ and those projected onto O2. From this it is apparent that the new states are highly localised and can be almost exclusively associated with O2. This is confirmed in the lower plot of empty manganese d states of the neutral (long dashed) and Li doped (full line) Mn_8O_8 systems, where the contribution to the new empty states of $LiMn_7O_8$ AF_{II} from manganese is almost negligible.

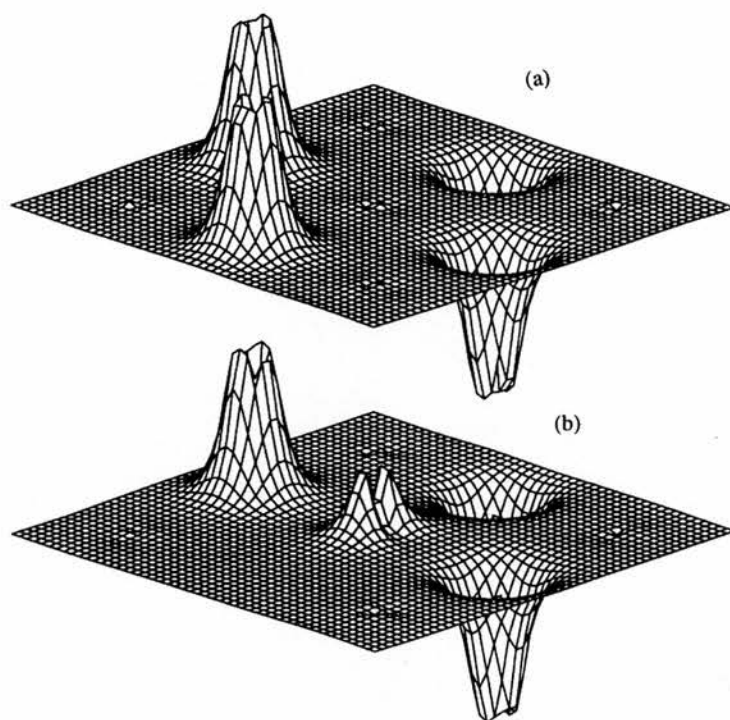


Figure 3.11. Net spin density distribution in a {001} basal plane of AF_{II} Mn₈O₈ (a) and ls-AF_{II} LiMn₇O₈ (b)

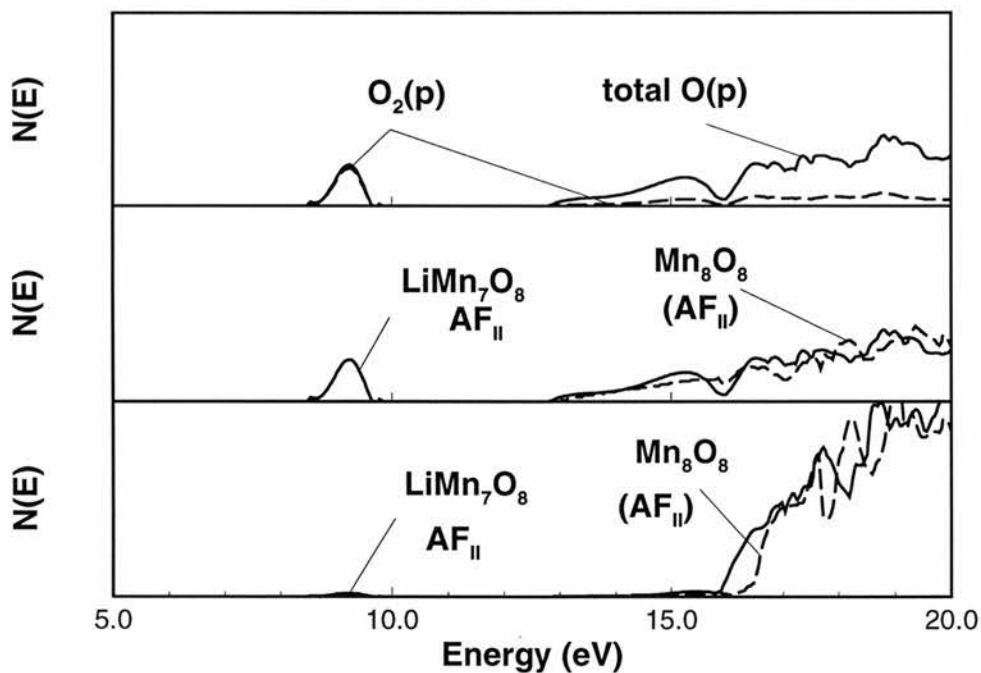


Figure 3.12. Upper panel - comparison of the total empty and O₂ projected empty O(p) DOS of LiMn₇O₈ ; Middle panel - comparison of the total empty O(p) DOS of ls-AF_{II} LiMn₇O₈ and AF_{II} Mn₈O₈ ; Lower panel - comparison of the total empty Mn(d) DOS of ls-AF_{II} LiMn₇O₈ (full line) and AF_{II} Mn₈O₈ (dashed line)

As mentioned previously, UHF calculations for Mn_8O_8^+ find an excited state of the self trapped hole $\sim 1\text{eV}$ above the $d^5\bar{L}$ ground state in which $\sim 85\%$ of the hole is localised at a single Mn and four nearest neighbour oxygen sites. From the Mulliken population analysis of hs- AF_{II} LiMn_7O_8 , a similar diffuse hole state is found both in the fully symmetric and broken symmetry configurations. This excited state occurs at $\sim 1.3\text{eV}$ above the ground state with $\sim 40\%$ of the hole localised at the Mn7 site, figure 3.10(a), nearest neighbour to Li and $\sim 50\%$ delocalised over four nearest neighbour oxygen sites which are coplanar with Li and Mn7. Table 3.5 contains the Mulliken population differences between this excited state and the undoped system. For Mn7 the 3d population is 4.66 with a local moment of $\sim 4.2\mu_{\text{B}}$ which compares with the formal moment of Mn(III) of $4\mu_{\text{B}}$. In view of this, this excited state is referred to as *weakly* d^5 . The charge and spin density difference distributions between this weakly d^5 state and neutral Mn_8O_8 confirm the Mulliken population analyses and are shown in figures 3.13(a) and 3.13(b). Figure 3.13(a) illustrates the charge density difference projected onto a $\{001\}$ basal plane. The majority of localised density is found at the central Mn site with the rest distributed equally over the four in plane oxygen sites. The spin difference distribution of the same plane is plotted in figure 3.13(b). Again the majority of the spin difference is found at the central Mn with a small dispersion over the oxygen positions.

As before, further insight into the nature of the AF_{II}^* state can be obtained from the empty O(p) and Mn(d) DOS. Figure 3.14 illustrates the empty O(p) states (upper) and empty Mn(d) states (lower) of neutral Mn_8O_8 (dashed line) and AF_{II}^* LiMn_7O_8 (full line). This clearly shows that new empty O(p) and Mn(d) states occur in LiMn_7O_8 AF_{II}^* , with the majority Mn(d) in nature. This agrees completely with the Mulliken charge difference analysis which suggests that $\sim 40\%$ of the hole is localised at the Mn7 site.

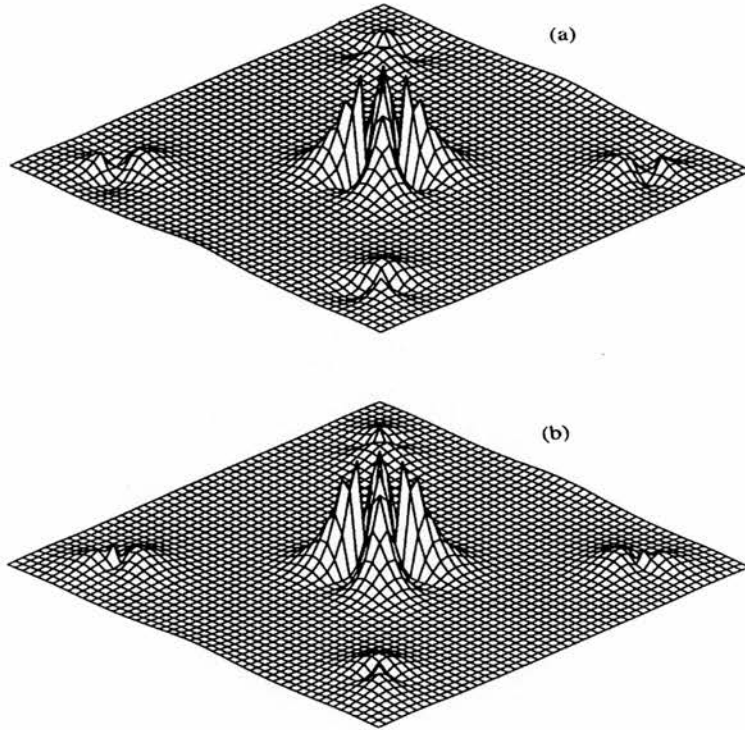


Figure 3.13. Charge (a) and spin (b) density difference between neutral Mn_8O_8 and $\text{LiMn}_7\text{O}_8 \text{AF}_{\text{II}}^*$ projected onto a $\{001\}$ basal plane

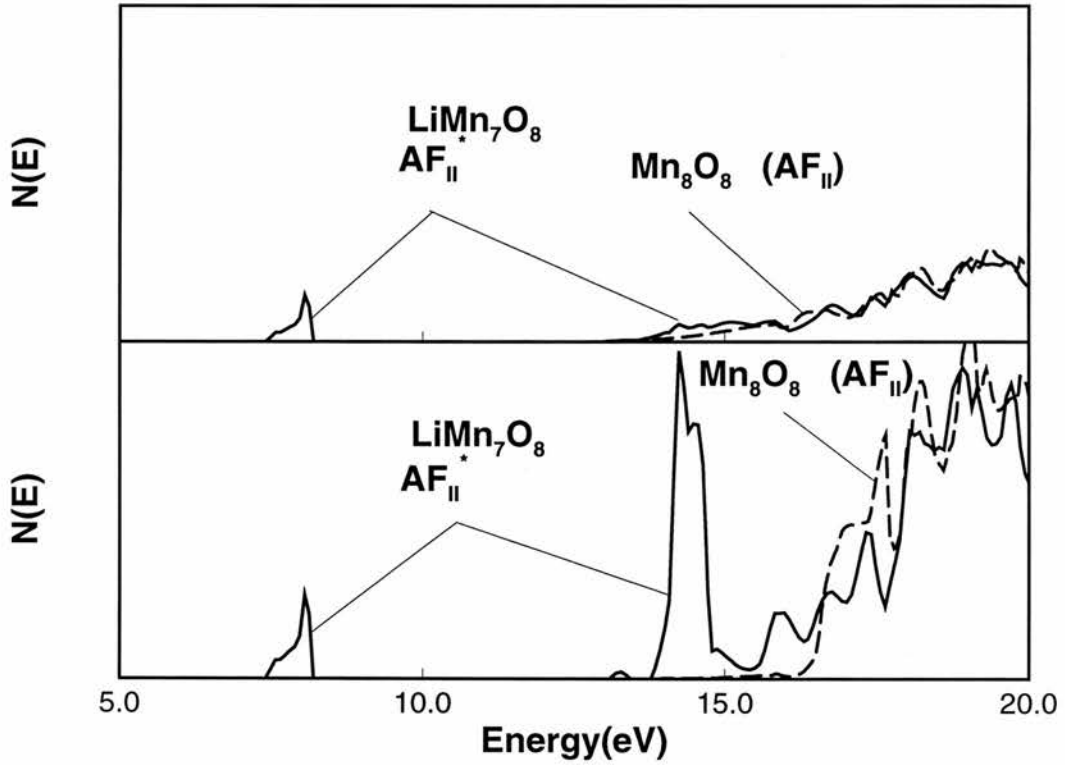


Figure 3.14. Comparison of the empty O(p) states (upper panel) and the empty Mn(d) states (lower panel) of neutral $\text{Mn}_8\text{O}_8 \text{AF}_{\text{II}}$ with $\text{LiMn}_7\text{O}_8 \text{AF}_{\text{II}}^*$

A comparison of the valence band DOS of ground state LiMn_7O_8 AF_{II} (upper) and the excited state, AF_{II}^* (lower) is shown in figure 3.15. In the upper panel, the O(p) states have been shifted to lower energy, whereas in the lower panel, it is the Mn(d) states. This is due to a reduction in the onsite Coulomb repulsion as observed previously for the valence band DOS of Is-FM and $\text{AF}_{\text{II}}^* \text{Mn}_8\text{O}_8^+$ shown in figure 3.9.

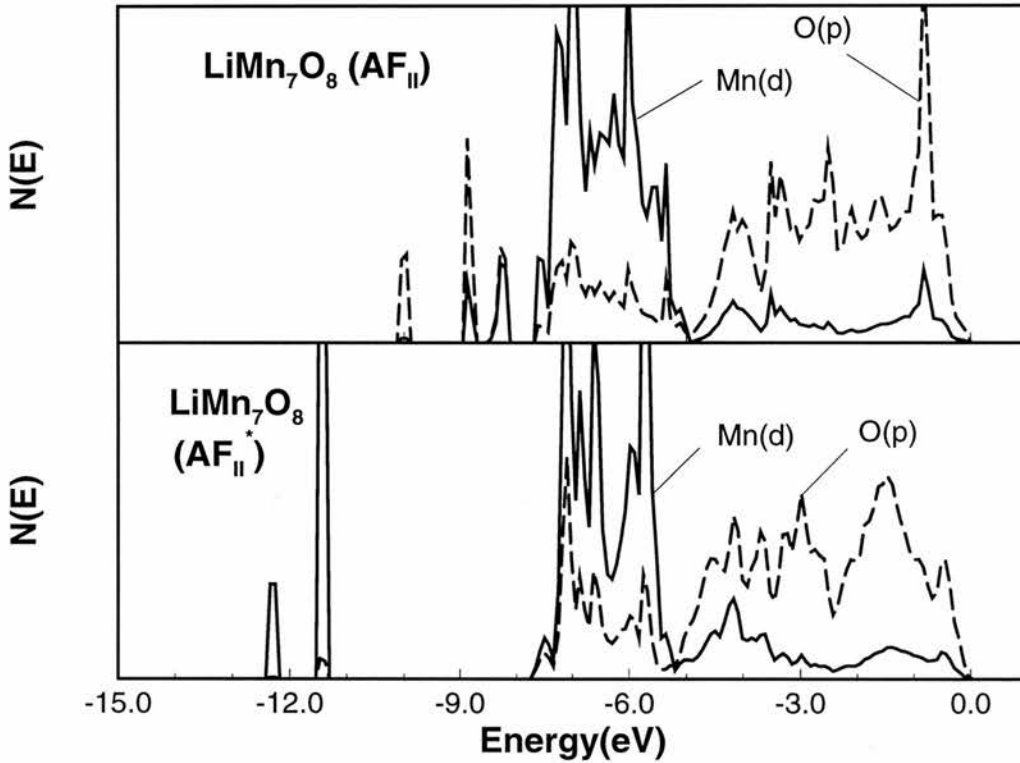


Figure 3.15. Comparison of the valence band DOS of LiMn_7O_8 AF_{II} (upper) with LiMn_7O_8 AF_{II}^* (lower)

To summarise the results of Li:MnO broken symmetry calculations, the ground state of LiMn_7O_8 is low spin $d^5\bar{L}$ with a highly localised $\text{O } p_e$ hole. There is no change to the Mn valence, d^5 , in keeping with the p-d charge transfer description of MnO suggested previously. A low lying excited state occurs $\sim 1.3\text{eV}$ above the ground state which is similar to the excited self trapped hole in MnO. This further supports the intermediate position of MnO in the ZSA phase diagram².

3.2.4 Electron addition states in MnO

Although it is clear that the first electron addition state in MnO is Mn(d), it is of interest to determine if electrons can self trap as holes can or if an aliovalent substitution is required, such as the substitution of F for O, to facilitate self trapping.

As before, eight unit supercells were used, and one electron was added to the ferromagnetic lattice and found to delocalise over all eight Mn in the fully symmetric case. Symmetry breaking in the way described previously leads to self trapping with ~76% of the electron localised at a single Mn site. However unlike the self trapped hole, the energy of the self trapped electron is found to be 0.24eV higher in energy than the delocalised state. A relaxed minimum energy structure is found, as before, with a localisation energy of 0.07eV for a nearest neighbour O displacement of 0.13 Å. Even in this relaxed state, the energy of the localised electron is higher than that of the delocalised state.

In order to determine if the localised state could be stabilised with substitution, UHF calculations were performed on Mn₈O₇F. Here 77% of the added electron density localises at the Mn nearest neighbour to F with an energy of 1.32eV lower than the symmetric delocalised state. The energy differences between the FM electron states of Mn₈O₈⁻ and Mn₈O₇F relative to the infinitesimally distorted FM state are summarised in table 3.6

Electron State	ΔE	$\Delta E'$
FM	0.0	0.0
FM (relaxed)	- 0.08	- 0.07
FM (symmetric)	- 0.24	+ 1.32

Table 3.6. Energies, ΔE and $\Delta E'$ (eV), of the electron addition state Mn₈O₈⁽⁻⁾ and Mn₈O₇F relative to the infinitesimally distorted FM state.

Figures 3.16(a) and 3.16(b) show the charge and spin density differences in a {100} basal plane between neutral ferromagnetic Mn₈O₈ and the first electron addition state of ferromagnetic Mn₈O₈. As for the first ionised state, the net

charge and spin density plots provide direct evidence of the difference in charge or spin distribution in the system. From figure 3.16(a), it is evident that the majority of the additional charge resides on the central Mn atom in a d_{xy} orbital, but with some dispersion on the other surrounding in plane oxygen and manganese atoms. From the net spin density plot, figure 3.16(b), of the same plane, however, it is clear that the spin resides only on the central Mn atom, with very little dispersion elsewhere.

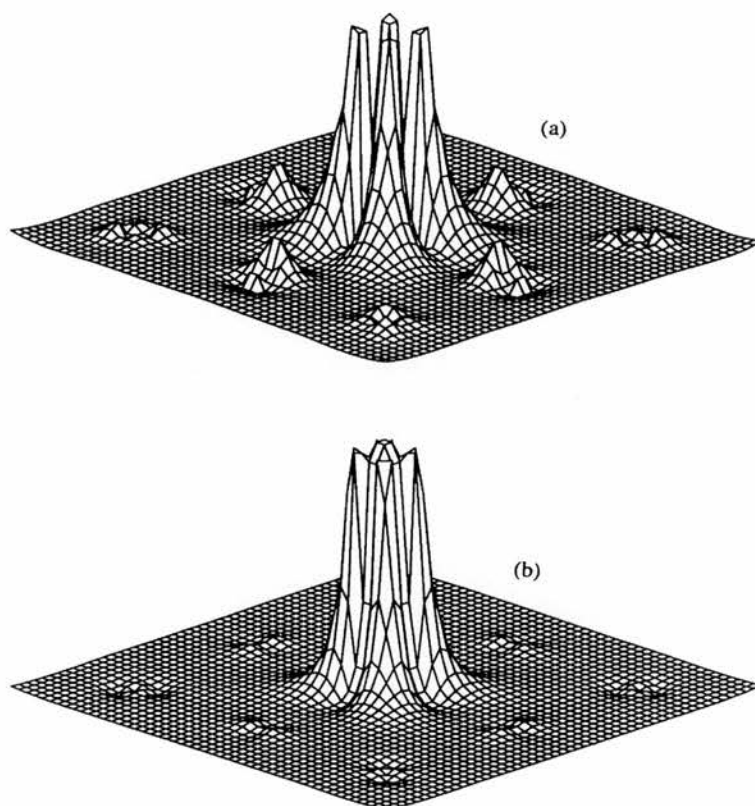


Figure 3.16. Difference in charge density distributions in a basal {100} plane between (FM) Mn_8O_8 and (FM) $Mn_8O_8^{(-)}$

3.3. Discussion

All electron UHF calculations have been carried out on the electron hole and electron addition states of MnO and the Li doped system in order to clarify the resulting electronic structures in terms of the ZSA phase diagram². The AF_{II} and the FM spin configurations of $Mn_8O_8^+$ and AF_{II} $LiMn_7O_8$ all yield localised oxygen holes as observed previously in NiO^9 . The localisation energies in

Mn_8O_8^+ range from 2.33 to 2.51eV which compares with 3.3eV for NiO^9 . From the direct evidence presented on Mn_8O_8^+ , this study suggests that MnO is a high spin p-d charge transfer insulator with localised free holes, which is in full agreement with a spectroscopic study by Becker *et al*¹⁵. For the fully symmetric hole state, the electron hole is distributed evenly between the six symmetry equivalent oxygen atoms resulting in a metallic solution. An infinitesimal distortion of the lattice, which reduces the local symmetry of a single O site from O_h to C_{4v} , localises the hole at this site. A likely reason for the stability of the localised state is that it increases the polarisation energy of the hole which is proportional to the effective charge squared. Therefore the polarisation energy associated with the localised hole is approximately six times greater than that of the delocalised hole. It is stabilised further by a lattice relaxation away from the hole resulting in a displacement dipole. This was also found previously for Li:NiO^8 and NiO^9 while esr measurements suggest that this is also the case for Li:MgO^{16} .

Further evidence to support the existence of oxygen holes in MnO comes from the Mulliken analyses, the projected DOS and charge and spin density distributions in Mn_8O_8^+ and LiMn_7O_8 . Differences in the Mulliken charge populations between the AF_{II} spin arrangement of Mn_8O_8 and LiMn_7O_8 suggest that ~80% of the bound hole is localised at a single O site adjacent to Li giving a $d^5\bar{L}$ ground state. This is exactly the same state found for the free hole in the AF_{II} spin arrangement of Mn_8O_8^+ . Direct confirmation of the oxygen hole state in AF_{II} LiMn_7O_8 also comes from the charge and spin density distributions, which confirm the Mulliken charge and spin population analyses. The fully symmetric hole state in LiMn_7O_8 differs from the fully symmetric free hole in that it is insulating. However as in Mn_8O_8^+ , an infinitesimal distortion of the lattice reduces the symmetry leading to localisation of the hole at a single O site. Further relaxation results in a lowering of the energy by 0.29eV which is close to the activation energy of hole hopping in Li:MnO^{17} . This compares with the range of relaxation energies, 0.14-0.2eV, found for the various spin states of Mn_8O_8^+ . LiMn_7O_8 not only provides direct evidence of O(p) holes but also confirms the similarities between the free hole state and the bound hole state in Mn_8O_8 . Figure

3.17 illustrates a comparison of the empty O(p) (full line) and empty Mn(d) (dashed line) DOS between Mn_8O_8^+ Is-FM (upper panel) and LiMn_7O_8 AF_{II} (lower panel). In both plots, new empty states of ~1eV width are clearly visible. These states are predominantly O(p) with some small Mn(d) contribution and are separated from the conduction band lower edge by a gap of ~3eV. The overall shape of the conduction band is broadly similar in both cases with slight differences in relative distribution of states at the lower edge due to the reduction in Mn(d) states on going from Mn_8O_8^+ to LiMn_7O_8 .

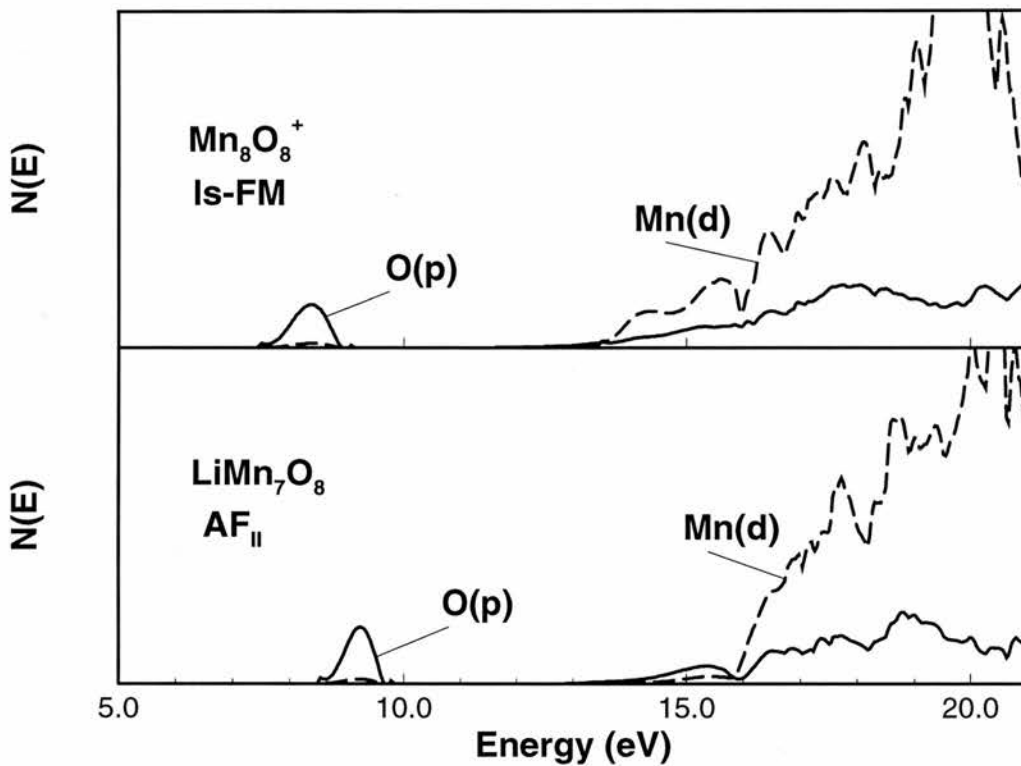


Figure 3.17. Comparison of the empty O(p) (full line) and empty Mn(d) (dashed line) DOS between Mn_8O_8^+ Is-FM (upper panel) and LiMn_7O_8 AF_{II} (lower panel)

The magnitude of the magnetic effects associated with the free hole state in Mn_8O_8^+ can be deduced from the three calculated spin configurations, the order of stability of which is $E(\text{Is-FM}) < E(\text{AF}_{II}) < E(\text{hs-FM})$. Two main effects were responsible for this: Pauli repulsion and spin-spin stabilisation. The unpaired spin is confined at the oxygen site in Is-FM relative to hs-FM and AF_{II} due to Pauli

repulsion, as the increase in kinetic energy is much greater in hs-FM and AF_{II} than the direct spin-spin stabilisation energy, which was concluded from energy differences (table 3.4) of 0.71eV and 0.29eV for E_p(hs-FM) and E_p(AF_{II}) respectively.

The first ionised state of MnO is often thought to involve a Jahn Teller distortion of Mn³⁺ which removes the degeneracy of the Mn d⁴ state¹. However, UHF calculations reported here suggest that, lattice relaxation results in a localised O hole leading to an interpretation of the Jahn Teller distortion in terms of O p⁵ rather than Mn d⁴. This agrees with a previous UHF study of the hole states in NiO, where the Jahn Teller distortion similarly results from the O p⁵ state and not the Ni d⁷ configuration as generally accepted.

As well as the d⁵ \underline{L} ground state, found for Mn₈O₈⁺ and LiMn₇O₈, excited states, ~d⁴, were found 0.7eV and 1.28eV higher in energy respectively. This makes sense in terms of the position of MnO in the ZSA phase diagram² and correlates with the findings of ZSA and van Elp *et al*³ who found d⁵ \underline{L} and d⁴ states with relative weights of 0.5 and 0.42 respectively. Using the same terminology as ZSA², the difference in energy between the d⁵ \underline{L} and d⁴ states $\approx \Delta - U$, where Δ = charge transfer energy and U = d-d Coulomb interaction energy, van Elp *et al*³ found $\Delta - U = 0.3\text{eV}$, which compares with 0.7eV and 1.28eV from UHF calculations for the AF_{II} spin arrangements of Mn₈O₈⁺ and LiMn₇O₈ respectively. For electron addition, the ⁵T_{2g} (d⁶) state found was in agreement with van Elp *et al*³, who reported ⁵T_{2g} 1.0 eV lower in energy than ⁵E_g, but with approximately equal contributions to the BIS spectrum³. The free state was predicted to be delocalised which was consistent with measurements of Hall mobility of n-type MnO, which was over 3 orders of magnitude greater than that of p-type MnO¹⁷ at elevated temperatures. Substitution of F⁻ was predicted to localise the electron addition state with a stabilisation energy of ~1.5eV.

3.4. Conclusions

The main conclusions from this chapter are: (1) that MnO is a p-d charge transfer insulator with the ground state hole d⁵ \underline{L} (⁵E_g); (2) that the free hole and the bound hole are localised on a single oxygen atom and are practically identical; (3)

that the unpaired electron associated with the free hole is a spin polaron with a 'bag' of antiferromagnetic nearest neighbours; (4) that the lattice distortion which is found to accompany the self trapped hole and the bound hole is associated with the oxygen p^5 state and not manganese d^4 as widely accepted; (5) that on the addition of an electron, the ground state is delocalised; (6) that on substitution of F, an electron localises as Mn d^6 adjacent to F in a $^5T_{2g}$ state; (7) that the results of the Mulliken population analyses are entirely consistent with the atom projected densities of states and the charge and spin density distributions; (8) that the nature of the states which span the band gap in MnO provide a good guide as to the nature of the hole and electron addition states.

References

1. P.A.Cox, 1990 ' *Transition Metal Oxides* ', Oxford University Press .
2. J.Zaanen, G.A.Sawatzky, and J.W.Allen, 1984 *Phys.Rev.Lett.* **55**, 418
3. J.vanElp, R.H.Potze, H.Eskes, R.Berger and G.A.Sawatzky, 1991
Phys.Rev.B, **44**,1530
4. A.Svane and O.Gunnarsson, 1990 *Phys.Rev.Lett.* **65**, 1148
5. K.Terakura, T.Oguchi, A.R.Williams and J.Kuebler, 1984 *Phys.Rev. B*,
30, 4734
6. W.C.Mackrodt, N.M.Harrison, V.R.Saunders, N.L.Allan, M.D.Towler,
E.Aprà, and R.Dovesi, 1993 *Phil.Mag. A*, **68**, 653
7. M.D.Towler, N.L.Allan, N.M.Harrison, V.R.Saunders, W.C.Mackrodt,
and E.Aprà, 1994 *Phys.Rev. B*, **50**, 5041
8. W.C.Mackrodt, N.M.Harrison, V.R.Saunders, N.L.Allan and
M.D.Towler, 1996 *Chem.Phys.Lett.* **250** 66
9. W.C.Mackrodt, 1997 *Ber.Bunsenges.Phys.Chem.* **101**, 169
10. P.Kuiper, G.Kruizinga, J.Ghijssen and G.A.Sawatzky, 1989
Phys.Rev.Lett., **62**, 221
11. J.van Elp, B.G.Searle, G.A.Sawatzky and M.Sacchi, 1991 *Solid State
Comm.* **80**, 67
12. J.van Elp, H.Eskes, P.Kuiper and G.A.Sawatzky, 1992 *Phys.Rev. B*, **45**,
1612
13. C.Springhorn and H.Schmalzried, 1994 *Ber. Bunsenges. Phys. Chem.* **98**,
746
14. M.D.Towler, N.L.Allan, N.M.Harrison, V.R.Saunders and
W.C.Mackrodt, 1995 *J. Phys. C :Condensed Matter Physics* **7**, 6231
15. K.D.Becker and T.He, 1992 *Ber.Bunsenges.Phys.Chem.* **96**, 1886
16. M.M.Abraham, Y.Chen and W.P.Unruh, 1974 *Phys.Rev. B*, **9**, 1842
17. C.Crevecoeur and H.J.de Wit, 1970 *J.Phys.Chem.Solids* **31**, 783

Chapter 4

MnO at High Pressure

4.1. Introduction

In the previous chapter the electronic structure of the hole and electron addition states in fcc (B1) (Fm3m) MnO were investigated. This chapter is also devoted to MnO, its structure and properties at high pressure, in light of a recently observed shock induced phase transition at 90GPa¹.

The B1 (Fm3m) phase of the earth metal monoxides, CaO, SrO and BaO are all known to undergo a pressure induced phase transition^{2,3,4} to the B2 (Pm3m) phase or in the case of BaO, a distorted B2 phase at room temperature. The phase transition pressures for these oxides range from ~14GPa for BaO through to ~60GPa for CaO, increasing with the decrease in cation radius. As yet this transition is not observed in MgO, which has a much smaller cation radius than the heavier alkali earth monoxides, but it is thought to occur at pressures greater than 227GPa, up to which pressure the B1 phase is found to be stable⁵. The transition metal monoxides on the other hand do not follow such a neat trend. The B1 phase of FeO is found at ambient temperature and pressure but under shock compression it undergoes a phase transition at 70GPa^{6,7} to the NiAs (P63/mmc) (B8) structure⁸ which has been confirmed as conducting^{9,10} and unstable at low temperatures¹¹. No structural phase transitions have been observed for NiO although it does undergo an insulator metal transition at 200GPa¹². Recently Noguchi *et al*¹ reported a pressure induced phase transition from the B1 phase of MnO at ~90GPa which was accompanied by a decrease in volume by ~8%. These shock wave experiments, which were carried out over the pressure range 41-114GPa, have confirmed previous static compression results¹³ up to 60GPa. Noguchi *et al*¹ have interpreted this high pressure phase of MnO as B2 due to the magnitude of the phase transition pressure and also the size of the cation radius in MnO, both of which appear to follow the trend of the alkaline earth monoxides. Two questions arise: (1) is the high pressure phase of MnO, a simple B2 phase (as in CaO²), a distorted B2 phase (as in BaO⁴), or even a B8 phase (as in FeO⁸); (2) is the high pressure phase conducting as in FeO^{9,10} and

NiO¹², even though no evidence of metallisation has been found up to 50GPa¹⁴? The purpose of this investigation is to answer the above questions. In view of the success of UHF calculations in predicting correctly the spin lattice interaction (magnetostriction) of the B1 phase of MnO and NiO at ambient pressure, investigations have been carried out into the spin lattice interaction of the B1 phase of MnO as a function of pressure. In addition, the variation of the valence electron structure including the band width and conductivity gap is also studied as a function of pressure.

4.2.Results

4.2.1 Low pressure phase

It was found experimentally that the the high pressure phase of MnO obtained from shock compression of the B1 phase at 90GPa was ~8% less in volume than the B1 phase¹. Therefore to determine possible high pressure phases of MnO, direct energy minimisation of the lattice structures, B1(Fm3m), B2(Pm3m), blende(F43m), wurtzite(P63mc) and NiAs(P63(mmc)) was carried out using the FM spin arrangements and their volumes were compared with that found for the B1 structure. The order of stability, lattice parameters and corresponding volumes are shown in table 4.1.

Structure	Sp. Group.	$\Delta E_{\text{HF}}(\text{eV})$	$a(\text{\AA})$	$c(\text{\AA})$	$V(\text{\AA}^3)$
B1	Fm3m	0.0	4.524*	-	23.149
wurtzite	P6 ₃ mc	0.13	3.477	5.550	29.058
blende	F43m	0.21	4.877	-	29.003
NiAs(B8)	P6 ₃ /mmc	0.38	3.140	5.520	23.570
B2	Pm3m	1.59	2.774	-	21.349

Table 4.1. Comparison of Hartree-Fock optimised structures and energies of MnO

$$* a_{\text{fcc}}(\text{expt}) = 4.445 \pm 0.001 \text{ \AA}$$

As expected, the B1 phase is found to be the most stable. The unit cell volumes are found to increase in the order $B2 < B1 < B8 < \text{blende} < \text{wurtzite}$. Thus from predictions at the UHF level, the only likely candidate for the high pressure phase of MnO is B2 (or some variant of it) and furthermore since the stabilising influence of electron correlation increases with a decrease in volume, the inclusion of electron correlation would stabilise further the B1 and B2 with respect to the other phases. The ferromagnetic spin arrangements were used during the optimisations as it has been shown previously that the energy difference between the magnetic states is negligible when compared with the difference in energy between phases^{15,16}. For example, the energy difference between the FM and AF_{II} spin arrangements of the B1 phase of MnO was calculated as 0.006eV ^{15,17}, whereas the energy difference between the B1 and B2 phases themselves is found to be $\sim 1.6\text{eV}$. From these initial calculations, the only possible high pressure phase would seem to be B2 as it is the only phase which is predicted to have a lower volume than that of the B1 structure. In view of this, structural optimisations including *a posteriori* correlation correction to the total energy based on the Perdew functional were carried out only for the B1 and B2 phases. These energies are referred to as E_{HFP} , as distinct from the Hartree-Fock energies of E_{HF} , and are shown in table 4.2.

Structure	Sp. Group.	$\Delta E_{\text{HFP}}(\text{eV})$	$a(\text{\AA})$	$V(\text{\AA}^3)$
B1	Fm3m	0.0	4.392	21.180
B2	Pm3m	1.34	2.662	18.864

Table 4.2. Comparison of Hartree-Fock-Perdew optimised structures and energies of the Fm3m and Pm3m phases MnO

If as a first approximation, the transition pressure, p^{\dagger} , is represented by $p^{\dagger} \approx -\Delta E/\Delta V$, where ΔE and ΔV are the differences in energy and volume between the B1 and B2 phases respectively, then the transition pressures corresponding to the HF and HFP energies would be $\sim 142\text{GPa}$ and $\sim 93\text{GPa}$ respectively, with the

latter, in particular, close to the phase transition pressure reported by Noguchi *et al*¹.

4.2.2 High pressure phase

Calculations for the B1 structure down to a lattice parameter of 3.87Å, which corresponds to pressures of ~211GPa and ~181GPa and reduced volumes of ~0.63 and ~0.68 on the HF and HFP scales respectively, show that MnO retains its high spin insulating character both in the FM and AF_{II} spin arrangements.

The pressure, p , is estimated by numerical differentiation of the HF or HFP energy with respect to volume, V ,

$$p = \frac{-dE(V)}{dV} = p(V)$$

Then the Gibbs free energy, $G(p, V)$, is approximated by the expression,

$$G(p, V) = E(V) - V \left[\frac{dE(V)}{dV} \right]$$

and the transition pressure, p^t is defined as the pressure for which

$$G_I(p, V_I) = G_{II}(p, V_{II})$$

This is obtained graphically from the intersection of the free energy versus pressure curves for the two phases.

At the lattice parameter of 3.87Å, the difference in the reduced volumes between the FM and AF_{II} spin arrangements is <0.3%, which implies that the phase transition pressure would be unaffected by the magnetic state. Figure 4.1 shows the calculated Hugoniot for the FM and AF_{II} B1 phases of MnO derived from HF energies and also that of FM B1 based on HFP energies. These are compared with two sets of experimental data obtained from static compression by Jeanloz *et al*¹³ and from shock compression by Noguchi *et al*¹. Very good agreement is observed between the static data and the calculated Hugoniot up to the limit of the data, ~60GPa, which suggests that the undistorted B1 phase is stable up to this pressure.

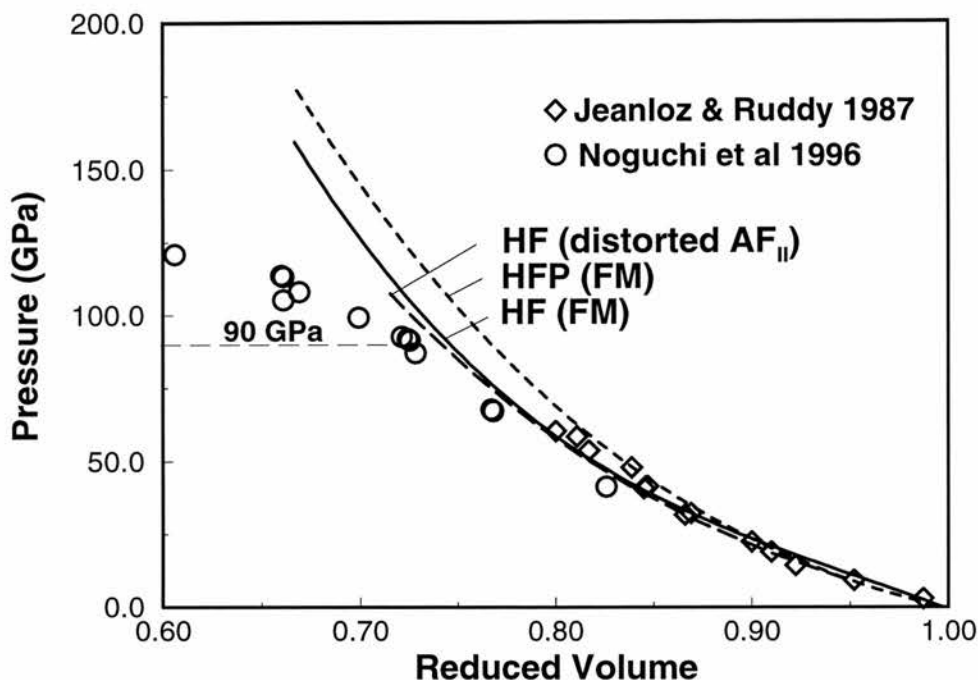


Figure 4.1. A comparison of calculated and experimental Hugoniot of MnO.

Turning now to the B2 phase of MnO, it is found to be high spin insulating down to 2.747 Å, below which the UHF solutions become conducting. Thus UHF calculations predict the B2 phase to remain insulating up to HF and HFP pressures of ~118GPa and ~93GPa respectively, which correspond to reduced volumes of 0.75 and 0.83. The metallic B2 phase was not investigated further as it is well known that Hartree-Fock theory does not provide a good description of the conducting state. Figure 4.2 shows a plot of the calculated HF free energies as a function of pressure for the B1 and B2 phases, from which it is clear that B1 is lower in energy than B2 up to the pressure at which the UHF solutions for the B2 phase remain insulating. Therefore UHF calculations do not predict directly a phase transition in MnO from an insulating undistorted B1 phase to an insulating undistorted B2 phase. A cubic extrapolation of the free energy versus pressure curve for B2 (the heavy dashed line of figure 4.2) leads to a hypothetical HF transition pressure (to the hypothetical insulating B2 phase) of ~160GPa with a corresponding HFP value of ~149 GPa.

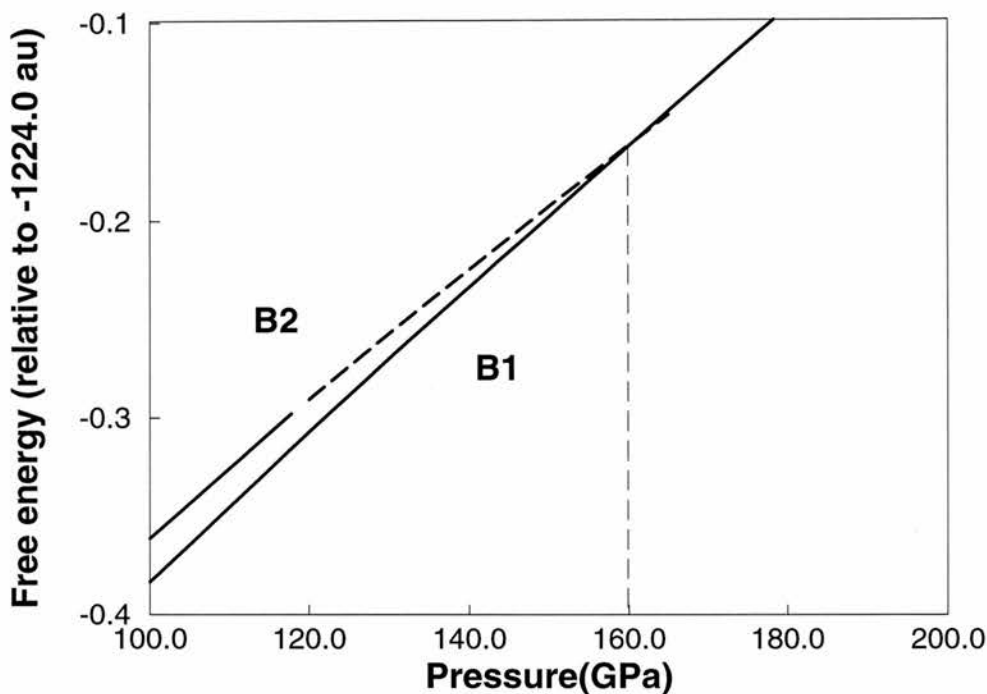


Figure 4.2. Calculated free energies as a function of pressure for the Fm3m and Pm3m structures of MnO (Full lines are the HF values; the dashed line a cubic extrapolation of the Pm3m values)

It has been shown experimentally that the AF_{II} spin arrangement of the MnO B1 phase involves a spin lattice interaction which results in a small rhombohedral distortion of the fcc structure at ambient temperatures and pressures¹⁸. This has also been correctly predicted by previous UHF calculations¹⁵. The rhombohedral angle for the AF_{II} spin arrangement of the B1 phase of MnO was calculated here in the pressure range 0 to 90GPa in an attempt to determine if this distortion might be causing the apparent discrepancies in the thermodynamics of the B1 phase up to the phase transition pressure. The calculated rhombohedral angle was found to deviate from the cubic angle of 33.557° by 0.12° at zero pressure, up to 0.67° at ~90GPa. The change in rhombohedral angle with pressure is shown in figure 4.3.

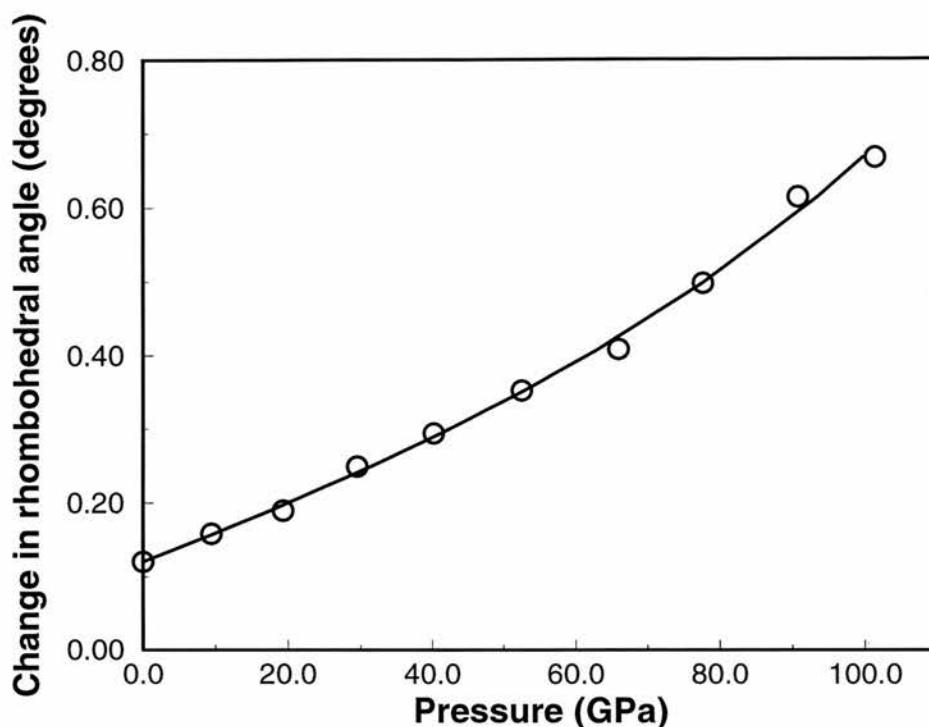


Figure 4.3. Calculated rhombohedral distortion of MnO as a function of (HF) pressure

The Hugoniot plot of this distorted AF_{II} B1 structure is represented by the heavy dashed line in figure 4.1. It follows closely the FM HF Hugoniot curve up to ~60GPa after which a small softening of the lattice is predicted. The rhombohedral distortion resulting from the spin lattice interaction stabilises the B1 phase at these pressures and so cannot account for the experimentally observed phase transition of B1 MnO at 90GPa.

The stability of the AF_{II} spin arrangement with temperature was investigated up to 90GPa from estimates of the Néel temperature (T_N) based on the undistorted B1 structure. The approximation used to represent the Néel temperature was the same as that used in previous UHF studies of MnO and NiO at zero pressure¹⁵, ie, $T_N \propto \Delta E(1+S^{-1})$, where ΔE = the energy difference between the AF_{II} and FM spin arrangements and S = the spin moment. Then, for T_N at some pressure, p , $T_N(p) = T_N(0) \Delta E(p) / \Delta E(0)$. Figure 4.4 shows a plot of the Néel temperature as a function of pressure. It increases almost linearly from ~114K at zero pressure up to ~1000K at ~90GPa. Since the undistorted structure was used to calculate the

Néel temperature in this pressure range, this would be a lower bound on the true estimate and therefore UHF calculations predict that the AF_{II} spin arrangement remains up to the observed transition pressure.

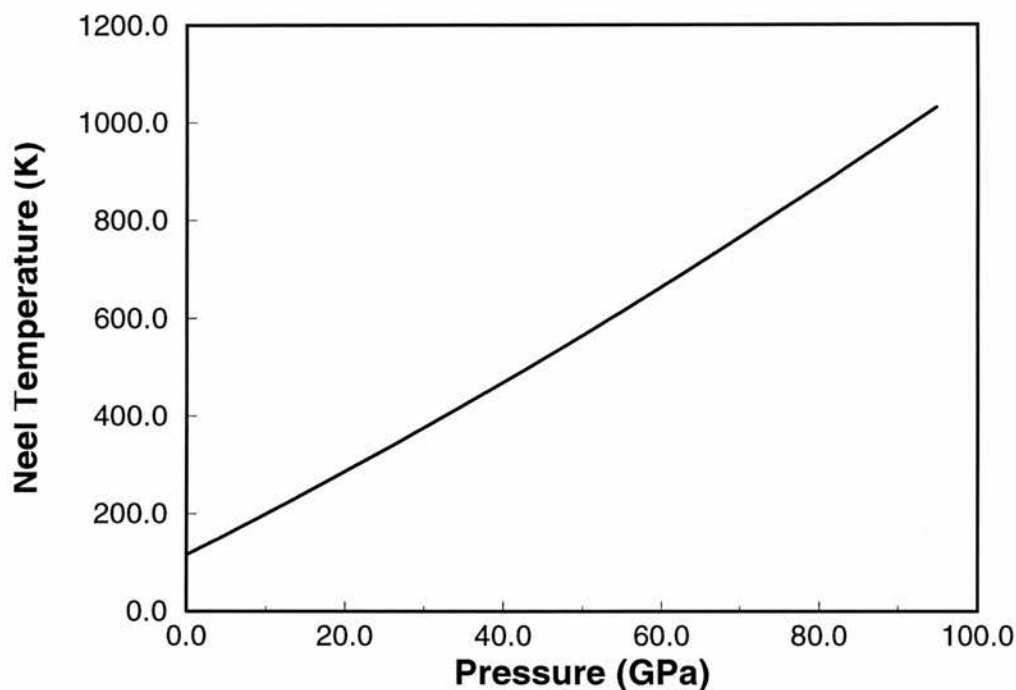


Figure 4.4. Calculated Néel temperature as a function of pressure

The effect of pressure on the electronic structure and DOS of the B1 phase of MnO has been examined. Table 4.3 shows a comparison of the Mulliken charge, 3d population, local spin moment and valence band width of the B1 phase of MnO at zero and 90GPa.

Pressure	q_M	n_{3d}	n_s	U_b
0	1.86	5.11	4.92	8.5
90	1.80	5.19	4.86	12.1

Table 4.3. Comparison of the Mulliken charge, q_M (e), 3d population, n_{3d} , local spin moment, n_s (μ_B) and valence band width, U_b (eV), for Fm3m MnO at 0 GPa and 90 GPa

Very little change is observed in the Mulliken charge and spin distributions on going from 0GPa to 90 GPa with a change of <2% in the d electron populations and spin moments. The calculated valence band width of the FM B1 phase of MnO is found to increase by 3.6eV, from 8.5eV at 0GPa to 12.1eV at 90GPa. This increase is shown graphically in figure 4.5.

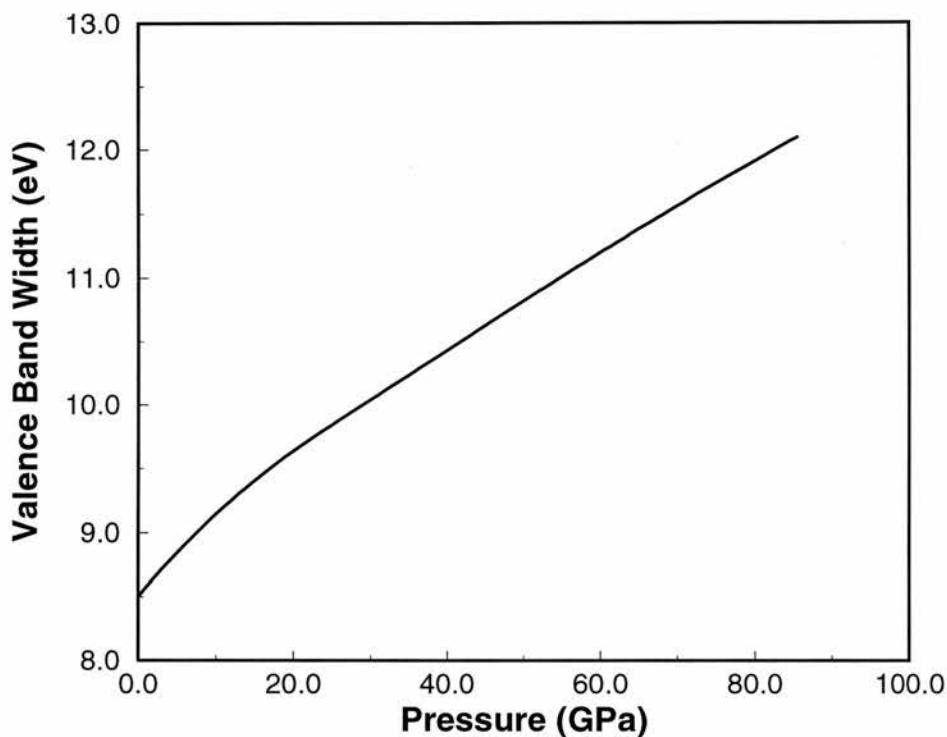


Figure 4.5. Calculated valence band width of FM Fm3m MnO as a function of pressure

The calculated DOS plots of the valence band of the FM B1 phase of MnO at 0GPa and 90GPa are illustrated in figure 4.6, where the Mn(d) and O(p) states are projected out separately. At 90GPa a change occurs in the distribution of states at the upper valence band edge. This suggests that the UHF description of the first ionised state of MnO may be different at high pressures from that described in chapter 3.

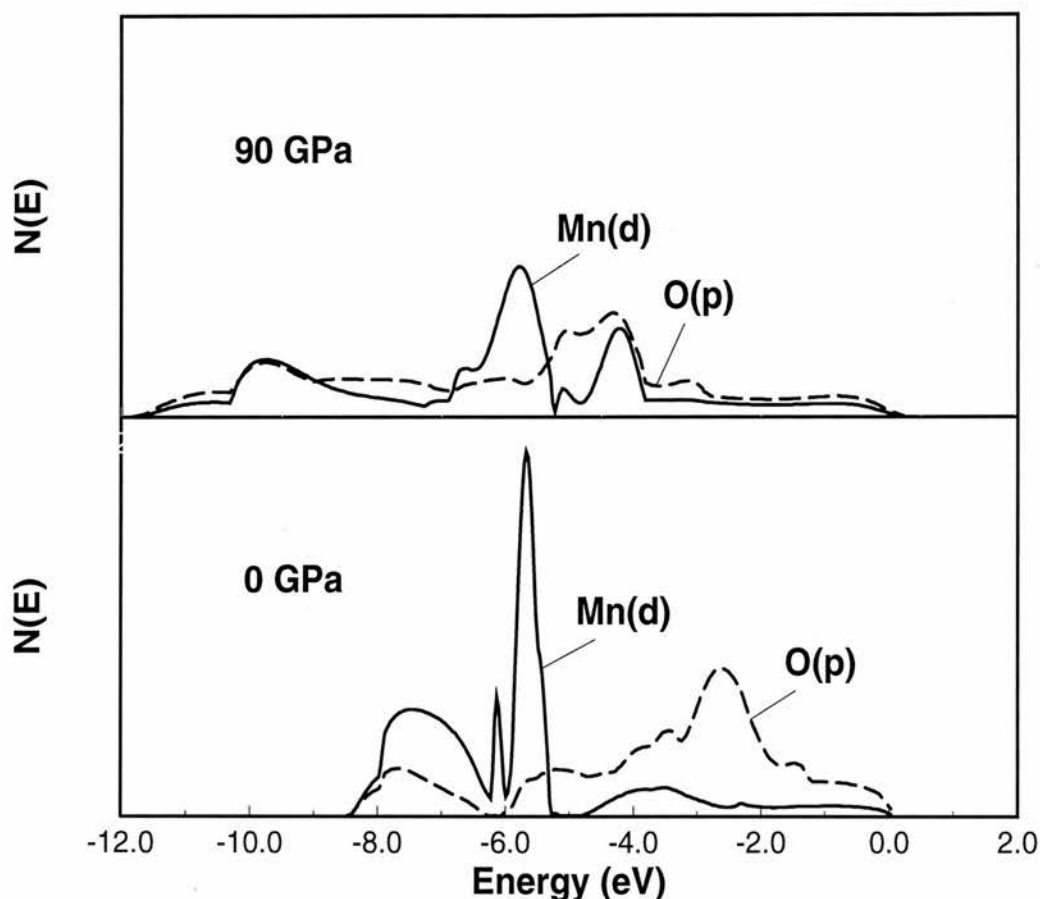


Figure 4.6. Atom projected valence band DOS of FM $Fm\bar{3}m$ MnO at 0 GPa (lower panel) and 90 GPa (upper panel) where the zero of energy has been put at the valence band upper edge

The DOS of the first ionised state was used to estimate the change in the band gap with increasing pressure, shown in figure 4.7. It is found that the band gap increases with pressure up to a maximum value at ~ 45 GPa and no narrowing is observed up to ~ 73 GPa. Changes of this general type have been observed in other systems¹⁹.

For the B2 phase of MnO, there is very little change in the Mulliken charge and spin populations with increasing pressure and no decrease in the band gap up to ~ 118 GPa.

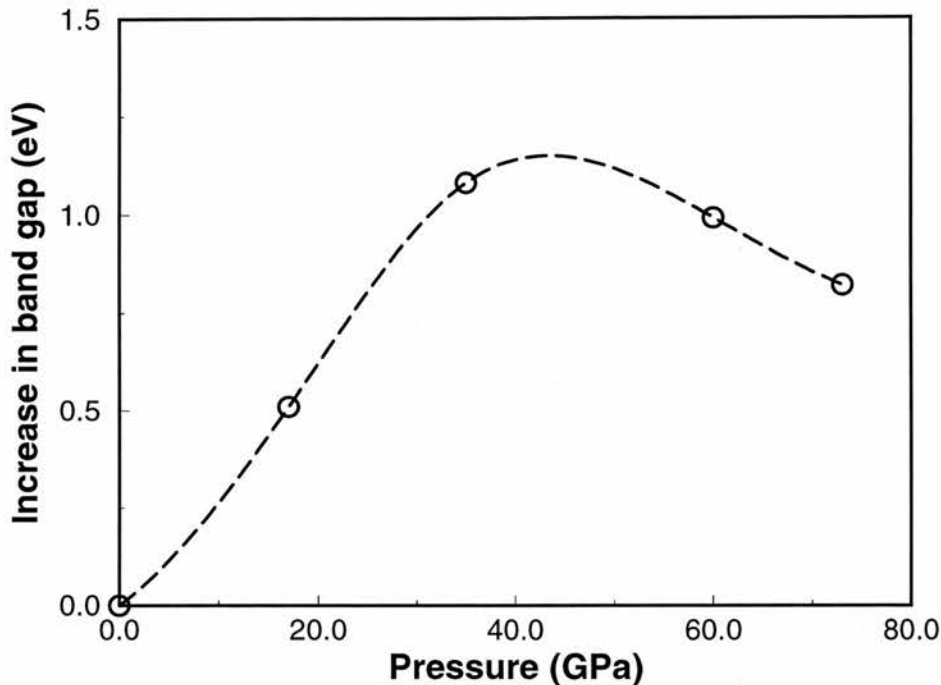


Figure 4.7. Calculated increase in the band gap of FM Fm3m MnO as a function of pressure

4.3. Discussion

Unrestricted Hartree-Fock calculations have been carried out on MnO at high pressures following a recent shock compression study which revealed a phase transition at 90GPa¹. The transition was assumed to follow the trend of the alkaline earth monoxides, ie B1-B2, largely from the magnitude of the transition pressure although no structural investigations were carried out on the high pressure phase.

The B1 phase of MnO was investigated up to a pressure of ~200GPa and is found to be high spin insulating both in the FM and AF_{II} spin arrangements up to this pressure. The calculated Hugoniot of the FM and AF_{II} spin arrangements from figure 4.1 are found to be in good agreement with the experimental static compression data¹³. This suggests that the B1 phase exists at least up to 60GPa after which a slight structural softening takes place up to 90GPa. The data from the shock compression study¹, also shown in figure 4.1, was softer than the static data over the range where the data sets overlapped, between ~40GPa and

~60GPa. However, it was still close enough to the calculated Hugoniot to exclude the possibility of any structural changes up to 90GPa.

From the change in the band gap of the B1 phase of MnO with increasing pressure, the insulating character is found to increase up towards the phase transition pressure. Overall then, UHF calculations predict that the B1 phase of MnO remains unchanged up to the phase transition pressure.

Turning now to the B2 phase of MnO, it is found to be high spin insulating down to a volume of 15.14\AA^3 , which corresponds to HF and HFP pressures of up to ~118GPa and ~93GPa respectively. At these pressures however, the undistorted B1 and spin lattice distorted B1 phases are found to be more stable. Above these pressures, or below the critical volume of 15.14\AA^3 , the B2 phase is found to be conducting. Therefore UHF calculations do not predict the phase transition observed by Noguchi *et al*¹ at 90GPa to be of the type insulating undistorted B1 to insulating undistorted B2. Extrapolation of the B2 phase Gibbs free energy versus pressure plot, shown by the heavy dashed line in figure 4.2, results in an estimate of a hypothetical phase transition pressure between ~149GPa and ~161GPa, which is consistent with the range of phase transition pressures found for the alkali metal monoxides. Figure 4.8 illustrates the experimentally determined transition pressures of the alkali metal monoxides, MnO and FeO as a function of cationic radius. The oxides, SrO, CaO and MgO all undergo typical B1-B2 type phase transitions^{3,2,5}. BaO on the other hand undergoes a transition to a distorted B2 structure at 14GPa⁴, which is represented on the graph by a square. Its phase transition pressure has been increased to 29GPa so that it produces a smooth inflection free curve with the other alkali metal monoxides. If it is assumed that MnO fits on this curve, that is, it undergoes a transition from the insulating undistorted B1 phase to the insulating undistorted B2 phase, an estimate of the phase transition pressure would be ~145GPa. Using the same rational on FeO, the estimated phase transition pressure would be ~200GPa.

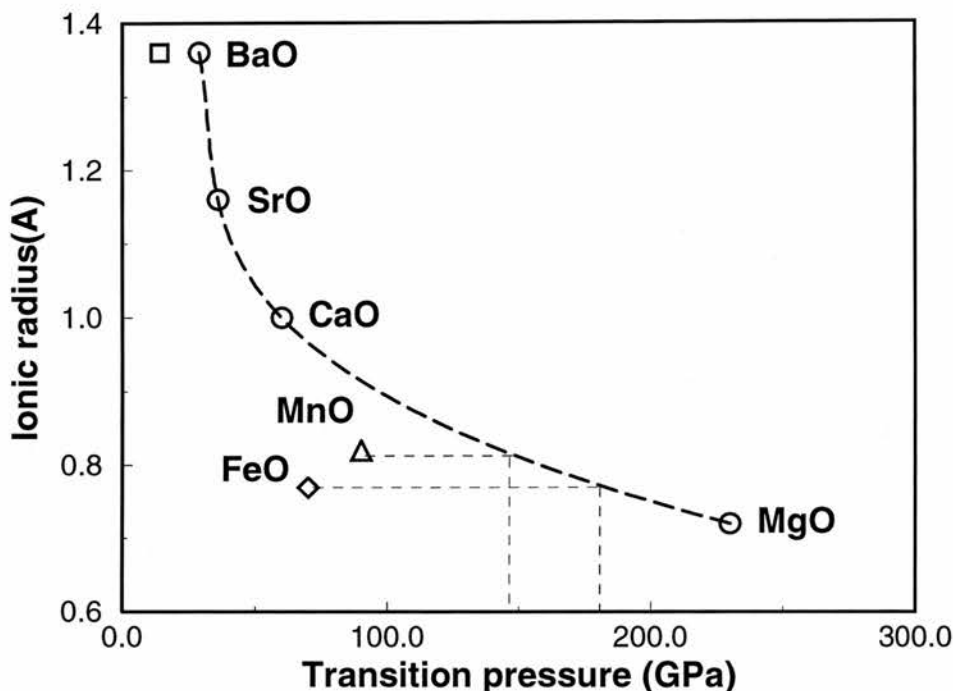


Figure 4.8. Experimental transition pressures of the alkaline earth oxides and FeO and MnO as a function of cation radius

Finally then, from this UHF investigation, there are two possible explanations of the experimentally determined phase transition in MnO at 90GPa observed by Nuguchi *et al*¹. The first is that the transition could be from the B1 phase to a distorted B2 phase as found for BaO⁴. The second is that the phase transition is accompanied by a metallisation to the undistorted or distorted B2 phase. Another less likely explanation is that a metallisation transition takes place resulting in the B8 phase as found in FeO^{8,9,10}. This might be possible as the HF optimised volume of the B8 phase at zero pressure is 1.8% greater than the volume of the B1 phase. Therefore the unit cell volume of a conducting B8 phase could reasonably be less than that of the B1. However a transition to a metallic wurtzite or blende phase would be extremely unlikely as their calculated volumes are ~25% greater than that of the B1 phase at zero pressure.

4.4. Conclusions

The main conclusions from this chapter are: (1) that the B1 phase of MnO remains insulating up to the observed phase transition pressure of 90GPa; (2) that the rhombohedral distortion of AF_{II} B1 MnO increases up to the phase transition pressure; (3) and that the experimentally determined transition at 90GPa is not consistent with an insulating non distorted B1 to B2 phase transition, but could be interpreted in terms of a transition from the B1 phase to a distorted B2 phase or as a transition with metallisation to the B2 phase.

References

1. Y.Noguchi, K.Kusaba, K.Fukuoka, and Y.Syono, *Geophys.Res.Lett.*, 1996, **23**, 1469
2. P.Richet, H-K.Mao and P.M.Bell, *J.Geophys.Res.*, 1988, **93**, 15279
3. Y.Sato, and R.Jeanloz, *J.Geophys.Res.*, 1981, **78**, 8470
4. L.Liu, and W.A.Bassett, *J.Geophys.Res.*, 1972, **77**, 4934
5. T.H.Duffy, R.J.Hemley, and K.H.Mao, *Phys.Rev.Lett.*, 1995, **74**, 1371
6. R.Jeanloz, and T.J.Ahrens, *Geophys.J.R.Astr.Soc.*, 1980, **62**, 505
7. T.Yagi, K.Fukuoka, H.Takei, and Y.Syono, *Geophys.Res.Lett.*, 1988, **15**, 816
8. Y.Fei, and H.K.Mao, *Science*, 1994, **266**, 1678
9. E.Knittle, and R.Jeanloz, *Geophys.Res.Lett.*, 1986, **13**, 1541
10. E.Knittle, R.Jeanloz, A.C.Mitchell, and W.J.Nellis, *Solid State Comm.*, 1986, **59**, 513
11. T.Yagi, T.Suzuki and S.Akimoto, *J.Geophys.Res.*, 1985, **90**, 8784
12. N.Kawai and S.Mochizuki, *Solid State Comm*, 1971, **9**, 1393
13. R.Jeanloz, and A.Ruddy, *J.Geophys.Res.*, 1987, **92**, 11455
14. Y.Syono, T.Goto, J.Nakai, and Y.Nakagawa, 1975, *Proc. 4th Inter.conf. on High Pressure, Kyoto, 1974, Sp.issue of Rev.Phys.Chem.Jpn*, pp 466, Phys- Chem.Soc.Jpn.
15. M.D.Towler, N.L.Allan, N.M.Harrison, V.R.Saunders, W.C.Mackrodt and E.Aprà 1994, *Phys.Rev. B*, **50**, 5041
16. R.I.Hines, N.L.Allan, G.S.Bell, and W.C.Mackrodt, *J.Phys.C: Condensed Matter Physics*, 1997, **9**(34), 7105
17. W.C.Mackrodt, and E-A.Williamson, *J.Phys.C: Condensed Matter Physics*, **9**, 1997, 6951
18. H.Shaked, J.Faber and R.L.Hittermann, *Phys.Rev.B*, 1988, **38**, 11901
19. H.G.Drickamer and C.W.Frank, *Electronic Transitions and the High Pressure Chemistry and Physics of Solids* (Chapman and Hall, London), 1973

Chapter 5

The Valence Charge States In MnO₂ Rutile

5.1. Introduction

The valence state of Mn in MnO₂ is generally thought of as Mn(IV) and for the sake of convenience it is often written as Mn⁴⁺¹. There appears to be some evidence to support this state from electron paramagnetic resonance² (EPR), x-ray absorption³ and electron loss near edge structure (ELNES) spectroscopy⁴ and also some supporting evidence from the Jahn Teller distortion of the reduced Mn(III) state which is interpreted as a product of the high spin d⁴ configuration^{1,5}. However, recent advances in theoretical calculations of the transition metal oxides suggest that this description needs reviewing. From the charge and spin density plots presented in chapter 3, all electron *ab initio* Hartree-Fock calculations have provided direct evidence of the oxygen p hole in the first ionised state of MnO⁶ and Li:MnO⁷. These findings were comparable with previous Hartree-Fock studies of Li:NiO⁸ and NiO⁹.

Since this description of the electron hole in MnO has implications for the higher manganese oxides in general and on the interpretation of experimental data, UHF calculations have been carried out on the ground and first ionised and electron addition states of MnO₂, the purpose of which is to clarify the nature of its valence states. This seems justifiable in light of the commercially exploitable application of MnO₂, in Li solid state batteries^{5,10-13}, where the process of charging is attributed to the reduction of Mn⁴⁺ to give Mn³⁺. An investigation into the valence charge states of Li_xMnO₂ is presented in the next chapter, chapter 6.

5.2. Results

5.2.1 Ground state of MnO₂

Figure 5.1 illustrates MnO₂ in the rutile structure and the atom labelling which will be used throughout this chapter. Two spin states were investigated, the ferromagnetic (FM) arrangement and the antiferromagnetic (AF) arrangement. In terms of figure 5.1, parallel spins on Mn1 and Mn2 give the FM arrangement and

antiparallel spins give the simple AF arrangement. Although the actual low temperature spin state is known to be a complex spiral configuration, which has not been included in this study, investigation of the FM and AF arrangements leads to estimates of the magnetic energies of this system.

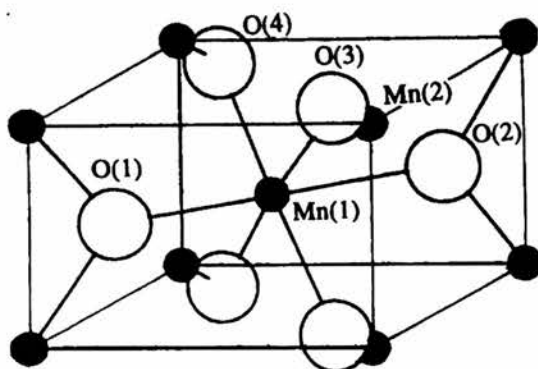


Figure 5.1. Crystal structure of rutile MnO₂ showing the labelling of the atoms in the charged unit cells, Mn₂O₄⁽⁺⁾ and Mn₂O₄⁽⁻⁾

UHF calculations of the FM and AF spin configurations of MnO₂ predict both to be high spin insulators in both the fully symmetric and symmetry broken configurations. The FM arrangement is found to be 0.06eV per MnO₂ unit lower in energy than the AF. In the case of MnO and Fe₂O₃¹⁴, however, the AF arrangement is lower in energy than the FM by 0.006eV. The calculated lattice constants¹⁵, obtained by direct energy minimisation using the FM spin arrangement, are $a = 4.365 \text{ \AA}$, $c = 2.908 \text{ \AA}$ and $u = 0.306$. These compare with experimental values of $a = 4.4041 \text{ \AA}$, $c = 2.7765 \text{ \AA}$ and $u = 0.3046$ ¹⁶ giving a percentage difference between the experimental and calculated values of -0.9%, +1.1% and 0.5% for a , c and u respectively. This corresponds to a difference in energy between the experimental and calculated structures of 0.01eV per MnO₂ unit compared with the total energy of $\sim 1300\text{Ha}$, which testifies to the numerical accuracy of the CRYSTAL program.

Table 5.1 shows the total ($\alpha+\beta$) and net ($\alpha-\beta$) Mulliken populations of the FM and AF spin arrangements which are also invariant to symmetry breaking. From this table the valence state of Mn in both the FM and AF spin arrangements is

seen to be high spin d^5 , with Mulliken 3d populations of ~ 4.7 and total cation charges of $\sim 2.1e$. However for both arrangements the net Mn spin populations are ~ 3.3 which is less than the ionic value of ~ 5 , but close to that associated with Mn(IV).

	FM	AF
$q_M(e)$	2.12	2.14
$n_{3d}(\text{Mn})$	4.70	4.68
$n_s(\text{Mn})$	3.40	± 3.28
$n_s(\text{O})$	-0.20	± 0.06

Table 5.1. Total Mn Mulliken charge, q_M (e), 3d population, n_{3d} , and local spin moments, n_s (μ_B), in the FM and AF states of MnO_2^*

* Total unit-cell energies (Hartree)

FM -2599.020633

AF -2599.016575

The detailed Mn d orbital Mulliken populations are presented in table 5.2 for the FM spin arrangement: the corresponding AF populations, not shown here, are very similar. It is evident from this that the degeneracy of the e_g and t_{2g} orbitals associated with octahedral coordination in MnO_2 is lifted, with differences in both the charge and spin populations.

d-orbital	n	n_s
z^2	0.97	0.75
$x^2 - y^2$	1.08	0.95
xz	0.91	0.60
yz	0.91	0.60
xy	0.83	0.47

Table 5.2. Mulliken charge, n, and spin, n_s , populations in the FM state of MnO_2

Although crystal field effects could be responsible in part for this due to the small deviation from full O_h symmetry, differences in the spin populations suggest that strong overlap effects are also taking place.

To illustrate this, consider the central atom, Mn1, of figure 5.1 and the Mulliken spin and charge populations of its d orbitals shown in table 5.2. The charge and spin populations of the $d_{x^2-y^2}$ orbital, which does not have a nearest neighbour O of the required symmetry for overlap, are almost equal, but the spin population of the d_{xy} orbital, aligned such that overlap occurs with O1 and O2, is approximately half the value of the charge population. This reduced spin population is also observed for the d_{z^2} , d_{xz} and d_{yz} orbitals of Mn1. Therefore the high spin d^5 electron density in MnO_2 is delocalised and partially spin paired due to overlap with the $O p_\sigma$ orbital with spin population of -0.12 compared with -0.04 for the p_π states. This leads to significant d_σ - p_σ covalent bonding in MnO_2 with the valence electron configuration close to d^5 and a local magnetic moment of $\sim 3\mu_B$. The partial covalency of MnO_2 contrasts with the ionic bonding observed in MnO ^{6,17,18}, where the charge and spin populations of Mn are almost identical due to the highly localised distribution of the d^5 electron density.

The atom projected densities of states (DOS) of the FM and AF spin arrangements of MnO_2 , shown in figure 5.2(a), provide more insight into the valence states. The upper panel shows the AF spin arrangement and the lower panel the FM, with the zero of energy fixed at the upper edge of the valence band. In common with other magnetic systems, notably MnO , the AF bands are narrower than the FM bands, due to slightly different orthogonality constraints which lead to a difference of $\sim 2eV$ in the valence band width for example. The band gap, which as expected from previous studies, is grossly overestimated at $\sim 6eV$. It is spanned by filled O(p) states at the valence band edge and predominantly empty Mn(d) states, with a significant O(p) contribution, at the lower conduction band edge. Therefore, UHF calculations predict MnO_2 to be a p-d charge transfer insulator which suggests that the hole state is d^5 and that the electron addition state contains a strong O(p) component.

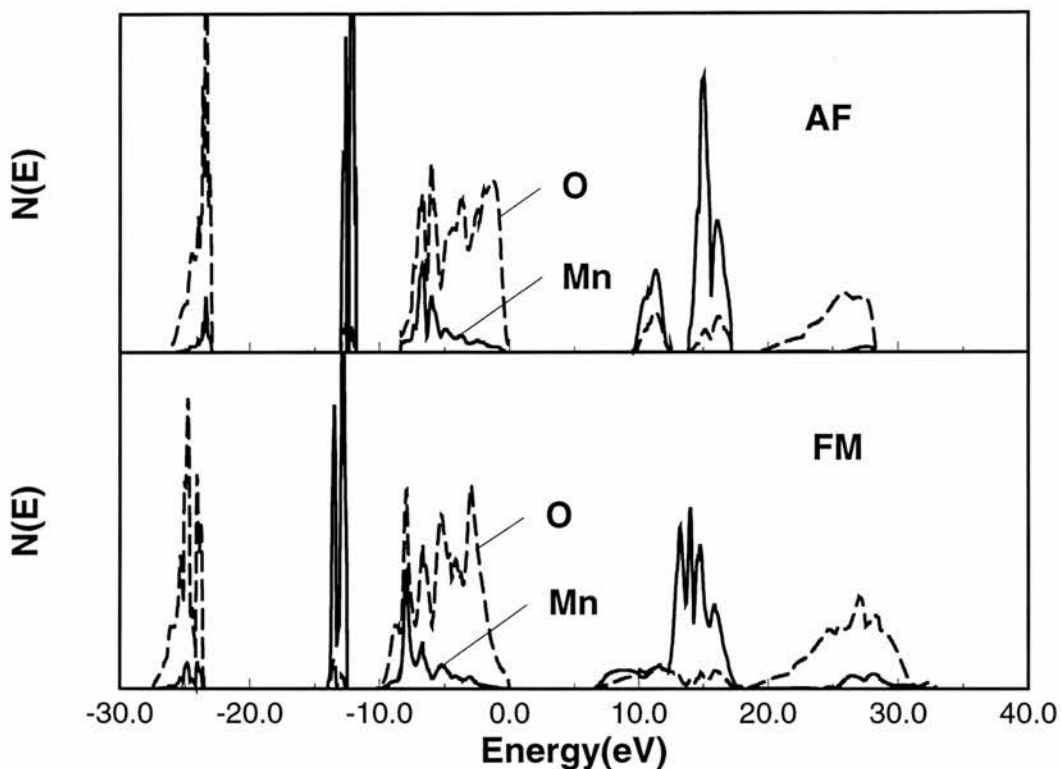


Figure 5.2(a). Atom projected DOS for the AF (upper panel) and FM (lower panel) spin arrangements of MnO_2 (The zero of energy has been put at the upper VBE)

A comparison of the atom projected DOS between MnO (upper panel) and MnO_2 (lower panel) in the FM spin arrangement is illustrated in figure 5.2(b). As in figure 5.2(a) the zero of energy is put at the valence band upper edge, which is similar in both systems, with the majority of states O(p). The main difference between the two systems is in the dispersion of Mn(d) states, shown in the full line in both panels. In the upper panel (MnO) both Mn(d) and O(p) states span the full 8eV of the upper valence band with regions of high Mn(d) density overlapping with regions of low O(p) density and no Mn(d) overlap with O(2s) states. The lower panel shows MnO_2 states, the most striking feature of which is the new band of predominantly Mn(d) states $\sim 5\text{eV}$ below the valence band. The contribution and width of Mn(d) and O(p) states in the valence band differs from MnO , as here high Mn(d) density overlaps with high O(p) density and the bands are broader. The O(2s) band is also broader in MnO_2 than in MnO . Overall then,

figure 5.2(b) suggests that MnO_2 is more covalent than MnO as a result of p-d hybridisation. Furthermore, from figure 5.2(b), it is predicted that the experimental photoemission spectra of MnO and MnO_2 would differ despite their similar d^5 configurations as the majority weight of $\text{Mn}(d)$ states is $\sim 6\text{-}7\text{eV}$ lower in MnO_2 than MnO .

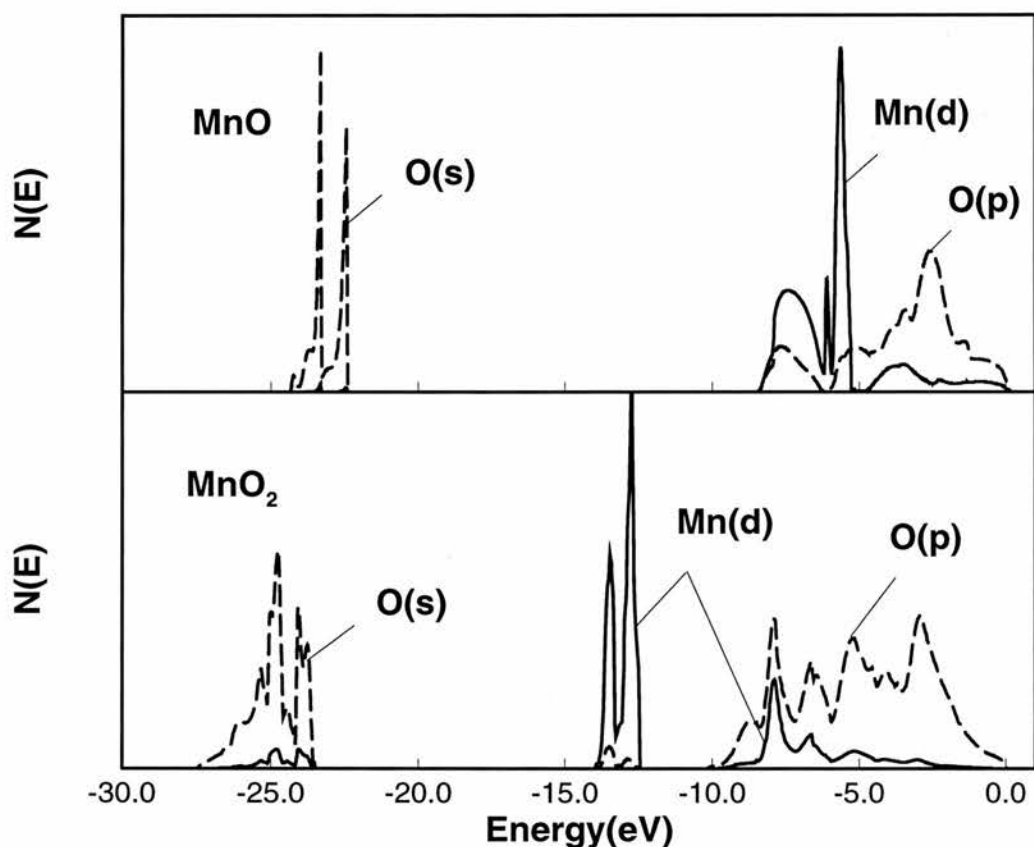


Figure 5.2(b). Comparison of atom projected DOS of MnO (upper panel) and MnO_2 (lower panel) in the FM spin arrangements

5.2.2 First ionised state of MnO_2

As in the case of MnO , broken symmetry calculations were used to localise the hole state in MnO_2 , where one Mn atom was displaced slightly from its normal lattice position. For example, Mn1 of figure 5.1 was displaced by 0.001\AA towards O2. Due to the limits of the available computational resources, calculations were confined to two molecular units, the labelling of which is illustrated for the MnO_2 rutile structure, shown in figure 5.1.

UHF calculations on the FM and AF spin arrangements of the first ionised state of MnO_2 give high spin insulating solutions with the AF configuration now lower in energy by 0.04eV per MnO_2 . It is found from Mulliken charge population analyses that $\sim 90\%$ of the hole is localised at the O1-Mn1-O2 unit (see figure 5.1 for labelling) with $\sim 60\%$ at O1 , $\sim 20\%$ at O2 and $\sim 10\%$ at Mn1 . Table 5.3 shows the changes in the Mulliken population for both spin arrangements of the first ionised state of MnO_2 (Mn_2O_4^+) compared with the neutral ground state. Mn1 undergoes little change, <0.1 , in its 3d Mulliken population, with negligible change in Mn2 for both spin arrangements. There is a slight increase in spin population on Mn2 , from 0.1 to 0.2 , but negligible change on Mn1 for both spin arrangements. Therefore, the Mulliken analysis agrees with the DOS prediction for the first ionised state of MnO_2 in that 80% of the hole is localised at oxygen sites with very little change to the Mn sublattice.

	FM	AF
$\delta q_{\text{M}}(\text{Mn}_1)$	+0.10	+0.09
$\delta n_{3d}(\text{Mn}_1)$	-0.08	-0.09
$\delta n_{\text{s}}(\text{Mn}_1)$	+0.04	-0.09
$\delta q_{\text{M}}(\text{Mn}_2)$	+0.04	+0.02
$\delta n_{3d}(\text{Mn}_2)$	0.0	-0.01
$\delta n_{\text{s}}(\text{Mn}_2)$	+0.10	+0.23
$\delta q_{\text{M}}(\text{O}_1)$	-0.57	-0.59
$\delta q_{\text{M}}(\text{O}_2)$	-0.23	-0.19
$\delta q_{\text{M}}(\text{O}_3)$	-0.04	-0.04
$\delta q_{\text{M}}(\text{O}_4)$	-0.04	-0.04

Table 5.3. Differences in the total Mulliken charges, δq_{M} , 3d populations, δn_{3d} , and net spin populations, δn_{s} , between the FM and AF states of Mn_2O_4 and $\text{Mn}_2\text{O}_4^{(+)}$.

Figures 5.3(a) and 5.3(b) illustrate the integrated differences in charge density between neutral Mn_2O_4 and the first ionised state, Mn_2O_4^+ , projected onto a $\{001\}$ basal plane, with O1-Mn1-O2 shown in figure 5.3(a) and O3-Mn2-O4 shown in 5.3(b). From these it is clear to see that the majority of charge density difference is at the O1 site with the rest at O2 and little at O3 and O4 as predicted by the Mulliken charge population analysis shown in table 5.3.

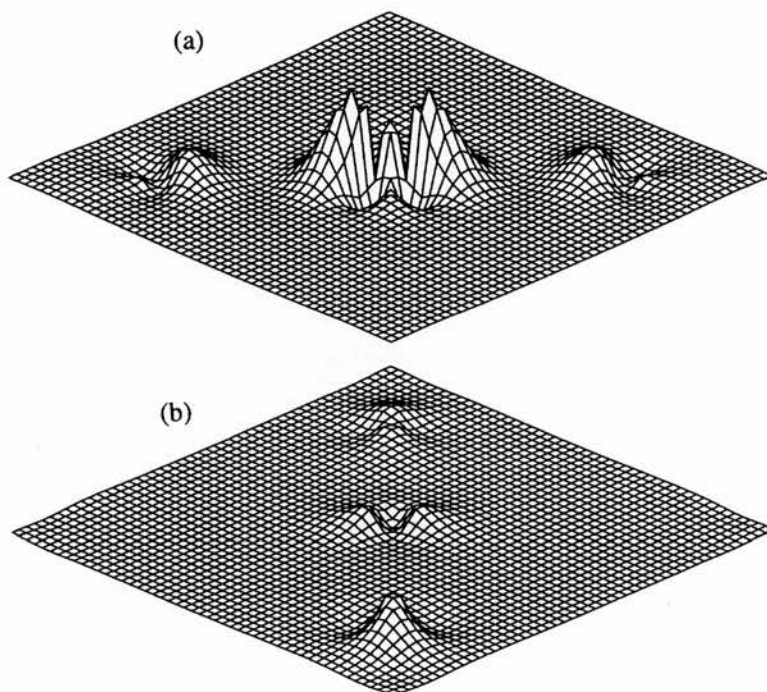


Figure 5.3. Integrated difference in the charge density between Mn_2O_4 and $\text{Mn}_2\text{O}_4^{(+)}$ projected onto the $\{001\}$ plane for the O(1)Mn(1)O(2) atoms (a) and O(3)Mn(2)O(4) atoms (b) of the unit cell. (Labelling corresponds to Figure 5.1)

5.2.3 First electron addition state of MnO_2

Broken symmetry calculations were used again, this time to self trap the added electron. The displacement required, however, was $\sim 0.13\text{\AA}$ which results in high spin insulating states for both spin arrangements with the FM configuration lower in energy by 0.03eV .

The changes in the Mulliken charge and spin populations between the neutral system, Mn_2O_4 , and the first electron addition state, Mn_2O_4^- , are shown in table 5.4.

	FM	AF
$\delta q_M(\text{Mn}_1)$	-0.13	-0.18
$\delta n_{3d}(\text{Mn}_1)$	+0.12	+0.23
$\delta n_s(\text{Mn}_1)$	+0.04	+0.56
$\delta q_M(\text{Mn}_2)$	-0.12	-0.12
$\delta n_{3d}(\text{Mn}_2)$	+0.16	+0.12
$\delta n_s(\text{Mn}_2)$	+0.28	0.0
$\delta q_M(\text{O}_1)$	-0.27	-0.14
$\delta q_M(\text{O}_2)$	-0.20	-0.12
$\delta q_M(\text{O}_3)$	-0.14	-0.22
$\delta q_M(\text{O}_4)$	-0.14	-0.22

Table 5.4. Differences in the total Mulliken charges, δq_M , 3d populations, δn_{3d} , and net spin populations, δn_s , between the FM and AF states of Mn_2O_4 and $\text{Mn}_2\text{O}_4^{(-)}$.

The distribution of charge from the added electron is similar for both spin arrangements, with more or less equal distribution between the two MnO_2 units of the lattice. Approximately 70% of the additional charge is localised at the four oxygen sites and ~30% at the two manganese sites of the unit cell. The Mulliken charge of Mn1 in the FM Mn_2O_4^- system remains close to that in the neutral system with an increase in charge population of only 0.12 and a slight increase in spin population of ~0.04. However, Mn2 of the same system shows an increase in charge population of ~0.16 and an increase in spin population of ~0.3 which results in a local moment of $\sim 3.9\mu_B$. For the AF spin arrangement of Mn_2O_4^- , the opposite occurs as very little change in Mulliken charge and spin population is found at Mn2, only 0.12, and zero respectively.

From the Mulliken charge and spin analysis, the majority of additional charge, ~70%, localises at oxygen sites which leaves the manganese close to a d^5 configuration. The local moment at one Mn site increases to $\sim 4\mu_B$ due to the redistribution of unpaired spin, which is associated with the formal Mn(III) state. Figures 5.4(a) and 5.4(b) show the integrated difference in charge density between $Mn_2O_4^-$ and Mn_2O_4 projected onto a {001} basal plane. The O1-Mn1-O2 unit is illustrated in figure 5.4(a) and the increase in charge on the two oxygen atoms is clearly visible with substantial reorganisation of charge at the central Mn1 site. Figure 5.4(b) illustrates the same integrated charge density difference for the O3-Mn2-O4 unit. Again the increase in charge is apparent at the two outer oxygen positions but the decrease in charge at the Mn2 site is masked due to a reorganisation of charge from the d_{xy} and d_{yz} to the d_{z^2} and d_{xz} orbitals. Overall, however, these integrated difference density plots are entirely consistent with the Mulliken populations.

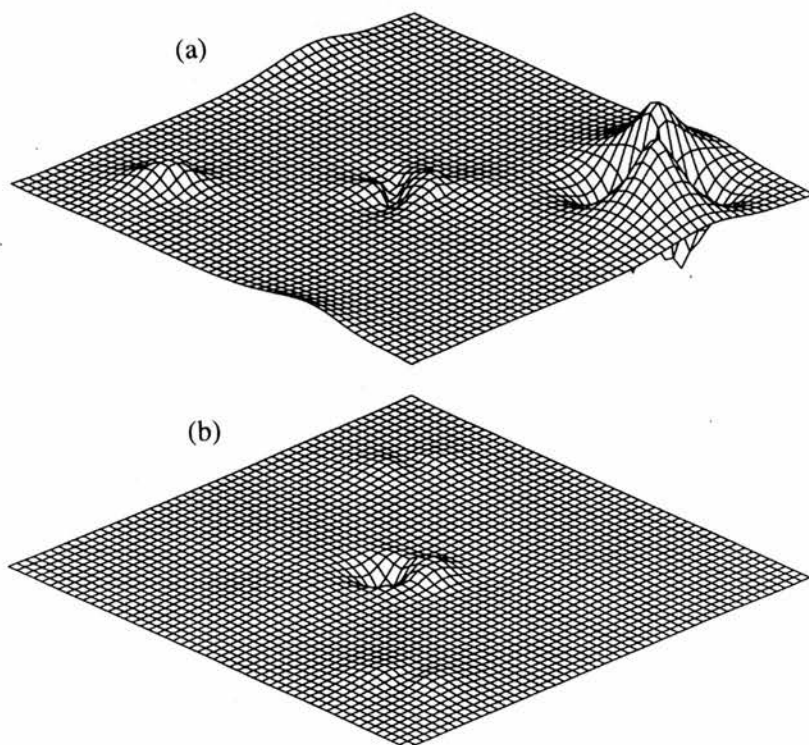


Figure 5.4. Integrated difference in the charge density between $Mn_2O_4^{(-)}$ and Mn_2O_4 projected onto the {001} plane for the O(1)Mn(1)O(2) atoms (a) and O(3)Mn(2)O(4) atoms (b) of the unit cell. (Labelling corresponds to Figure 5.1)

5.3. Discussion

Unrestricted Hartree-Fock calculations have been carried out on the neutral, first ionised and first electron addition states of MnO_2 in the ferromagnetic and antiferromagnetic spin arrangements in order to determine the nature of the valence states. The results are most readily interpreted in terms of the changes in the Mulliken charge and spin populations from the neutral system, the atom projected densities of states and the integrated differences in charge density from the neutral system to the first ionised and first electron addition states.

The lattice constants of ground state MnO_2 were calculated by direct energy minimisation and found to be within 1% of the experimental values. This corresponds to a difference in energy of $3 \times 10^{-5}\%$ between the experimental and calculated structures, which illustrates the high numerical accuracy of the calculations and also the overall stability of the CRYSTAL code. It is predicted, from the 133.6° Mn-O-Mn angle in MnO_2 , that no significant superexchange interaction is taking place which is supported by the lower energy FM state.

The main conclusion from the neutral ground state calculations is that Mn is present in a d^5 state with a local spin moment of $\sim 3\mu_B$, both in the FM and AF spin configurations. This suggests that MnO_2 is a partially covalent system.

The atom projected DOS of neutral MnO_2 suggests that it is a charge transfer insulator like MnO, with the valence band upper edge dominated by O(p) states. However the DOS of MnO_2 differs from that of MnO with the majority of Mn(d) states $\sim 6-7\text{eV}$ lower in energy even although Mn is in a d^5 state. This lowering in energy of the Mn(d) states is a result of the reduced Madelung potential in MnO_2 compared with MnO, as a consequence of the reduced oxygen charge. The differences in the DOS between MnO and MnO_2 are supported by previous x-ray photoelectron⁴ and ultraviolet photoelectron spectroscopy¹⁹ studies of these oxides, where the shift to lower energy is cited as characteristic of the difference between Mn(II) and Mn(IV). The conventional explanation for this shift is the enhanced Coulomb potential of Mn^{4+} compared with Mn^{3+} , whereas here, it is attributed to the reduced Coulomb potential of O^- compared with O^{2-} . Figure 5.5 shows a comparison of the upper valence band DOS of MnO, orthorhombic ($Pnmm$) LiMnO_2 ²⁰ and MnO_2 , all of which have been calculated as $\sim d^5$

configurations, and represent Mn(II), Mn(III) and Mn(IV) respectively. The shift in Mn(d) states from MnO to MnO₂ is almost linear from ~7eV below the valence band edge in MnO to ~13eV below for MnO₂ despite the constant approximate 3d⁵ Mulliken population. In the case of LiMnO₂⁷ the Mulliken 3d charge population and local spin moment are calculated to be 4.84 and 3.97, which are very close to those found for the electron addition state which is also formally Mn(III). A more detailed analysis of the Li_xMnO₂ investigation is presented in chapter 6.

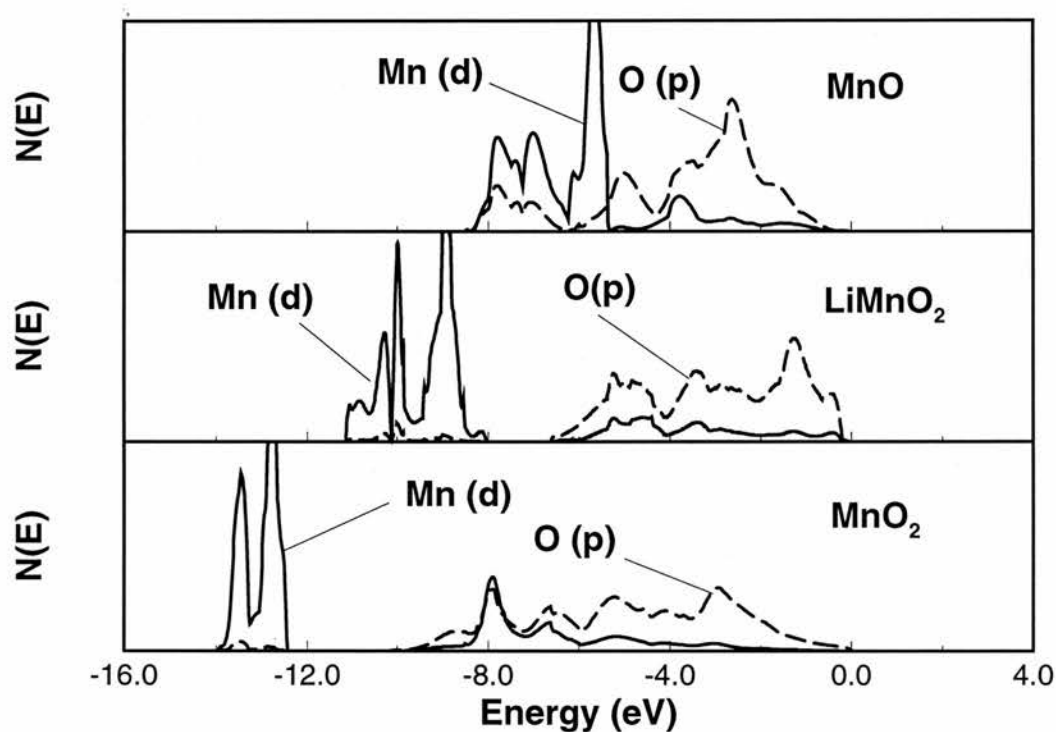


Figure 5.5. Comparison of the valence band DOS of MnO, LiMnO₂ and MnO₂

From the valence band DOS of neutral MnO₂ it is predicted from the rigid band approximation that the first ionised state is essentially O(p). This is confirmed by the Mulliken population analyses which show that ~90% of the hole density is localised at the oxygen sites with the Mn 3d population remaining close to a d⁵ configuration and a local moment which remains largely unchanged. This is

supported by the charge density difference plots which were as always calculated directly from the wavefunction.

Previous UHF calculations on the first ionised state of MnO^6 , which formally can be thought of as Mn(III) predict self trapped holes. Since the first electron addition state of MnO_2 can also be thought of formally as Mn(III) a reasonable assumption is that this addition state would also be O(p) in nature. This is found to be the case from the Mulliken population analysis of Mn_2O_4^- where ~80% of the additional charge is localised at the oxygen positions with the most significant change to Mn being the addition of ~0.3 spin population which increased the local moment to $\sim 3.8\mu_B$. This is close to the formal value of $4\mu_B$ for Mn(III). The increased local moment indicates the localisation of unpaired spin density and hence a shift towards greater ionicity. The charge density difference plots of Mn_2O_4^- are again consistent with the Mulliken populations.

In summary, UHF calculations predict that the Mn d^5 state in MnO_2 is very stable and remains even on electron addition or removal. This is shown from the changes in Mulliken populations and supported by the integrated differences in charge densities between the neutral and charged systems which were obtained directly from the wavefunction.

5.4. Conclusions

The main conclusions of this chapter are: (1) that the valence state of Mn in MnO_2 is a d^5 configuration with a local moment of $\sim 3\mu_B$ which suggests that it is substantially covalent; (2) that the valence state of Mn does not depend on the spin state of the system; (3) that the hole states in MnO_2 are oxygen p states as found previously for MnO; (4) that the electron addition state of MnO_2 is also an oxygen p state but with the local moment on the Mn nearest neighbour $\sim 4\mu_B$; (5) and that the lattice distortion which results from a one electron addition to MnO_2 is not associated with the $3d^4$ state.

References

1. P.A.Cox, ' *Transition Metal Oxides* ', Oxford University Press 1990
2. M.V.Ananth and K.Dakshinamurthi, *J.Power Sources*, 1992, **40**, 355
3. S.I.Salem, C.N.Chang, P.L.Lee and V.Severson, *J.Phys. C: Solid State Phys.*,1978, **11**, 4085
4. J.H.Paterson and O.L.Krivanek, *Ultramicroscopy*, 1990, **32**, 319
5. A.R.Armstrong and P.G.Bruce, *Nature*, 1996, **381**, 499
6. W.C.Mackrodt and E-A.Williamson, *J.Phys.C: Condensed Matter Physics*, 1997, **9**, 1-16
7. W.C.Mackrodt and E-A.Williamson, *Ber.Bunsenges.Phys.Chem.*, 1997 - in press
8. W.C.Mackrodt, N.M.Harrison, V.R.Saunders, N.L.Allan and M.D.Towler, *Chem.Phys.Lett.*, 1996, **250** 66
9. W.C.Mackrodt, *Ber.Bunsenges.Phys.Chem.*, 1997, **101**, 169
10. M.M.Thackeray, W.I.F.David, P.G.Bruce and J.B.Goodenough, *Mater.Res.Bull.*, 1983, **18**, 461
11. J.M.Tarascon and D.Guyomard, *Electrochimica Acta*, 1993, **38**, 1221
12. G.Pistola and G.Wang, *Solid State Ionics*, 1993, **66**, 135
13. H.Huang and P.G.Bruce, *J.Power Sources*, 1995, **54**, 52
14. W.C.Mackrodt and M.Gautier-Soyer, (1997) - To be submitted
15. W.C.Mackrodt and E-A.Williamson, *Journal of the Chemical Society, Faraday Transactions*. 1997, **93**(18), 3295
16. R.W.Wyckoff, *Crystal Structures*, Vol 1 (Interscience, New York 1960)
17. W.C.Mackrodt, N.M.Harrison, V.R.Saunders, N.L.Allan, M.D.Towler, E.Aprà and R.Dovesi, *Phil.Mag. A*, 1993, **68**, 653
18. M.D.Towler, N.L.Allan, N.M.Harrison, V.R.Saunders, W.C.Mackrodt, and E.Aprà, *Phys.Rev. B*, 1994, **50**, 5041
19. J.Zaanen, G.A.Sawatzky, and J.W.Allen, *Phys.Rev.Lett.*, 1984, **55**, 418
20. R.Hoppe, G.Brachtel and M.Jansen, *Zeit.f.Anorgan.Alleg.Chemie*, 1975, **417**, 1

Chapter 6

The Electronic Structure Of Monoclinic C2/m Li_xMnO_2

$$(1 \geq x \geq 0)$$

6.1. Introduction

After the launch of the first commercially successful rechargeable Li battery¹ in 1990, the search began for new, less expensive and less toxic electrode materials which could intercalate Li into their lattice structure. The newly synthesised C2/m monoclinic LiMnO_2 ² phase by Armstrong and Bruce is one such material. It is described in terms of a distorted rhombohedral structure due to the strong Jahn Teller nature of Mn^{3+} attributed to the high spin $3d^4$ configuration. During battery operation the valence of Mn is assumed to vary between Mn^{3+} and Mn^{4+} , controlled by the movement of Li out of and into the lattice structure, thus Li_xMnO_2 ($0.5 \leq x \leq 0.95$).

Other manganese oxides have been investigated for the same reason, especially orthorhombic LiMnO_2 ³ which has been used as a precursor to synthesise the electrode material, defective LiMn_2O_4 spinel. However, very little work has been carried out to determine the basic physical properties of these systems. In fact although the crystal structure of orthorhombic Pmmn LiMnO_2 has been known since 1975, the first detailed study of its magnetic properties⁴ has only just been published this year.

Chapters 3 and 4 presented the results of UHF calculations which were carried out on MnO^5 , MnO_2 ⁶ and their defect states^{5,6,7}. These calculations predicted the valence electron configurations of the formal Mn(II), Mn(III) and Mn(IV) states as d^5 but with local magnetic moments of $\sim 5\mu_B$, $\sim 4\mu_B$ and $\sim 3\mu_B$ respectively. Furthermore, the Jahn Teller distortion associated with the formal Mn(III) state, which in the past has always been attributed to the high spin $3d^4$ valence electron configuration, could instead be attributed to the O p^5 configuration. Since the formal valence of Mn in LiMnO_2 is Mn(III) it would be interesting to investigate this material to confirm whether the previous description of the Mn(III) valence electron configuration could be applied here. In view of the important role that

the electronic valence state plays in monoclinic LiMnO_2 during battery operation, it also seems justifiable to investigate its fundamental electronic properties. Since a recent FLAPW⁸ investigation carried out on monoclinic LiMnO_2 failed to address these issues, UHF calculations have been carried out on C2/m monoclinic Li_xMnO_2 in the range $1 \geq x \geq 0$.

6.2. Results

6.2.1 LiMnO_2

Supercells of the C2/m monoclinic LiMnO_2 structure, type 1(P,P)⁹, were constructed in the composition range $\text{Li}_n\text{Mn}_4\text{O}_8$ (where $n = 0, 1, 2, 3, 4$). The fully lithiated lattice structure is shown in figure 6.1.

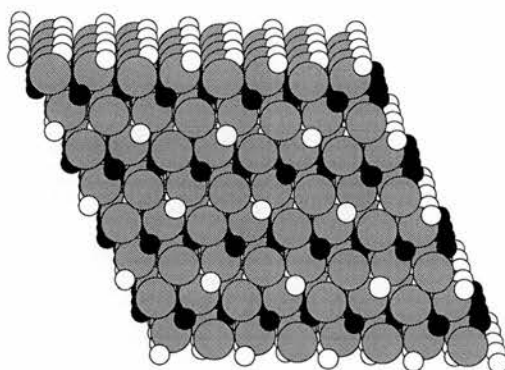


Figure 6.1. Crystal structure of C2/m LiMnO_2^2 where the small white spheres represent Mn, the small black spheres Li and the large grey spheres O

Various spin arrangements of $\text{Li}_4\text{Mn}_4\text{O}_8$ were investigated, which included the ferromagnetic (FM) and three antiferromagnetic (AF_1 , AF_2 , AF_3) spin configurations. The AF_1 structure contains ferromagnetic layers of Mn stacked antiferromagnetically and the AF_2 and AF_3 structures contain FM chains arranged antiferromagnetically in Mn layers. UHF calculations predict the order of stability of these magnetic states to be, $\text{AF}_3 < \text{FM} < \text{AF}_1 < \text{AF}_2$ and all were found to be high spin wide band gap insulators. The difference in energy between AF_3 and FM, ΔE , is 0.02eV which is more than double the value found MnO^{10} (0.006eV) and less than half the value found for MnO_2^6 (0.06eV). Table 6.1

shows the total ($\uparrow + \downarrow$) and net ($\uparrow - \downarrow$) spin populations for the AF₃ and FM spin arrangements in Li₄Mn₄O₈. The Mulliken 3d population for both spin arrangements is ~ 4.9 with a local spin moment of $\sim 4\mu_B$ which is localised on Mn with only $\sim 0.03\mu_B$ at the O sites. The Mulliken charges are $\sim 1.0e$, $\sim 2.0e$ and $\sim 1.5e$ for Li, Mn and O respectively.

	AF ₃	FM
$q_M(e)$	2.03	2.03
$n_{3d}(Mn)$	4.86	4.85
$n_s(Mn)$	± 3.97	3.95
$n_s(O)$	± 0.03	0.03

Table 6.1. Total Mn Mulliken charge, q_M (e), 3d population, n_{3d} , and local spin moments, n_s (μ_B), in the AF₃ and FM arrangements of C2/m LiMnO₂

The other AF states, AF₁ and AF₂, although not shown in table 6.1, are nearly identical to the AF₃ state with $<1\%$ differences in the individual Mulliken populations. Table 6.2 shows a more detailed Mulliken analysis of the AF₃ spin configuration, which illustrates the differences in the spin and charge populations of the Mn d orbitals.

d-orbital	n	n_s
z^2	1.06	0.96
$x^2 - y^2$	1.09	0.94
xz	0.71	0.37
yz	1.09	0.94
xy	0.92	0.74

Table 6.2. Mulliken charge, n, and spin, n_s , populations in the AF₃ arrangement of C2/m LiMnO₂

These differences are partially attributed to the distorted MnO_6 octahedron which removed the degeneracies of the Mn d orbitals resulting in unequal Mulliken charge and spin occupancies. Although it is possible that crystal field effects could be solely responsible for the unequal spin populations it seems more likely that overlap effects are also operational as found previously in MnO_2 ⁶. With reference to the MnO_6 octahedron in figure 6.2, the d_{xz} orbital has the appropriate symmetry to overlap with two oxygen atoms, one above and one below the Mn plane which would result in partial covalency and a reduction in the net spin.

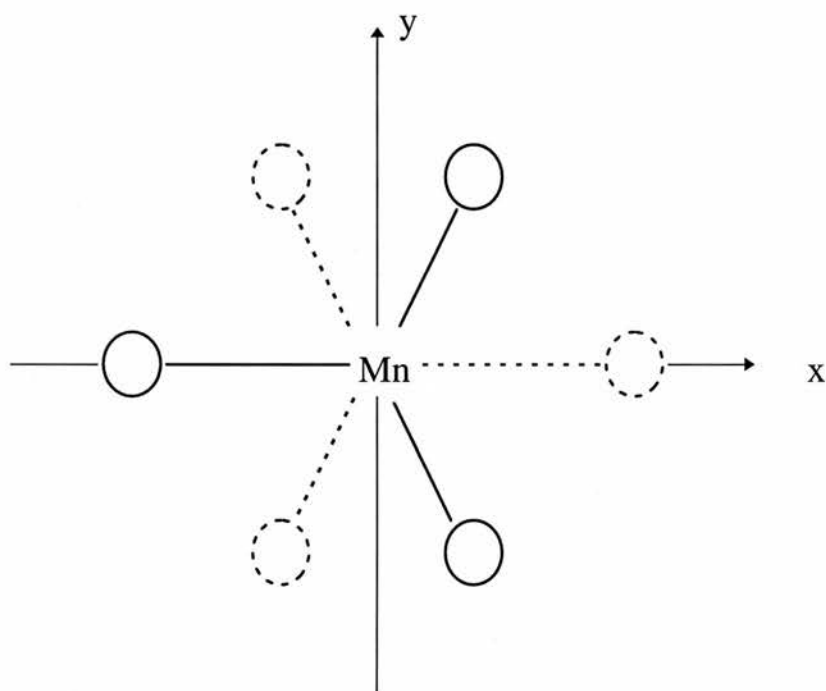


Figure 6.2. Coordinate system of the layer structure of the MnO_6 octahedra in $C2/m$ LiMnO_2 , where the full and broken circles represent the O layers above and below the Mn layer respectively.

For comparison with the $C2/m$ monoclinic LiMnO_2 ² structure, UHF calculations were also carried out on another FM phase of LiMnO_2 , the orthorhombic $Pmmn$ structure reported by Hoppe, Brachtel and Jansen³. It is found to be 0.03eV lower in energy than FM $C2/m$ structure but with very similar Mulliken populations as

shown in table 6.3. On the addition of correlation corrections, this energy difference is reduced from 0.03eV to 0.02eV.

Phase	$\Delta E_L(\text{HF})$	$\Delta E_L(\text{HFP})$	q_M	n_{3d}	n_s
C2/m	0.0	0.0	2.03	4.85	3.95
Pmmn	- 0.03	- 0.02	2.05	4.84	3.97

Table 6.3. Relative energies, ΔE_L (eV), Mn Mulliken charge, q_M (e), 3d population, n_{3d} , and local Mn spin moment, n_s (μ_B), of FM (C2/m) and (Pmmn) LiMnO_2 (Here and in subsequent tables HF and HFP refer to UHF energies without and with *a posteriori* correlation corrections based on the Perdew functional)

The energy differences and spin moments of Mn for the FLAPW and UHF calculated spin arrangements of the C2/m monoclinic LiMnO_2 structure are compared in table 6.4. In both cases the magnetic ground state is predicted to be AF_3 but there is a striking difference in the Mn spin moments, as the FLAPW calculations predicted a spin moment $\sim 17\%$ ($0.7\mu_B$) less than the UHF value of $3.97\mu_B$. Also the FLAPW calculations predicted a much greater variation in Mn spin moment from AF_3 to FM spin arrangements, $3.29\mu_B$ to $3.45\mu_B$ respectively.

Phase	ΔE			μ	
	HF	HFP	FLAPW	UHF	FLAPW
FM	0.0	0.0	0.0	3.95	3.45
AF_1	+ 0.004	-	- 0.003	3.95	-
AF_2	+ 0.014	-	- 0.092	3.98	3.34
AF_3	- 0.021	- 0.020	- 0.173	3.97	3.29

Table 6.4. Relative energies, ΔE (eV/formula unit), and local Mn spin moments, μ (μ_B), of the AF_1 , AF_2 and AF_3 phases of (C2/m) LiMnO_2 compared with FLAPW values⁸

The valence and conduction band atom projected DOS of AF₃ and FM LiMnO₂ are illustrated in figure 6.3. As before the AF₃ plot shows a narrowing of the bands compared with the FM spin arrangement due to different orthogonality constraints on the two wavefunctions. In both cases, the upper valence band of ~6-7eV, is constructed from predominantly O(p) states but with a significant Mn(d) density throughout. A narrower Mn(d) band exists ~2-3eV below the lower edge of the valence band. The gap between the valence and conduction band is spanned by mostly O(p) states at the valence band edge (VBE) and Mn(d) states at the conduction band edge (CBE), but with a significant O(p) contribution. Therefore, UHF calculations predict LiMnO₂ to be a p-d charge transfer insulator and, within a rigid band approximation, to remain ~d⁵ in the initial stages of oxidation or, specifically in this case, Li removal.

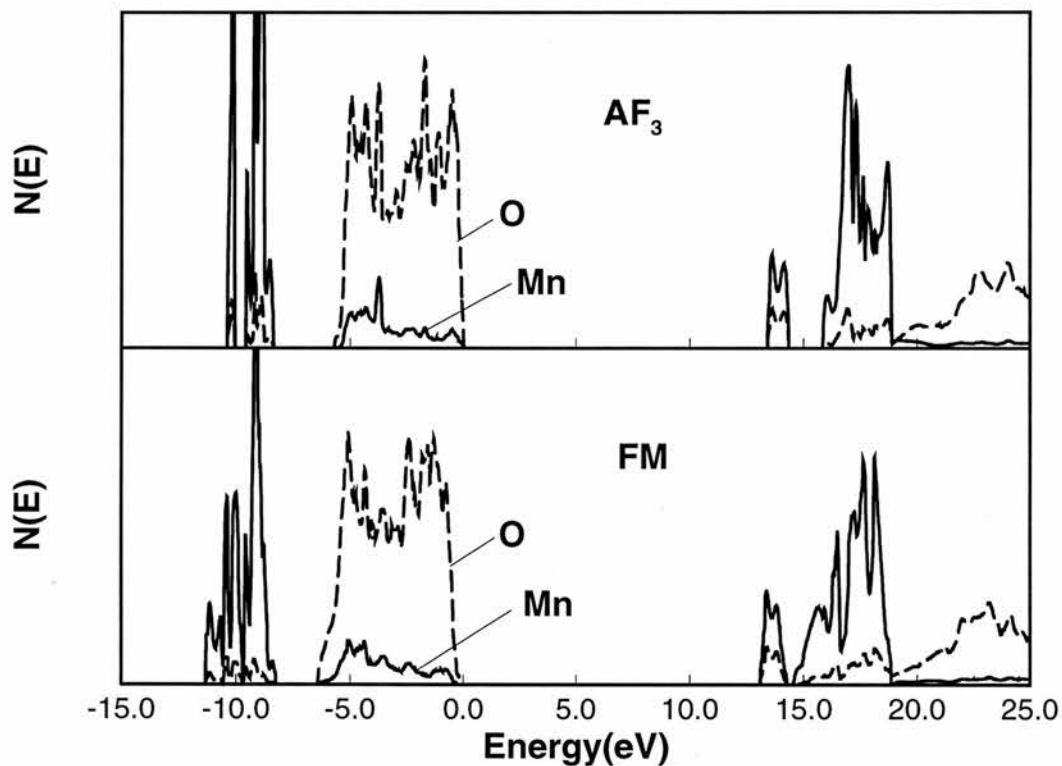
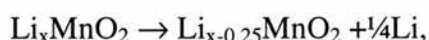


Figure 6.3. Atom projected valence and conduction band DOS for the AF₃ (upper panel) and FM (lower panel) spin arrangements (the zero of energy has been put at the VBE)

6.2.2 Li_xMnO_2 ($x < 1$)

The FM arrangement was the only one considered here as the difference in energy between the AF_3 and FM phases of $\text{Li}_{0.75}\text{MnO}_2$ (0.00035eV) is so small that, at this Li concentration and below, the monoclinic C2/m structure would not exhibit any AF_3 order.

Table 6.5 shows the Li removal energy, U_r , and the Mulliken charge and spin populations of Mn and O for the unrelaxed monoclinic C2/m Li_xMnO_2 structure with $x = 0.0, 0.25, 0.5, 0.75, 1.0$. Here the Li removal energy corresponds to the energy for the reaction,



where Li corresponds to an isolated Li atom. From table 6.5 $U_r \sim 6\text{eV}$ throughout the compositional range with very little variation from LiMnO_2 to $\text{Li}_{0.25}\text{MnO}_2$ given that the calculated energies are for unrelaxed structures. On going from $\text{Li}_{1.0}\text{MnO}_2$ to $\text{Li}_{0.5}\text{MnO}_2$ the changes in the Mulliken populations are small and close to linear. The hole density in $\text{Li}_{0.75}\text{MnO}_2$ and $\text{Li}_{0.5}\text{MnO}_2$ relative to $\text{Li}_{1.0}\text{MnO}_2$ is highly localised and found only on the oxygen sublattice, with local moments close to $1\mu_B$ aligned antiferromagnetically to the other Mn spin moments of the lattice as found previously in chapter 3 for the free hole in MnO^5 . In $\text{Li}_{0.5}\text{MnO}_2$ all the hole density is localised on a single oxygen plane, but it is possible that lattice relaxation may alter the hole density distribution. For Li compositions of less than 0.5, the large changes in the charge and spin distributions are attributed to the instability of these hypothetical C2/m monoclinic structures, but even so, Mn remains close to a d^5 configuration.

UHF calculations find the C2/m monoclinic structure of $\text{Li}_{0.5}\text{MnO}_2$ to be 0.5eV lower in energy than the corresponding orthorhombic Pmmn phase. This compares with the energy difference of only 0.03eV found previously for compositions of $\text{Li}_{1.0}\text{MnO}_2$, but where the Pmmn orthorhombic phase is lower in energy.

Figure 6.4 shows the empty O(p) atom projected DOS of the C2/m monoclinic phase of Li_xMnO_2 in the composition range $\text{Li}_{1.0}\text{MnO}_2$ to $\text{Li}_{0.25}\text{MnO}_2$. Significant changes below the CBE can be observed which increase with decreasing Li concentration. Only very small changes can be seen at the lower conduction band

edge and negligible changes in distribution at high energy. This confirms the Mulliken population analyses description of the hole density in that it is mostly O(p) and that it increases with decreasing Li concentration. Since the gap between the new states and the lower CBE approximates the band gap, UHF predicts a band gap of $\sim 1.9\text{eV}$ for $\text{Li}_{1.0}\text{MnO}_2$ which decreases to $\sim 0.2\text{eV}$ for Li_xMnO_2 as x goes towards zero.

The corresponding atom projected DOS of Mn(d) states, in the same compositional range as figure 6.4, is shown in figure 6.5. It is clear that the Mn(d) states remain almost unchanged apart from a trace of density below the CBE due to the partial p-d hybridisation with the new empty O(p) states.

x	$\Delta U_r(\text{HF})$	$\Delta U_r(\text{HFP})$	$q_M(\text{Mn})$	n_{3d}	$n_s(\text{Mn})$	$q_M(\text{O})$	$n_s(\text{O})$
1.0	6.13	6.41	2.03	4.85	3.95	-1.50	0.03
0.75	5.77	6.06	1.94	4.93	3.99	1.37 0.78	0.0 -0.96
			1.99	4.89	3.96	1.43 1.43	0.01 0.02
			2.04	4.85	3.95	1.52 1.52	0.02 0.02
			1.94	4.95	4.00	1.38 1.39	0.0 0.0
			(1.98)	(4.90)	(3.97)	(-1.35)	(-0.11)
0.5	5.62	6.05	1.91	4.95	4.00	1.29 0.74	-0.02 -0.97
			1.91	4.95	4.00	1.29 0.74	-0.02 -0.97
			1.95	4.92	3.99	1.40 1.40	-0.01 0.0
			1.95	4.92	3.99	1.40 1.40	-0.01 0.0
			(1.93)	(4.94)	(4.00)	(-1.21)	(-0.25)
0.25	5.51	5.95	1.92	4.95	4.03	1.37 1.38	-0.02 0.01
			1.59	5.32	4.68	1.43 1.43	-0.01 0.06
			1.61	5.31	4.70	1.52 1.52	0.06 -0.02
			1.91	4.96	4.04	1.37 0.78	0.06 0.96
			(1.76)	(5.13)	(4.36)	(-1.35)	(0.14)
0.0	-	-	1.58	5.34	4.76	-0.79	-0.88

Table 6.5. Variations of ΔU_r (eV/formula unit), the Mn Mulliken charge, q_M (e), 3d population, n_{3d} , and local Mn spin moment, n_s (μ_B), in FM (C2/m) Li_xMnO_2 as a function of x (the two columns of figures for $q_M(\text{O})$ and $n_s(\text{O})$ correspond to the two layers of the unit cell and the brackets denote average values)

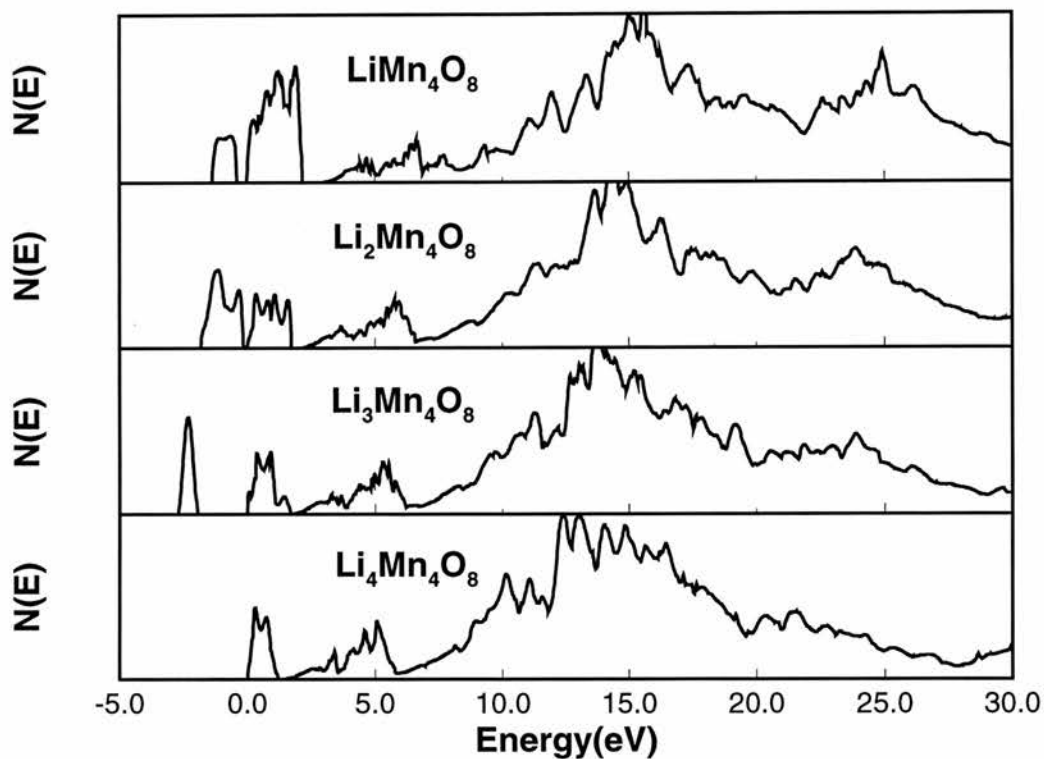


Figure 6.4. Empty O(p) DOS for LiMnO_2 ($\text{Li}_4\text{Mn}_4\text{O}_8$) to $\text{Li}_{0.25}\text{MnO}_2$ (LiMn_4O_8) where the zero of energy has been put at the CBE of LiMnO_2 here and in figure 6.5

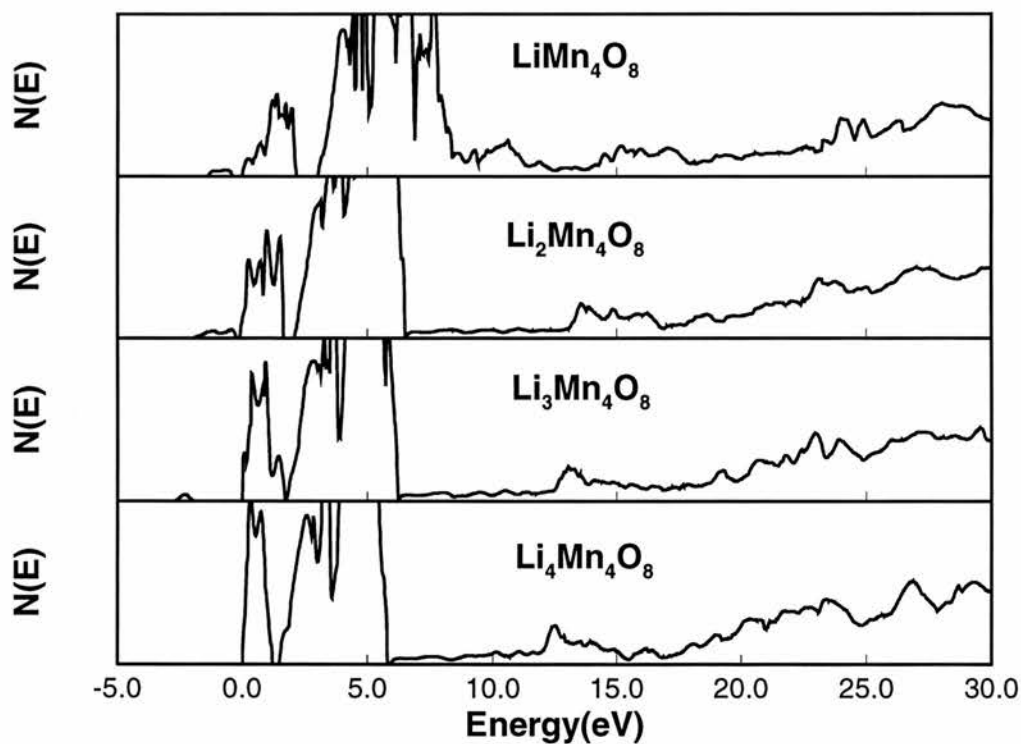


Figure 6.5. Empty Mn(d) DOS for LiMnO_2 ($\text{Li}_4\text{Mn}_4\text{O}_8$) to $\text{Li}_{0.25}\text{MnO}_2$ (LiMn_4O_8)

The precise location of the hole density can be obtained from the charge and spin density distribution projected onto one plane, exactly as in the case of MnO. Figure 6.6 illustrates the net spin density in the Mn (a), and two O planes (b,c) for compositions ranging from $\text{Li}_{1.0}\text{MnO}_2$ to $\text{Li}_{0.25}\text{MnO}_2$. The Mn spin density (a) remains unchanged, while up to composition, $\text{Li}_{0.5}\text{MnO}_2$, the spin density accumulates at only one of the O planes. As more Li is removed, it localises over both O planes which is in agreement with the Mulliken spin analyses over this composition range.

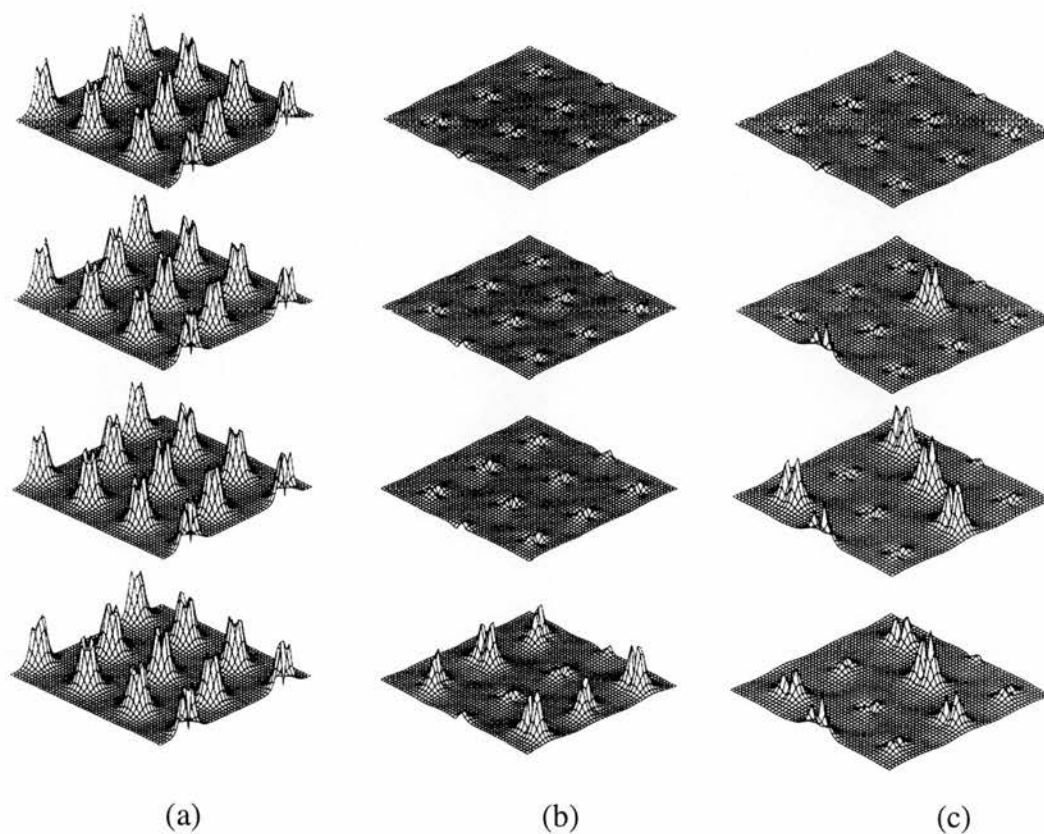


Figure 6.6. Net spin density distributions in an Mn plane (a) and two O planes adjacent to the Li layer (b,c) in LiMnO_2 to $\text{Li}_{0.25}\text{MnO}_2$, top to bottom respectively

6.3. Discussion

UHF calculations have been carried out on unrelaxed 1(P,P) supercells of $\text{Li}_n\text{Mn}_4\text{O}_8$ ($n = 0, 1, 2, 3, 4$) as part of an initial study of the new Li insertion system, monoclinic C2/m LiMnO_2 , in which Mn is conventionally thought to

vary from Mn^{3+} to Mn^{4+} . The results presented in chapters 3 and 4 of UHF calculations on MnO^5 , Li:MnO^7 and MnO_2^6 , formally, Mn(II), Mn(III) and Mn(IV), suggest a constant d^5 Mn valence configuration in this series with spin moments ranging from $5\mu_B$ to $3\mu_B$ due to an increase in covalency, and a primary objective here has been to verify that this is the case. As in previous chapters the results are presented in terms of Mulliken populations, spin density distributions and single particle DOS. Since no structural relaxations were carried out, all comments on the energetics are made with caution.

UHF calculations were carried out on two phases of the fully lithiated ferromagnetic material, C2/m monoclinic and the Pmmn orthorhombic. It is found that the orthorhombic phase is lower in energy by 0.02-0.03eV, which is consistent with the stability of these two phases. The Mulliken Mn 3d populations are 4.85 and 4.84 with similar local spin moments of $3.95\mu_B$ and $3.97\mu_B$ for the monoclinic and orthorhombic phases respectively. These findings are completely consistent with previous UHF studies, presented in chapters 3 and 4, which predict Mn(III) to have a valence configuration $\sim d^5$ and a local spin moment $\sim 4\mu_B$. The calculated orthorhombic spin moment, $3.97\mu_B$, shows good agreement with an experimental value of $3.69\mu_B^4$. The decreased local magnetic moment is attributed to overlap effects between the Mn d_{xz} orbital and two O atoms of the surrounding O_6 octahedron, one above and one below the Mn plane, as shown in figure 6.2. This results in partial σ_{p-d} covalent bonding. This suggested covalency is supported further by the atom projected DOS, from which the upper valence band is predominantly O(p) states but also contains a significant Mn(d) contribution throughout the band.

Table 6.6 shows a comparison of the total Mulliken charges, the Mn 3d and spin populations of MnO, LiMnO_2 (C2/m) and $\text{MnO}_2^{5,6,7}$. The interesting point to note from this table is that the Mulliken charge and 3d population on Mn remain close to 2 and 5 respectively throughout the formal valence range Mn(II) - Mn(IV). However, changes do occur in the Mn local spin moment and O Mulliken charge. The local spin moment on Mn reduces from $\sim 5\mu_B$ to $\sim 3\mu_B$ and the Mulliken charge on O reduces from ~ -2 to ~ -1 through the same range, Mn(II) - Mn(IV).

Oxide	$q_M(\text{Mn})$	n_{3d}	$n_s(\text{Mn})$	$q_M(\text{O})$
(Fm3m) MnO	1.86	5.11	4.92	- 1.86
(C2/m) LiMnO ₂	2.03	4.85	3.95	- 1.50
P4 ₂ /mnm MnO ₂	2.12	4.70	3.40	- 1.06

Table 6.6. Comparison of the total Mulliken charges, q_M (e), 3d population, n_{3d} , and local spin moments, n_s (μ_B), in FM MnO, LiMnO₂ and MnO₂

UHF calculations were also carried out on the lithium deficient C2/m monoclinic system at compositions, Li_{0.75}MnO₂, Li_{0.5}MnO₂, Li_{0.25}MnO₂, where it was found experimentally that monoclinic symmetry was retained up to a composition close to Li_{0.5}MnO₂². The changes which are found in the valence electronic structure at these compositions are consistent with the results presented in chapters 3 and 4 on electron deficient MnO⁵ and MnO₂⁶. On going from fully lithiated, LiMnO₂, to half lithiated, Li_{0.5}MnO₂, the Mn Mulliken 3d population and local spin moment changes very little, <2%, while the total Mn Mulliken charge changes by <5% which indicates that the $\sim d^5$ valence configuration is retained. On the other hand, the average Mulliken charge for O decreases from -1.5 to -1.2 with the majority of the hole predicted to localise over the O sites. The local spin moments are $\sim 1\mu_B$ and are antiferromagnetic to the surrounding FM lattice, forming spin polarons, as found previously for the free hole in MnO⁵. This change in electron configuration is accompanied by a 3% decrease in the Fermi energy from -8.63eV to -8.9eV and also a 6-8% decrease in the unrelaxed Li removal energy from 6.13eV to 5.62eV. These small percentage changes in the Fermi and Li removal energy up Li_{0.5}MnO₂ would almost certainly facilitate the use of this material as a good battery. For the fully lithiated orthorhombic phase however, the Fermi energy is $\sim 2\text{eV}$ higher than the monoclinic phase and decreases by $\sim 14\%$ on going from LiMnO₂ to Li_{0.5}MnO₂. For compositions containing < 50% Li, Li_{0.25}MnO₂ and Li_{0.0}MnO₂, large changes are observed in the valence electron configurations. This is attributed to the rather hypothetical unrelaxed structures at these compositions and it is expected that after relaxation, such large changes in the valence electron configurations might not be found.

UHF calculations, therefore, predict changes of only a few percent in the valence electron configuration on going from LiMnO_2 to $\text{Li}_{0.5}\text{MnO}_2$, the composition to which the monoclinic structure is known to remain stable.

Figure 6.7 shows a plot of the measured band gaps of MnO and MnO_2 ¹⁴ and calculated UHF band gap of monoclinic LiMnO_2 versus the formal valence state, where the theoretical value is estimated as the gap between the new O(p) states and the CBE. The striking feature to note is the apparent linear relationship.

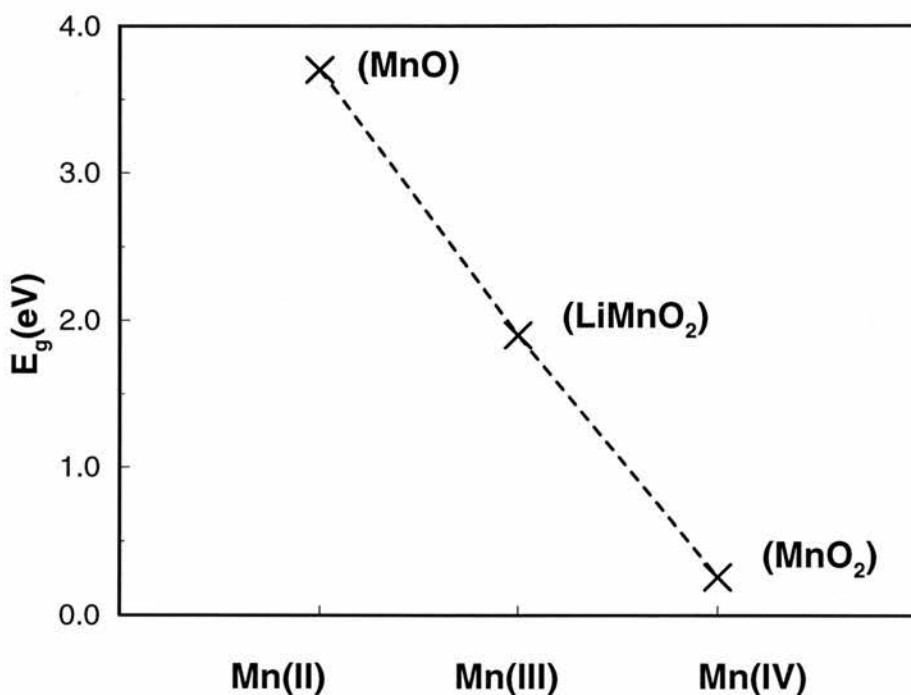


Figure 6.7. Comparison of the estimated band gap of LiMnO_2 compared with the experimental values for MnO and MnO_2 ¹⁴

Although no O K-edge or Mn K- or L-edge spectroscopy has been reported on Li_xMnO_2 to date, the predictions made here as to the $d^5\bar{L}$ nature of the hole states in $\text{Li}_n\text{Mn}_4\text{O}_8$ would be both directly and indirectly detectable using such spectroscopic techniques. This has been shown previously for $\text{Li}_{1-x}\text{Ni}_x\text{O}$ ¹¹, where the O K-edge spectrum showed a new oxygen peak which increased with Li concentration. This was subsequently confirmed by UHF calculations^{12,13} which

predicted new empty O(p) states (oxygen holes) on Li substitution in NiO. Figure 6.4 shows a similar prediction for Li_xMnO_2 with new empty O(p) states emerging $\sim 1.9\text{eV}$ below the CBE which increase with Li removal from LiMnO_2 ($\text{Li}_4\text{Mn}_4\text{O}_8$). As in the case of Li:NiO, therefore, these new empty O(p) states should be clearly evident in the O K-edge spectrum. This could also be verified indirectly from the absence of any detectable change in the Mn K-or L- edge spectra, as predicted by the empty Mn(d) states shown in figure 6.5.

6.4. Conclusions

The main conclusions of this chapter are: (1) that the UHF ground state valence configuration of monoclinic C2/m LiMnO_2 is d^5 with a local spin moment of $4\mu_B$, in an AF_3 spin arrangement and with a band gap of 1.9eV ; (2) that the FM orthorhombic Pmmn phase of LiMnO_2 is lower in energy than the monoclinic C2/m phase by 0.03eV but has almost identical valence configuration; (3) that the monoclinic symmetry is retained for Li_xMnO_2 within the limits $1 \leq x \leq 0.5$ and that the limiting Li concentration for AF_3 order is $x = 0.25$; (4) that in this compositional range, the evidence presented suggests that localised O(p) holes are formed which have strong spin polaron character and that the Mn valence remains unchanged; (5) for $x < 0.5$, UHF calculations of Li_xMnO_2 in an unrelaxed monoclinic C2/m structure, predict different valence configurations, a likely explanation of which is the unrealistic nature of these structures; (6) that the new O(p) states predicted below the CBE could be verified directly by O K-edge and indirectly by Mn K- and L-edge spectroscopies.

References

1. T.Nagaure, 3rd *Int. Battery Seminar* (Deerfield Beach, FL), 1990
2. A.R.Armstrong, and P.G.Bruce, *Nature*, 1996, **381**, 499
3. R.Hoppe, G.Brachtel, and M.Jansen, *Zeit.f.Anorgan.Allg.Chemie*, 1975, **417**, 1
4. J.E.Greedan, N.P.Raju, and I.J.Davidson, *J.Solid state Chem.*, 1997, **128**, 209
5. W.C.Mackrodt, and E-A.Williamson, *J.Phys.C: Condensed Matter Physics*, 1997, **9**, 6951
6. W.C.Mackrodt, and E-A.Williamson, *J.Chem.Soc., Faraday Trans.*, 1997, **93** (18), 3295
7. W.C.Mackrodt, and E-A.Williamson, *Ber.Bunsenges.Phys.Chem.*, 1997, **101**, - In press
8. D.J.Singh, *Phys.Rev. B*, 1997, **55**, 309
9. R.A.Evarestov, V.P.Smirnov, *J.Phys.C: Condensed Matter Physics*, 1997, **9**, 3023
10. M.D.Towler, N.L.Allan, N.M.Harrison, V.R.Saunders, W.C.Mackrodt, and E.Aprà, *Phys.Rev. B*, 1994, **50**, 5041
11. P.Kuiper, G.Kruizinga, J.Ghijsen, G.A.Sawatzky, and H.Verweij, *Phys.Rev.Lett.*, 1989, **62** 221
12. W.C.Mackrodt, N.M. Harrison, V.R.Saunders, N.L.Allan, and M.D.Towler, *Chem.Phys.Lett.*, 1996, **250** 66
13. W.C.Mackrodt, *Ber.Bunsenges.Phys.Chem.*, 1997, **101**, 169
14. W.H.Strehlow and E.L.Cook, *J.Phys.Chem.Ref.Data*, 1973, **2**, 163

Chapter 7

The Cation Valence Charge States in MnFe_2O_4

7.1. Introduction

A number of structural studies^{1,2} have been carried out on manganese ferrite, which show that it deviates slightly from the normal spinel structure of $[\text{Mn}]_A[\text{Fe}_2]_B\text{O}_4$, and has a cation distribution which can be represented as $[\text{Mn}_{0.8}\text{Fe}_{0.2}]_A[\text{Mn}_{0.2}\text{Fe}_{1.8}]_B\text{O}_4$. Several experimental investigations^{3,4,5} have been carried out to determine the nature of the cation valence states on these two sites, A and B. From conductivity³ and thermogravimetric measurements⁴ and infra-red and optical spectra analyses⁵, a simple cation arrangement has been proposed where the A sites are occupied only by divalent ions and the B sites by trivalent ions, formally thus $[\text{Mn}_{0.8}^{2+}\text{Fe}_{0.2}^{2+}]_A[\text{Mn}_{0.2}^{3+}\text{Fe}_{1.8}^{3+}]_B\text{O}_4$. For this arrangement to occur, the following charge transfer would have to take place,

$\text{Mn}_B^{2+} + \text{Fe}_A^{3+} \rightarrow \text{Mn}_B^{3+} + \text{Fe}_A^{2+}$. However, Sawatsky *et al*² found no evidence of Fe^{2+} in the Mössbauer spectra of MnFe_2O_4 , while Harrison *et al*⁶ and Lotgering⁷ deduced energies of approximately +1eV and +0.3eV for the above charge transfer reaction from ionisation and crystal field energies⁶ and from electrical conductivity measurements and Seebeck voltage studies⁷ respectively. Pseudopotential LDA calculations⁸ have also been carried out on manganese ferrite from which the ground state was found to be metallic which is contrary to experimental findings. In view of these studies, and in light of the results presented in chapters 3, 5 and 6 on the nature of the Mn(III) state, Hartree-Fock calculations have been carried out in an attempt to clarify the cation valence charge states in MnFe_2O_4 .

7.2. Results

The unit cell data used to construct the cubic spinel, space group $\text{Fd}3\text{m}$ and lattice constant 8.511 Å, was that reported by Koenig and Chol⁹. To represent the unit cell, $\frac{1}{4}$ of the full unit cell was constructed. This contained two formula units or $\text{Mn}_2\text{Fe}_4\text{O}_8$. The normal spinel was represented by the following arrangement,

$[\text{Mn}_2]_A[\text{Fe}_4]_B\text{O}_8$, where A denotes tetrahedral sites and B denotes octahedral sites. To simulate the inverse spinel, the two Mn atoms were exchanged with two Fe atoms, giving, $[\text{Fe}_2]_A[\text{Mn}_2\text{Fe}_2]_B\text{O}_8$. All possible configurations of the inverse structure were checked and were found to have the same Hartree-Fock energy, indicating that all were equivalent. Although it is known that at low temperatures, MnFe_2O_4 is antiferromagnetic, the ferromagnetic spin arrangement was used for convenience, as previous studies on MnO and NiO¹⁰ have shown that Hartree-Fock spin distribution and projected densities of states are almost independent of the magnetic state.

In an attempt to determine the nature of the ground state of MnFe_2O_4 , both UHF and RHF calculations were carried out with various starting charge states and spin arrangements. The lowest energy solution is found for the normal spinel arrangement, with both normal and inverse structures having insulating ground states. No converged metallic solutions are found to be lower in energy than the UHF insulating solutions reported here, which is in complete agreement with experimental findings.

Table 7.1 shows a comparison of the total Mulliken populations for MnO, α - Fe_2O_3 , and MnFe_2O_4 in the normal and inverse structures. There are three points worth noting from this table: first, the formal charges of Mn and Fe in both the normal and inverse structures are close to 1.9e and 2.6e respectively; second, on comparison of the Mulliken populations for Mn and Fe in the normal and inverse structures with the corresponding oxides, the charges are found to be very similar, < 0.15% difference; third, there is very little difference in the Mulliken populations of Mn and Fe in the normal and inverse structures.

Oxide	q_{Mn}	q_{Fe}	q_{O}
MnO	23.139	-	9.861
α - Fe_2O_3	-	23.398	9.734
MnFe_2O_4 (n)	23.146	23.397	9.765
MnFe_2O_4 (i)	23.168	23.375(A) 23.381(B)	9.765 9.775

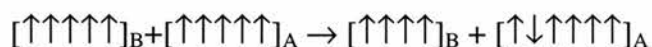
Table 7.1 Total Mulliken populations, q_x , in MnO, α - Fe_2O_3 and MnFe_2O_4

Taking a closer look at the d electron populations, shown in table 7.2, the total d electron populations do not change very much, although some differences are found in the e_g and t_{2g} levels of Fe at the A and B sites in the inverse spinel. Overall however, negligible differences in charge distribution are found from the Mulliken population analyses for Mn and Fe in the normal and inverse structures.

Structure	Cation	$q_X(3d)$	$q_X(e_g)$	$q_X(t_{2g})$
MnFe ₂ O ₄ (n)	Mn	5.110	2.026	3.084
	Fe	5.300	2.240	3.060
MnFe ₂ O ₄ (i)	Mn	5.150	2.133	3.017
	Fe(A)	5.271	2.052	3.219
	Fe(B)	5.291	2.232	3.059

Table 7.2 Mulliken d-electron populations, $q_X(i)$, in MnFe₂O₄

For the suggested charge transfer to take place, $Mn_B^{2+} + Fe_A^{3+} \rightarrow Mn_B^{3+} + Fe_A^{2+}$, a change in spin would have to follow as shown below,



Therefore a comparison of the net (or $\uparrow - \downarrow$) spin density would provide an invaluable insight into the occurrence of any charge transfer which might be taking place. Figures 7.1, 7.2 and 7.3 show such spin density plots which are all on the same scale. In figure 7.1, the net spin density of Mn is shown, (i) in the normal spinel (at an A site), (ii) in the inverse spinel (at a B site) and (iii) the difference between these two spin densities. Figure 7.2 shows similar plots for Fe, (i) in the normal spinel (at a B site), (ii) in the inverse spinel (at an A site) and (iii) the difference between these two.

As seen in figures 7.1(iii) and 7.2(iii), there are small differences in the spin densities on Mn and Fe in the two sites, A and B, but these can be attributed to the change in coordination as the magnitude of the differences is not large enough to be associated with charge transfer.

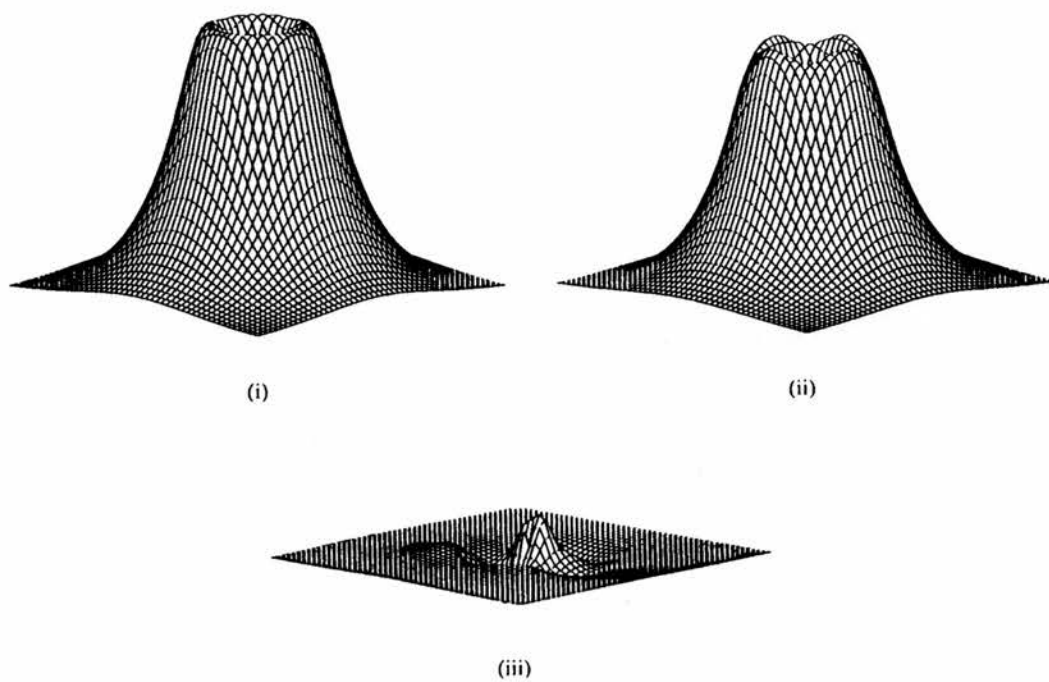


Figure 7.1 Net spin density distributions in a $\{001\}$ plane through Mn in the normal spinel structure (i), in the inverse spinel structure (ii) and their difference (iii)

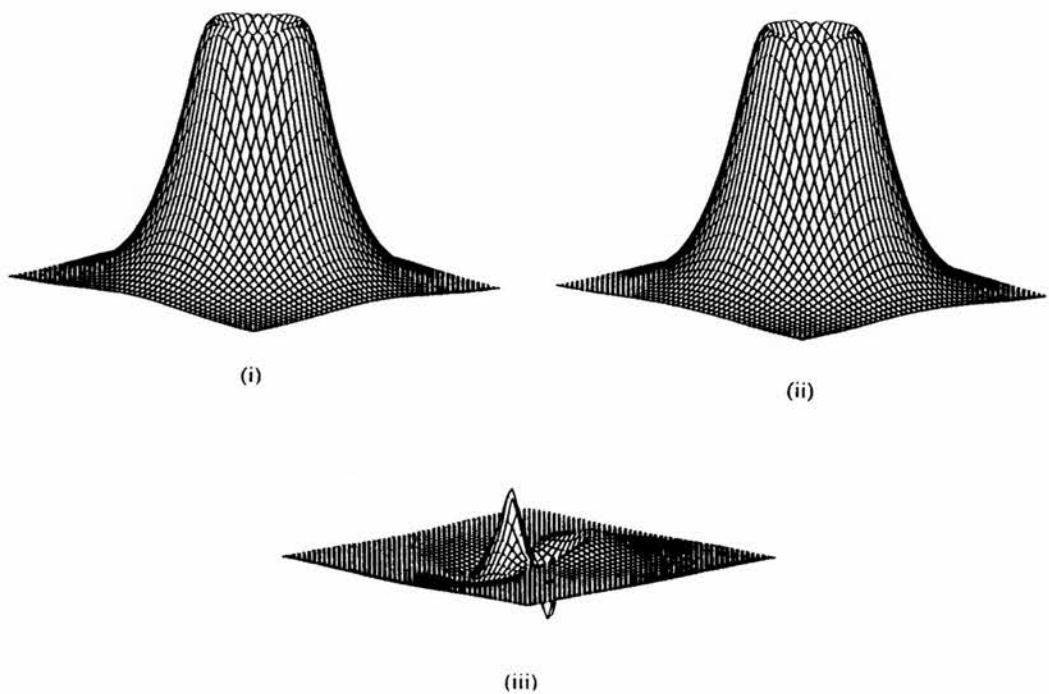


Figure 7.2 Net spin density distributions in a $\{001\}$ plane through Fe in the normal spinel structure (i), in the inverse spinel structure (ii) and their difference (iii)

Figure 7.3 shows the net spin density of Fe at a B site in (i) the normal spinel (ie figure 7.2(i)) and (ii) in the inverse spinel structure and (iii) their difference. Figure 7.3(iii) shows no difference in spin density between Fe in the B site of these two structures.

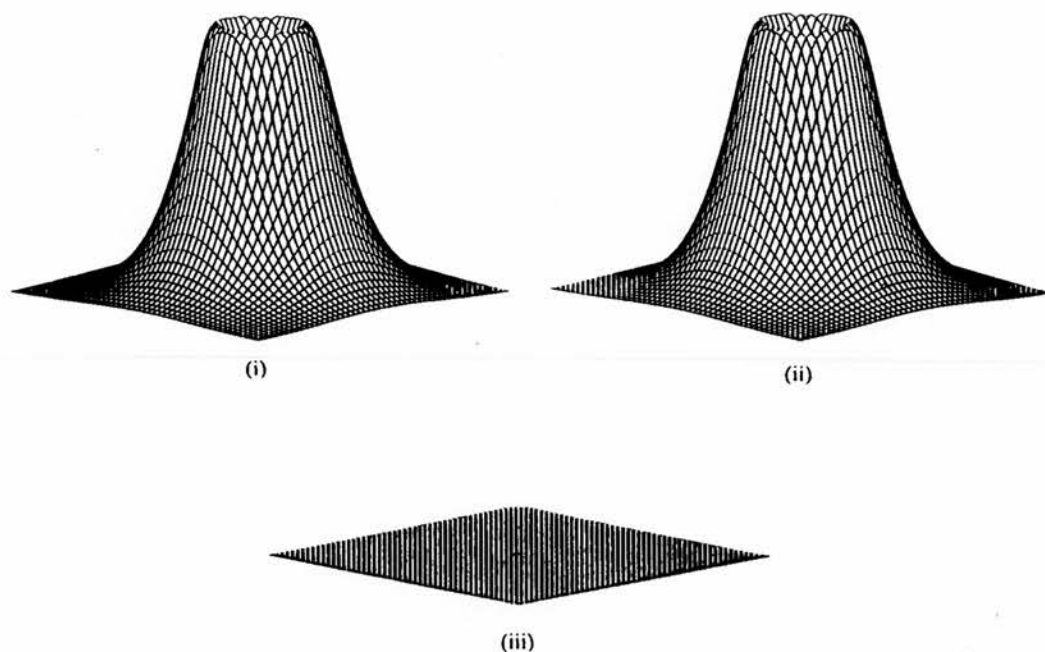


Figure 7.3 Net spin density distributions in a $\{001\}$ plane through a B site Fe in (i) the normal spinel structure, (ii) in the inverse spinel structure and (iii) their difference

The atom and spin projected densities of states provides even more information on the electronic structure. Figure 7.4 shows a comparison of the upper valence bands of normal MnFe_2O_4 (upper) with $\alpha\text{-Fe}_2\text{O}_3$ (lower). Both plots show similar features. The states which lie to higher energy are O(2p) in nature, and are separated from the Fe(d) band by a gap of about 5eV. The O(2p) band width in MnFe_2O_4 is 7eV and 7.3eV in $\alpha\text{-Fe}_2\text{O}_3$. The Fe(d) bands are 1.5eV and 2.1eV for MnFe_2O_4 and $\alpha\text{-Fe}_2\text{O}_3$ respectively. There is a certain degree of covalency in each system illustrated by the dispersion of Fe states in the mainly O(2p) band, and O in the Fe(d) band.

Turning now to the Mn states, the valence band of normal MnFe_2O_4 is compared with that of MnO in figure 7.5.

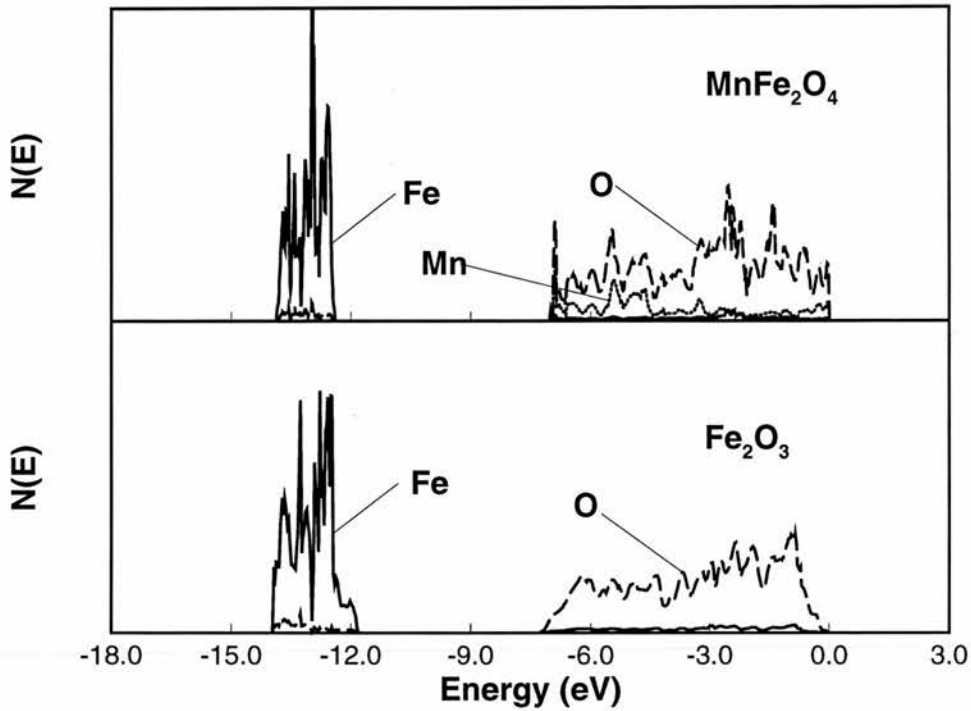


Figure 7.4 Comparison of the projected DOS of normal MnFe_2O_4 (upper) with Fe_2O_3 (lower). In figures 4-8 the solid line refers to the Fe DOS, the dashed line to O and the dotted line to Mn.

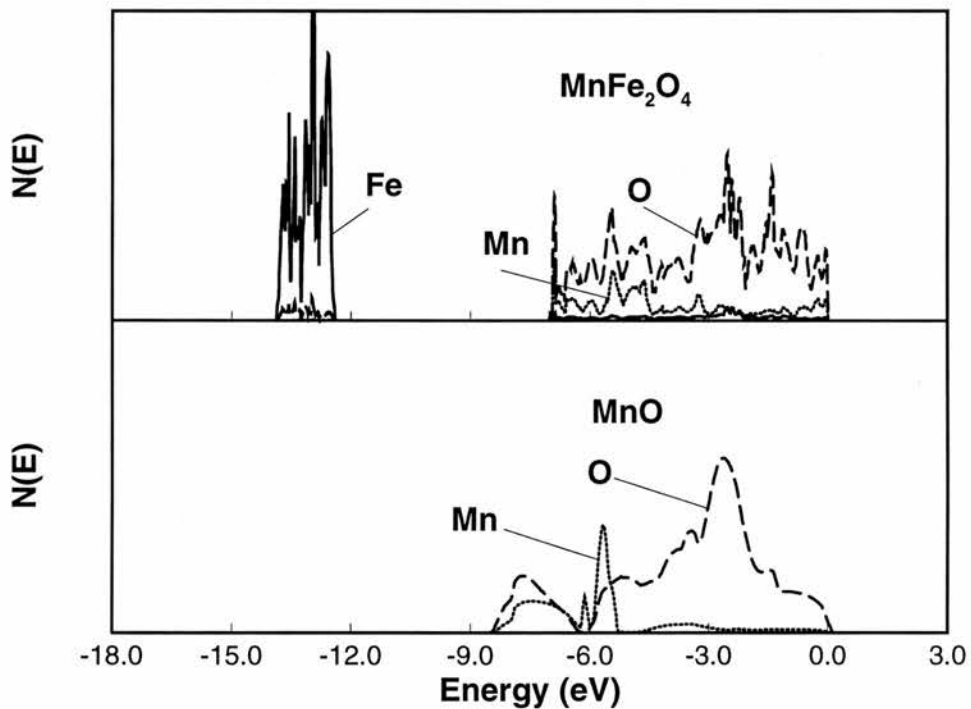


Figure 7.5 Comparison of the projected DOS of normal MnFe_2O_4 (upper) with MnO (lower). In the lower panel the O DOS has been multiplied by a factor of four for a direct comparison with the upper panel.

Here, the Mn states are dispersed differently in MnO than in the spinel structure. The Mn states in MnO are found towards the lower energy range of the mainly O(2p) band, whereas in MnFe_2O_4 , the Mn states are evenly dispersed throughout the same band. This is due to the increased ionicity in MnO and the difference in coordination between the two structures.

A comparison of the upper valence band states of normal (lower) and inverse (upper) MnFe_2O_4 is shown in figure 7.6. These plots differ in a number of respects. In the inverse structure, the Fe A site states are found to have lower energy than the Fe B site states with a separation of $\sim 0.6\text{eV}$. A redistribution of the Mn states takes place from the normal to the inverse structures, with most of the weighting towards the upper end of the O(2p) band in the inverse structure as opposed to the lower end in the normal structure. Also, a weak insulating band has appeared in the inverse structure at $\sim 0.7\text{eV}$ above the upper edge of the O(2p) band which has an equal number of O and Mn states.

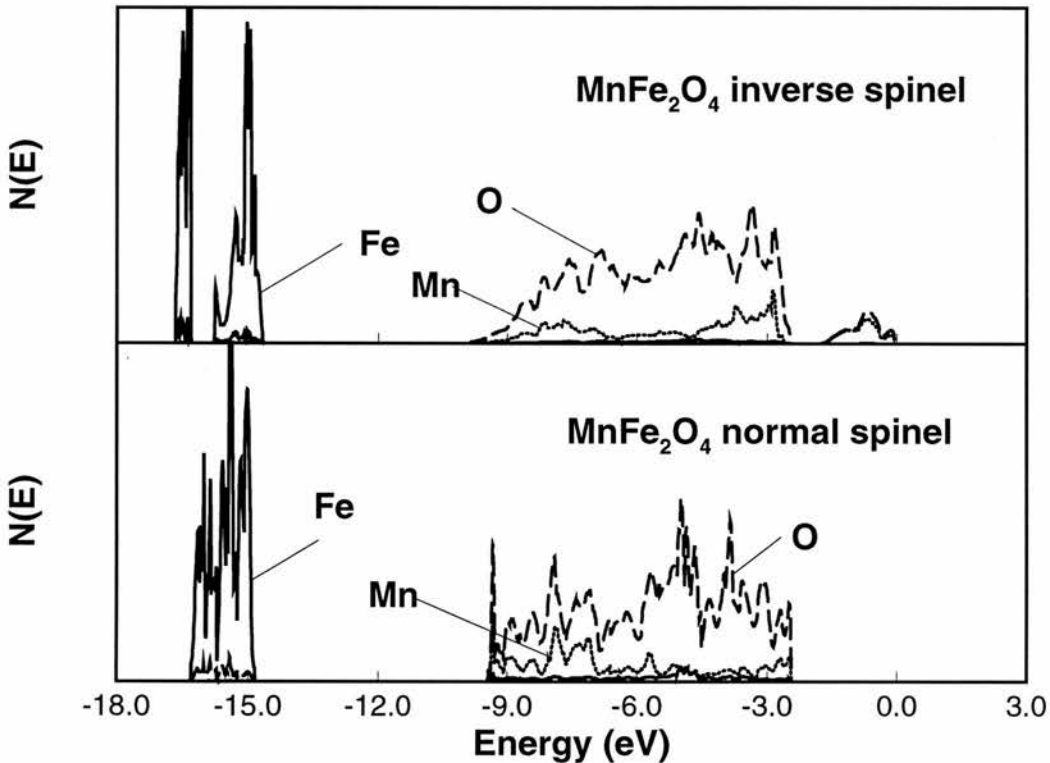


Figure 7.6 Comparison of the projected DOS of MnFe_2O_4 : inverse (upper) and normal (lower)

The spin projected DOS of normal and inverse MnFe_2O_4 is shown in figures 7.7 and 7.8 respectively. For the normal spinel, figure 7.7, the Mn and Fe d bands are entirely spin polarised, whereas the O(2p) band is almost completely spin paired.

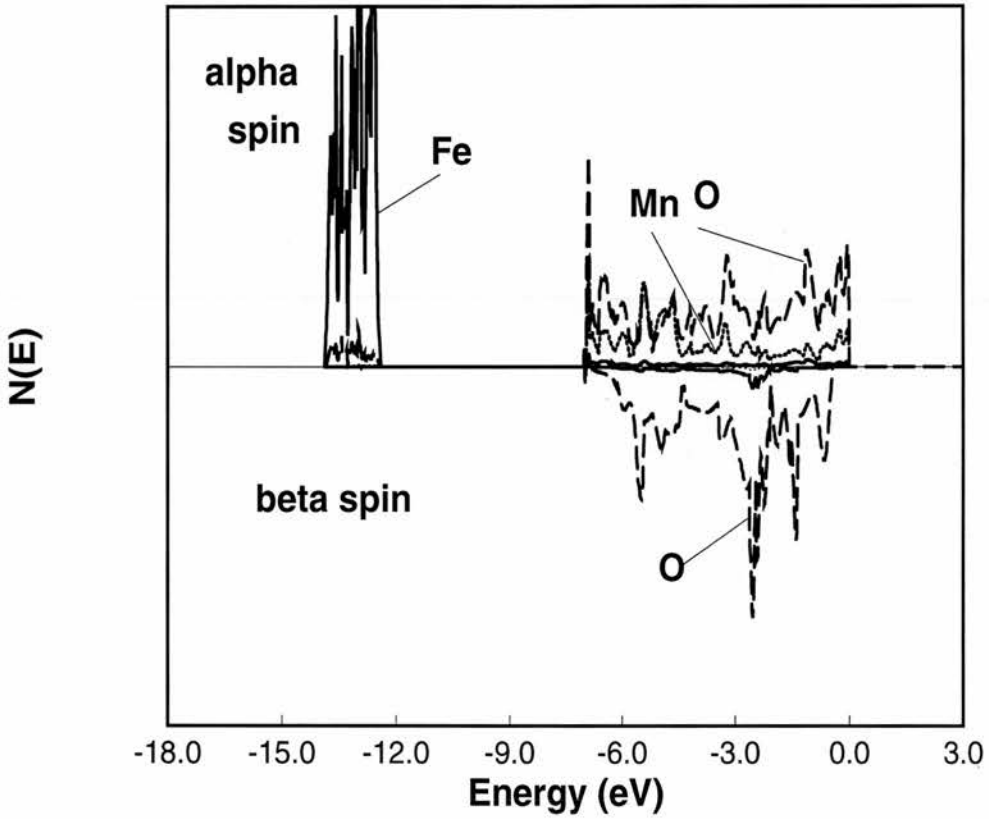


Figure 7.7 Spin projected DOS of normal MnFe_2O_4 : \uparrow (upper) \downarrow (lower)

The states above the O(2p) upper edge in the inverse structure, figure 7.8, are also entirely spin polarised which results in a slight polarisation of the O(2p) band.

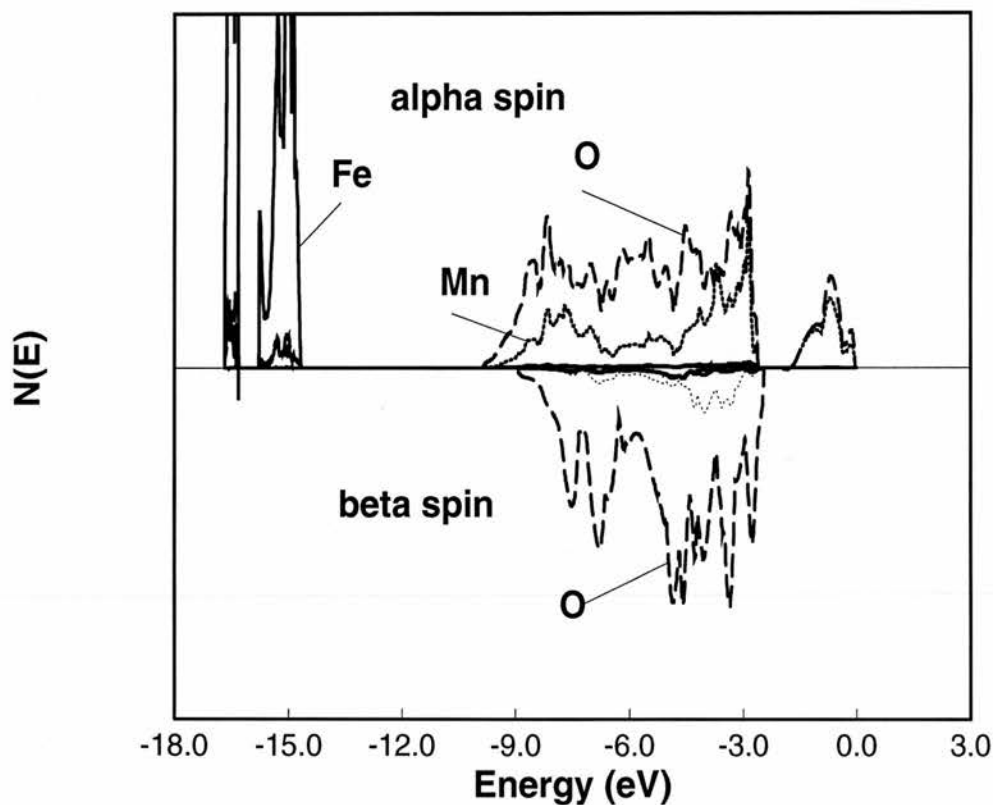


Figure 7.8 Spin projected DOS of inverse MnFe_2O_4 : \uparrow (upper) \downarrow (lower)

7.3. Discussion

The nature of the valence states of Mn and Fe in the normal and inverse MnFe_2O_4 spinel have been investigated using *ab initio* periodic Hartree-Fock calculations in light of the proposed charge transfer reaction,

$\text{Mn}_B^{2+} + \text{Fe}_A^{3+} \rightarrow \text{Mn}_B^{3+} + \text{Fe}_A^{2+}$. From Mulliken population, net spin density and DOS analyses, no evidence of this charge transfer is found. Although a slight redistribution of Mulliken population is apparent in the e_g and t_{2g} levels of the cations from A site occupancy to B site occupancy, the total Mulliken population of the cations does not change significantly. Net spin density difference plots, figures 7.1(iii) and 7.2(iii) show that a small difference in spin does occur for Mn and Fe between the two sites, the magnitude of which is not large enough to suggest that appreciable charge transfer had taken place. The DOS plots in figure 7.6 show that there are differences in the electronic structures of the normal and

inverse spinel, the main difference being the spin polarised insulating states found $\sim 2.5\text{eV}$ above the O(2p) band edge. Further evidence which supports the findings of this study came from atomistic simulations by Islam and Catlow¹¹ of the following charge transfer reaction, $\text{Ni}_A^{2+} + \text{Mn}_B^{3+} \rightarrow \text{Ni}_A^{3+} + \text{Mn}_B^{2+}$. The lattice energy contributions were calculated as -0.87eV to -1.14eV , which when added to the difference in the third ionisation potentials of Mn and Ni ($+1.5\text{eV}$), give an energy for the above reaction of between 0.36eV and 0.63eV . Using the same rationale for the present system, and assuming a lattice energy contribution of $\sim -1.0\text{eV}$, the reaction energy is estimated to be $\sim +2\text{eV}$ which suggests that the charge transfer is energetically unfavourable. This is in complete agreement with the findings presented here.

7.4. Conclusions

The principal conclusion of this chapter is that there is no evidence from UHF calculations to support the proposed simple cation distribution,



References

1. J.M.Hastings and L.M.Corliss, *Phys.Rev.*, 1956, **104**, 328
2. G.A.Sawatzky, F.Van Der Woude and A.H.Morrish, *Phys.Rev.*, 1969, **187**, 747
3. T.E.Whall, N.Salerno, Y.G.Proykova and V.A.M.Brabers, *Phil.Mag.B*, 1987, **56**, 99
4. P.Tailhades, C.Sarda, A.C.Vajpei, A.Rousset and B.Gilot, *Solid State Ionics*, 1989, **32/33**, 734
5. F.Petit and M.Lenglet, *Solid State.Comm.*, 1993, **86**, 67
6. F.W.Harrison, W.P.Osmond and R.W.Teale, *Phys.Rev.*, 1956, **104**, 328
7. F.K.Lotgering, *J.Phys.Chem.Solids*, 1964, **25**, 95
8. M.Pénicaud, B.Siberchicot, C.B.Sommers and J.Kübler, *J.Magnet.and Magnet.Mater.*, 1992, **103**, 212
9. U.Koenig and G.Chol, *J. Appl. Cryst.*, 1968, **1**, 124
10. M.D.Towler, N.L.Allan, N.M.Harrison, V.R.Saunders, W.C.Mackrodt and E.Aprà, *Phys.Rev. B*, 1994, **50**, 5041
11. M.S.Islam and C.R.A.Catlow, *J.Phys.Chem.Solids*, 1988, **49** 119

Chapter 8

The Non Defective Surfaces of TiO₂ Rutile

8.1. Introduction

TiO₂ finds applications as a photocatalyst, both in the purification and photolysis of water^{1,2,3}, a catalyst support, having a strong interaction with group VIII metals^{4,5} and as a white pigment used extensively in the paint and polymer industries⁶. These and other uses indicate that TiO₂ is a commercially important material so that a detailed knowledge of its surface properties, especially surface geometries and electronic structure, would be an advantage in improving existing processes and developing future applications which depend on TiO₂ rutile. This chapter focuses on the atomic relaxations and associated surface energies of the non defective low index surfaces of TiO₂ while the following chapter investigates the electronic structure of the stoichiometric and defective surfaces.

Prior to 1994, not a great deal of detailed theoretical investigation had been carried out into the surface geometries of TiO₂ rutile due largely to the relative complexity of the system and the subsequent computational requirements. In 1994 two studies were reported, the first by Freeman *et al*⁷ who investigated the geometry of the relaxed stoichiometric {110} surface of TiO₂ rutile based on the FLAPW method. The second was by Ramamoorthy *et al*⁸ who carried out an extensive study of TiO₂ rutile based on plane wave local density approximation (LDA) calculations using Vanderbilt pseudopotentials to estimate the structure and energetics of the {110}, {100}, {011} and {001} stoichiometric surfaces. However, the relaxations which were proposed by Freeman *et al*⁷ for the {110} surface differed markedly from those reported by Ramamoorthy *et al*⁸.

Experimentally, the surface structures of oxides are very difficult to determine. Low energy electron diffraction (LEED) and scanning tunneling microscopy (STM) have been the two main techniques used to investigate oxide surfaces, although recent advances in glancing angle x-ray diffraction suggests that this will be the principle tool for accurate surface structure determination in the future. Only a few detailed investigations have been carried out on the relaxed geometries of non defective TiO₂ surfaces with the bulk of the literature devoted

to probing the various surface reconstructions. One such investigation was carried out by Mason *et al*⁹ in 1991 using a model system together with LEED data to propose a structure for the non defective {001} surface. The atomic relaxations of this structure, however, did not agree with those proposed by Ramamoorthy *et al*⁸.

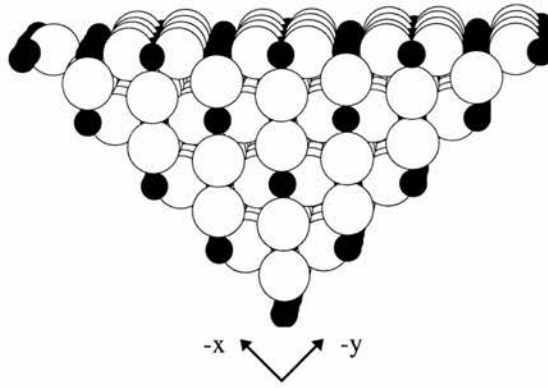
In view of the discrepancies in the atomic displacements of the stoichiometric {110} surface reported by Ramamoorthy *et al*⁸ and Freeman *et al*⁷ and those of the {001} reported by Ramamoorthy *et al*⁸ and Mason *et al*⁹, periodic Hartree-Fock calculations have been carried out on the five lowest index surfaces of TiO₂ rutile in an attempt to clarify the relaxed surface structures and to calculate their relative stabilities.

Since this work was carried out a number of other theoretical investigations have been reported both of the stoichiometric and defective surfaces of TiO₂. These include an independent *ab initio* Hartree-Fock study by Reinhardt and Hess¹⁰ on the relaxed {001}, {100} and {110} surfaces, spin polarised density functional theory calculations on the {100} and {110} surfaces by Lindan *et al*^{11,12} and atomistic simulations by Oliver *et al*¹³ and Purton *et al*¹⁴ on the stoichiometric {011}, {110}, {100}, {221} and {110}, {001}, {100} surfaces respectively. Also a very recent experimental study using surface x-ray diffraction techniques¹⁵ has provided detailed atomic displacements of the relaxed {110} surface of TiO₂.

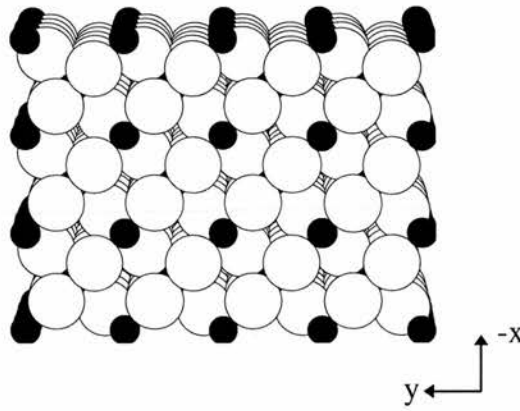
8.2. Results

UHF calculations were carried out on the defect free bulk and surfaces of TiO₂, rutile. The lattice parameters used were $a = 4.5613 \text{ \AA}$ and $c = 3.0197 \text{ \AA}$, which were obtained previously from a full structural optimisation of the bulk¹⁶. To simulate the required surfaces, infinite two dimensional slabs were constructed parallel to the desired direction. Relaxations were performed on the topmost surface layers on both sides of the slab to maintain the symmetry, with at least three layers in the middle of the slab representing the bulk. The lattice structures of the unrelaxed surfaces are shown in figure 8.1, and the corresponding stacking sequences in figure 8.2.

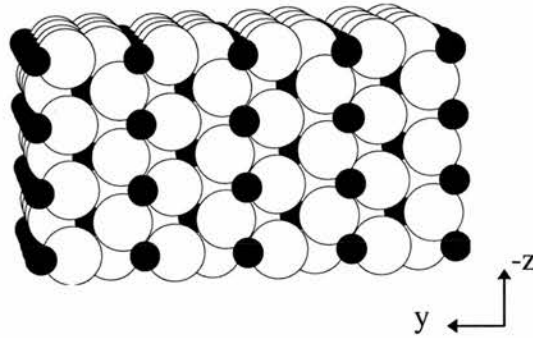
(a) $\{110\}$



(b) $\{100\}$



(c) $\{001\}$



(d) $\{011\}$

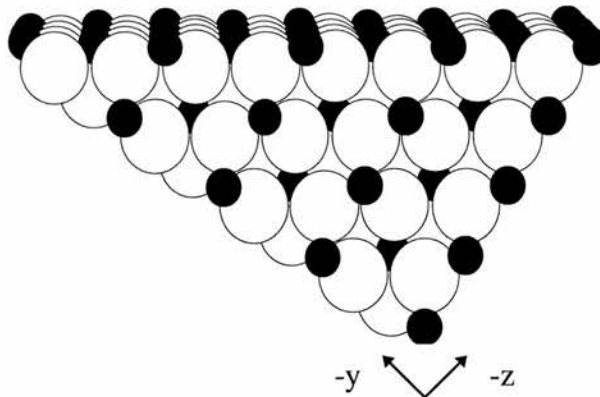


Figure 8.1. The lattice structures of the (a) $\{110\}$, (b) $\{100\}$, (c) $\{001\}$ and (d) $\{011\}$ slabs

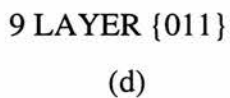
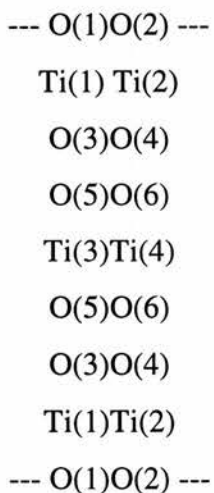
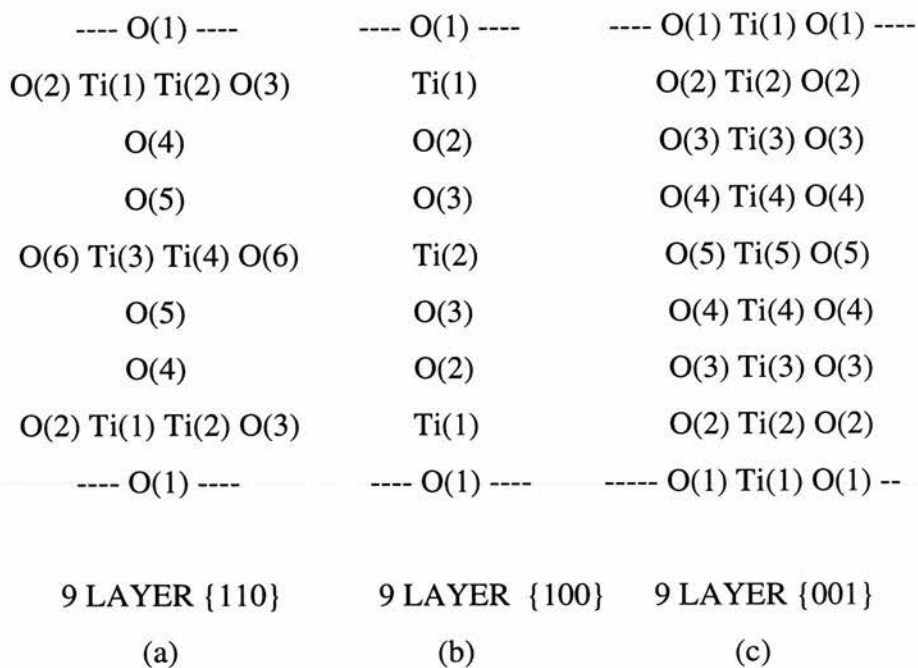


Figure 8.2. The stacking sequences of the (a) {110}, (b) {100}, (c) {001} and (d) {011} slabs

UHF calculations for bulk TiO₂ converged to RHF solutions, as they should for a non magnetic system, with a total energy of -998.37599858 au per TiO₂ unit. This energy was used throughout to calculate the surface energies, which are all quoted in units of Jm⁻².

Starting with the {110} surface, the lattice structure is shown in figure 8.1(a) and the stacking sequence in figure 8.2(a). UHF calculations were carried out on 9, 12 and 15 layers of the unrelaxed slab, resulting in surface energies of 2.734 Jm⁻², 2.721 Jm⁻² and 2.723 Jm⁻² respectively, which suggest that the surface energy is close to converged at 12 layers. The displacements of the relaxed {110} surface reported by Ramamoorthy *et al*⁸, the z components of which is shown in the third column of table 8.1, were then used to simulate the corresponding relaxed {110} surface using 6, 9, 12 and 15 layer slabs. These result in surface energies of 1.435Jm⁻², 1.918Jm⁻², 1.831Jm⁻² and 2.199Jm⁻² respectively. Calculations were also carried out for the relaxed structure reported by Freeman *et al*⁷, the z component of the displacements are also shown in table 8.1, but here the limited relaxation could only be accommodated using 6 layer slabs resulting in an energy of 2.141Jm⁻².

Atom Type	Layer	δz LDA	δz present study	δz FLAPW	δz Reinhardt and Hess	δz EXPT
O	1	-0.0635	-0.09	-0.156	-0.14	-0.27
Ti	1	-0.1693	-0.117	-0.180	-0.146	-0.16
Ti	1	0.1323	0.147	-0.049	0.092	0.12
O	1	0.1270	0.110	-0.115	0.066	0.05
O	2	0.1270	0.110	-0.115	0.066	-0.16
O	3	-0.0741	-0.028	-	-0.072	0.05
O	4	0.0159	-	-	-	0.0

Table 8.1 Comparison of the atomic (001) or z displacements (Å) for the Ramamoorthy *et al*⁸ (LDA), Freeman *et al*⁷ (FLAPW), Hartree-Fock (present) and experimental¹⁵ {110} surfaces

Independent Hartree-Fock calculations of surface relaxation, by direct energy minimisation, were then carried out on 9 layers of the {110} slab¹⁷, and again the z atomic displacements are shown in the fourth column of table 8.1, resulting in a relaxed surface energy of 1.765 Jm⁻². For these three calculated {110} surface structures, no relaxation was found in the x direction and only minimal displacements in the y direction, ± 0.037 , ± 0.072 and ± 0.73 for the O atoms of the second and first layers of the LDA, FLAPW and Hartree-Fock structures respectively. Table 8.2 contains details of the Hartree-Fock surface energies based on the relaxed {110} surface structures reported by Ramamoorthy *et al*⁸ and Freeman *et al*⁷ and that reported here. From this there is evident agreement between the Hartree-Fock and Ramamoorthy structures but not with that reported by Freeman *et al*⁷.

Surface Type	No. of Layers	Surface Energy	Relaxation Energy
Unrelaxed	9	2.734	-
Ramamoorthy relaxed	9	1.918	0.816
Freeman relaxed	6	2.141	0.593
HF relaxed	9	1.765	0.969

Table 8.2 Comparison of the Hartree-Fock calculated surface energies (Jm⁻²) of the unrelaxed and relaxed {110} surface

Table 8.3 contains a comparison of the Hartree-Fock and LDA {110} surface energies based on the relaxed structure of Ramamoorthy *et al*⁸ as a function of slab thickness.

No of Layers	Unrelaxed HF Surface Energy	Relaxed HF Surface Energy	Unrelaxed Ram. Surface Energy	Relaxed Ram. Surface Energy
9	2.734	1.918	1.79	1.10
12	2.721	1.831	1.73	0.76
15	2.723	2.199	1.79	0.96

Table 8.3 Comparison of surface energies (Jm⁻²) with number of layers for the unrelaxed and Ramamoorthy relaxed {110} surfaces

Only one relaxed structure was investigated for the {100} surface, namely, that proposed by Ramamoorthy *et al*⁸. The lattice arrangement and stacking sequence of the unrelaxed surface are illustrated in figures 8.1(b) and 8.2(b). Hartree-Fock calculations were carried out for both the 15 and 21 layer slabs of the unrelaxed and relaxed {100} surfaces. Details of the calculated unrelaxed and relaxed surface energies are given in table 8.4.

No of Layers	Unrelaxed Surface Energy	Relaxed Surface Energy	Relaxation Energy
15	2.970	2.189	0.781
21	2.970	2.229	0.741

Table 8.4 Comparison of the Hartree-Fock surface energies (Jm^{-2}) with number of layers of the unrelaxed and Ramamoorthy relaxed {100} surfaces

The lattice structure and stacking sequence of the {001} surface are shown in figures 8.1(c) and 8.2(c). UHF calculations of 5 and 7 layer slabs of the unrelaxed surface result in surface energies of 4.046Jm^{-2} and 4.044Jm^{-2} respectively. The displacements of the relaxed {001} surfaces determined by Ramamoorthy *et al*⁸ and Mason *et al*⁹ from LEED, shown in tables 8.5 to 8.7, were used to calculate the corresponding Hartree-Fock surface energies. These were found to be 3.697Jm^{-2} , 3.542Jm^{-2} and 3.459Jm^{-2} for the Ramamoorthy *et al*⁸ 5, 7 and 9 layer slabs of the relaxed surface respectively and 3.888Jm^{-2} for the 5 layer slab of the Mason *et al*⁹ relaxed surface. As for the {110} surface, an independent Hartree-Fock surface relaxation¹⁷ was carried out for the 7 layer slab of the {001} surface, the atomic displacements of which are also shown in tables 8.5 to 8.7. This results in a relaxed surface energy of 2.823Jm^{-2} . All these energies are collected in table 8.8, while table 8.9 shows the surface energies of the Ramamoorthy *et al*⁸ structure as a function of slab thickness.

Atom Type	Layer	δ_x LDA	δ_x LEED	δ_x present study
Ti	1	0.0	0.0	0.0
O	1	-0.1	0.004	-0.09896
O	1	0.1	-0.004	0.09896
Ti	2	0.0	0.0	0.0
O	2	-0.037	-0.0139	0.004749
O	2	0.037	0.0139	-0.004749
Ti	3	0.0	-	-
O	3	-0.026	-	-
O	3	0.026	-	-
Ti	4	0.0	-	-
O	4	-0.026	-	-
O	4	0.026	-	-

Table 8.5 Comparison of atomic (100) displacements (\AA) at the $\{001\}$ surface

Atom Type	Layer	δ_y LDA	δ_y LEED	δ_y present study
Ti	1	0.0	0.0	0.0
O	1	0.1	-0.004	0.09896
O	1	-0.1	0.004	-0.09896
Ti	2	0.0	0.0	0.0
O	2	-0.037	-0.0139	0.004749
O	2	0.037	0.0139	-0.004749
Ti	3	0.0	-	-
O	3	0.026	-	-
O	3	-0.026	-	-
Ti	4	0.0	-	-
O	4	-0.026	-	-
O	4	0.026	-	-

Table 8.6 Comparison of atomic (010) displacements (\AA) at the $\{001\}$ surface

Atom Type	Layer	δz LDA	δz LEED	δz present study
Ti	1	-0.33	-0.0531	-0.197138
O	1	0.033	-0.0858	-0.051104
O	1	0.033	-0.0858	-0.051104
Ti	2	0.33	0.0286	0.152217
O	2	-0.044	0.0419	0.006608
O	2	-0.044	0.0419	0.006608
Ti	3	-0.22	-	-
O	3	0.027	-	-
O	3	0.027	-	-
Ti	4	0.22	-	-
O	4	-0.033	-	-
O	4	-0.033	-	-

Table 8.7 Comparison of atomic (001) displacements (\AA) at the {001} surface

Surface Type	No. of Layers	Surface Energy
Unrelaxed	7	4.044
Ramamoorthy relaxed	7	3.542
Mason relaxed	5	3.888
Hartree-Fock relaxed	7	2.823

Table 8.8 Comparison of the Hartree-Fock calculated surface energies (Jm^{-2}) of the unrelaxed and relaxed {001} surface

No. of Layers	Unrelaxed Surface Energy	Relaxed Surface Energy
5	4.046	3.697
7	4.044	3.542
9	-	3.459

Table 8.9 Comparison of surface energies (Jm^{-2}) with number of layers for the unrelaxed and Ramamoorthy relaxed {001} surfaces

The final surface to be investigated was the {011}, the lattice arrangement and stacking sequence of which are shown in figure 8.1(d) and 8.2(d). Both the 9 and 15 layer unrelaxed and relaxed slabs were considered, of which the latter was based on the LDA structures reported by Ramamoorthy *et al*⁸, and the corresponding Hartree-Fock surface and relaxation energies are given in table 8.10.

No of Layers	Unrelaxed Surface Energy	Relaxed Surface Energy	Relaxation Energy
9	2.882	2.642	0.24
15	2.882	2.607	0.275

Table 8.10 Comparison of surface energies (Jm^{-2}) with number of layers of the unrelaxed and Ramamoorthy relaxed {011} surface

8.3. Discussion

Hartree-Fock calculations, based on surface geometries derived by Ramamoorthy *et al*⁸ from LDA calculations, confirm the order of stability as {110}>{100}>{011}>{001} which is consistent with the experimental morphology. A detailed comparison of the unrelaxed and relaxed surface energies is shown in table 8.11.

Surface	Unrelaxed Surface Energy	Relaxed Surface Energy
{110}	2.734	1.918
{100}	2.970	2.229
{011}	2.882	2.607
{001}	4.044	3.542

Table 8.11 Comparison of the unrelaxed and relaxed surface energies (Jm^{-2}) of the Ramamoorthy relaxed surfaces

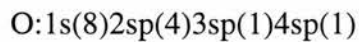
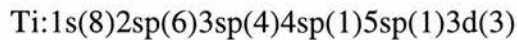
For the most stable of the surfaces, namely, the {110}, the order of Hartree-Fock energies for the different theoretically derived surface structures, that have been

proposed, is $HF < LDA < FLAPW$. However, the difference between the relaxed LDA and HF surface energies is only 0.15Jm^{-2} , leading to surface structures which are very similar, as shown in table 8.1. For these two structures all displacements agree in terms of their direction with the largest difference in magnitude being that for one of the Ti atoms in the first layer, which differed by only 0.05 \AA . Furthermore, as shown in table 8.1, the Hartree-Fock and LDA derived displacements are in good agreement with those obtained recently from surface x-ray diffraction¹⁵, the single exception being the displacement of the outermost bridging oxygen, O1 of figure 8.2(a).

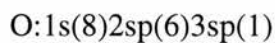
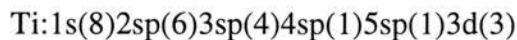
An interesting computational point to emerge is that the Hartree-Fock {110} surface energies appear to converge more quickly with slab thickness than LDA energies. The reasons for this are not obvious, but might arise, in part, from the more accurate treatment of the non local exchange interactions.

Table 8.1 shows that there are substantial differences between the Hartree-Fock and LDA derived displacements and those derived from FLAPW calculations. While these differences could result from the nature of the FLAPW methods, it seems likely that they result from the limited number of surface layers explicitly relaxed in the latter study.

The present calculations agree for the most part with previous *ab initio* periodic Hartree-Fock calculations carried out by Reinhardt and Hess¹⁰, where the principal difference between the two sets of calculation is the size of basis set used. In the present calculations, the Bloch functions were constructed from 23 atomic orbitals for Ti and 14 atomic orbitals for O of the type shown below,



where the numbers in brackets are the number of Gaussian functions which were used to represent each shell. This compares with the local basis set used by Reinhardt and Hess¹⁰ of the type,



Basis set size is an important factor in Hartree-Fock calculations and as a check on the present results a limited number of calculations were performed for the {110} surface based on an enlarged basis set of the type shown below,

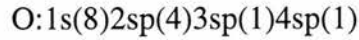
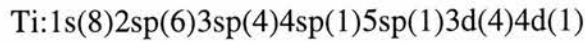


Table 8.12 compares the unrelaxed and relaxed {110} surface energies from which the influence of the basis set size is apparent. While there are differences of $\sim 0.2\text{Jm}^{-2}$ between the basis sets, this is unlikely to lead to any major conflict in the interpretation of experimental data which is generally of much lower accuracy than calculated surface energies.

Type of basis set	Unrelaxed Surface Energy	Relaxed Surface Energy	Relaxation Energy
Reinhardt & Hess	3.021	2.014	1.007
H-F	2.734	1.765	0.969
H-F enlarged	2.521	1.569	0.952

Table 8.12 Comparison of surface energies (Jm^{-2}) with basis set for the 9 layer {110} surface

Calculations for the {100} and {011} surface energies based on the geometries reported by Ramamoorthy *et al*⁸ find the energies of both to converge rapidly with slab thickness, with differences of 0.04Jm^{-2} between the 15 and 21 layer {100} slabs and also between the 9 and 15 layer {011} slabs. However, unlike the {011} surface, no Hartree-Fock optimisation of these surfaces is available for comparison. For the 15 layer slabs, the {100} surface is found to be more stable than the {011} in contradiction to the relative stability reported by Oliver *et al*¹³. Turning finally to the {001} surface, Hartree-Fock calculations were carried for unrelaxed and relaxed 5, 7 and 9 layer slabs. Here a relaxed surface structure was obtained by direct energy minimisation so that direct comparisons could be made with the LDA derived structure and that reported by Mason *et al*⁹ from LEED measurements. The three structures are compared in tables 8.5 to 8.7 and the Hartree-Fock energies for each compared in table 8.8, where the energy based on

the Hartree-Fock structure, 2.823Jm^{-2} , is lowest with a relaxation energy of 1.221Jm^{-2} . The energy differences between the Hartree-Fock optimised structure and those of Ramamoorthy *et al*⁸ and Mason *et al*⁹ are 0.72Jm^{-2} and 1.07Jm^{-2} respectively. The relaxation energy of the Hartree-Fock optimised structure is more than twice that between the unrelaxed and relaxed LDA surface, 0.502Jm^{-2} , and almost eight times that of the corresponding energy difference for the relaxed surface reported by Mason *et al*⁹, 0.158Jm^{-2} . It has been suggested that this relaxation might have been improved if more layers had been used in the initial investigation.

There are two main differences between the Hartree-Fock and LDA {001} surfaces structures. The first is the magnitude of the z displacement of the Ti atoms in the top two layers. Although these displacements occur in the same direction, the displacements of the LDA surface are approximately half the value of the Hartree-Fock surface. The second is the direction of the oxygen z displacement, as all oxygens in the LDA surface displace in the opposite direction to those in the Hartree-Fock relaxed structure.

8.4.Conclusion

The main conclusions of this chapter are: (1) that the order of the stability of the relaxed surfaces of TiO_2 , proposed by Ramamoorthy *et al*⁸ on the basis of LDA calculations, is confirmed to be $\{110\} > \{100\} > \{011\} > \{001\}$; (2) for the {110} surface the order of Hartree-Fock energies for different surface structures is HF optimised < LDA < FLAPW; (3) that the Hartree-Fock optimised {110} surface structure is both close to that derived from LDA calculations and to that deduced from surface x-ray diffraction¹⁵; the atomic displacements of which show good agreement with experiment; (4) that the surface energy calculated from Hartree-Fock calculations is dependent on the size of basis set used; (5) that convergence of surface energy with slab thickness is faster using Hartree-Fock calculations than density functional theory calculations; and that (6) theoretical calculations have an important role to play in surface structure determination.

References

1. K.Tennakone and U.S.Ketipearachi, *Applied Catalysis B:Environmental*, 1995, **5**, 343
2. K.Tennakone, C.T.K.Tilakaratne, I.R.M.Kottegoda, *Journal of Photochemistry and Photobiology A:Chemistry*, 1995, **87**, 177
3. A.Fujishma and K.Honda, *Nature*, **238**, 37, (1972).
4. J.P.Bucher, J.J. van der Klink and M.Graezel, *Journal of Physical Chemistry*, 1990, **94**, 1209
5. K.V.R.Chary, V.Vijayakumar and P.K.Rao, *Langmuir*, 1990, **6**, 1549
6. D.Gaskell, *Chemistry in Britain*, 1995, **31**, 430
7. D.Vogtenhuber, R.Podloucky, A.Neckel, S.G.Steinemann and A.J.Freeman, *Physical Review B*, 1994, **49**(3), 2099
8. M.Ramamoorthy, D.Vanderbilt and R.D.King-Smith, *Physical Review B*, 1994, **49**(23), 16721
9. C.G.Mason, S.P.Tear, T.N.Doust, G.Thornton, *Journal Physics: Condensed Matter*, 1991, **3**, 97
10. P.Reinhardt and B.A.Hess, *Physical Review B*, 1994, **50**(16), 12015
11. P.J.D.Lindan, N.M.Harrison, J.Holender, M.J.Gillan and M.C.Payne, *Surface Science*, 1996, **364**, 431
12. P.J.D.Lindan, N.M.Harrison, M.J.Gillan and J.A.White, *Physical Review B*, 1997, **55**(23), 15919
13. P.M.Oliver, G.W.Watson, E.T.Kelsey, S.C.Parker, *Journal of Materials Chemistry*, 1997, **7**(3), 563
14. J.Purton, D.W.Bullett, P.M.Oliver and S.C.Parker, *Surface Science*, 1995, **336**, 166
15. G.Charlton, P.B.Howes, C.L.Nicklin, P.Steadman, J.S.G.Taylor, C.A.Muryn, S.P.Harte, J.Mercer, R.McGrath, D.Norman, T.S.Turner and G.Thornton, *Physical Review Letters*, 1997, **78**(3), 495
16. W.C.Mackrodt - private communication
17. N.M.Harrison - private communication

Chapter 9

The Electron-Excess Gap States in TiO₂ Rutile

9.1. Introduction

The rutile polymorph of titanium dioxide is insulating in its stoichiometric form with a well defined electronic structure. The filled valence band consists mainly of oxygen 2p states and is separated from the empty conduction band of Ti 3d, 4s and 4p states by a gap of ~3eV. Experimental and theoretical studies have shown that deposition of thin metal overlayers, metal doping or the creation of oxygen vacancies on surfaces of TiO₂ all induce states within the band gap, resulting from excess electrons. These states have been observed at approximately 2.3eV above the valence band edge, that is ~0.7eV below the conduction band edge, and are frequently referred to as gap states. Knowledge of the electronic structure of these states under different defect conditions, such as the presence of oxygen vacancies or metal overlayers, is an important step towards understanding the mechanism of reactions involving TiO₂ in applications such as those mentioned in the previous chapter.

In 1981 Henrich and Kurtz¹ established experimentally that the defect free {110}, {100} and {001} surfaces of TiO₂ did not show any gap states, and that defects produced from fracturing these surfaces gave a small amount of emission in the gap. Since then, each experimental study on the stoichiometric surfaces has confirmed this observation^{2,3,4}. The most common experimental technique used to determine electronic structure, photoemission spectroscopy, was employed by Egdell *et al*⁵ in 1986 and Aiura *et al*⁶ in 1994 to investigate the oxygen deficient {110} surface. Electron energy loss spectroscopy (EELS) was used by Mohamed *et al*⁷ in 1988 to investigate the same surface. All three studies reported occupied states in the band gap at ~1eV below the conduction band edge. Aiura *et al*⁶ also found similar states for the oxygen deficient {001} surface, while Casanova *et al*³ published results of occupied gap states for the {100} oxygen deficient surface in 1991. More recently, Purdie *et al*⁸ used inverse and ultraviolet photoemission spectroscopy to show that the adsorption of potassium on a {100} surface gave a populated state in the band gap by charge transfer from K 4s to Ti 3d. The effect

on the electronic structure due to the presence of Nb doped thin films on TiO₂ was investigated by Okamura and Okushi⁹ in 1993 using isothermal capacitance transient spectroscopy and two gap states were observed. See *et al*¹⁰ compared thin films of Cu to Fe on the TiO₂ {110} surface, and showed that a gap state was only observed on Fe deposition as oxidation of Fe to Fe²⁺ and Fe³⁺ occurred.

A good illustration of the similar effects of metal monolayer and creation of surface oxygen vacancies on the electronic structure of TiO₂ was given by Mohamed *et al*⁷ in 1988 and Prabhakaran *et al*¹¹ in 1992. Using EELS Mohamed *et al*⁷ investigated the effect of evaporating a thin layer of titanium on the {110} surface, the resulting spectrum of which was identical to that of their oxygen deficient {110} surface. Prabhakaran *et al*¹¹ used resonance photoemission spectroscopy and showed that the adsorption of potassium on the {100} surface of TiO₂ resulted in occupied states at the same binding energy as the states associated with the oxygen deficient {100} surface.

Theoretical calculations have been carried out on non stoichiometric and perfect surfaces of TiO₂. The main area of study has been concerned with oxygen deficient surfaces, although one recent study by Glassford and Chelikowsky¹² was for Ru doped TiO₂ which showed gap states ~1eV above the valence band edge. For stoichiometric surfaces, theoretical results, for the most part, are in good agreement with experimental findings. For the non defective {110} surface, no gap states were found by Munnix and Schmeits using the scattering theoretic method,¹³ or by Wang and Xu¹⁴ using the tight binding extended Hückel theory. First principles calculations by Ramamoorthy *et al*¹⁵ and Goniakowski and Gillan¹⁶ based on the local density approximation (LDA) using pseudopotentials, FLAPW calculations by Vogtenhuber *et al*¹⁷ and spin restricted Hartree-Fock calculations by Reinhardt and Hess¹⁸ also confirmed this. The ideal {001} and {100} surfaces were also investigated by Wang and Xu¹⁴ and no gap states were observed. From a theoretical point of view the picture for the oxygen deficient {110} surface is not so clear. Wang and Xu¹⁴ found states ~0.7eV below the conduction band edge on removal of a surface bridging oxygen, as did Tsukada *et al*¹⁹ using the DV-X α cluster method. However, contrary to this, Munnix and Schmeits²⁰ only found gap states on removal of a sub surface oxygen, and none

on removal of a surface bridging oxygen. More recently, LDA calculations by Ramamoorthy *et al*¹⁵ on the oxygen deficient {110} surface found states at the edge of the conduction band, but not actually in the gap. However, recent plane wave local spin density (LSD) calculations by Lindan *et al*²¹ predicted gap states ~1.1eV above the valence band edge. Again using plane wave LSD calculations Manassidis *et al*²² predicted a broad continuum of states starting at the valence band upper edge of a reduced {110} surface of SnO₂, which is isostructural with TiO₂, with the excess electron density localised at the site of the oxygen vacancy. A similar electronic distribution was found by Ferrari and Pacchioni²³ for the reduced {100} surface of MgO. The oxygen deficient {001} surface of TiO₂ was investigated²⁴ using a tight binding approach, from which a tail of gap states were found which grew with increasing oxygen vacancy concentration. Confusion also exists for the oxygen deficient bulk as Ramamoorthy *et al*¹⁵, Halley *et al*²⁵ and Lindan *et al*²¹ all reported the presence of gap states, whereas Munnix and Schmeits²⁶ found no states within the band gap.

In summary, no gap states have been observed for the perfect surfaces of TiO₂, whereas, the presence of oxygen vacancies and certain metal overlayers have been found to produce occupied gap states. Theoretically, calculations predict the absence of gap states for stoichiometric surfaces, in accordance with experimental findings, but some disagreement exists over the electronic structure of the oxygen deficient {110} surface, and the oxygen deficient bulk. In view of this disagreement, and the importance of understanding the nature of the reduced state in TiO₂, *ab initio* Hartree-Fock calculations have been carried out on these structures.

9.2. Results

9.2.1 Non-defective bulk

Based on the previously calculated lattice parameters of 4.561 Å and 3.020 Å for a and c respectively the electronic structure of the non defective bulk was calculated using both UHF and RHF procedures. As expected the converged solutions were identical and confirmed the stoichiometric material to be a non magnetic wide band gap insulator. The calculated densities of states (DOS),

shown in figure 9.1, indicates that the valence band consists mainly of oxygen 2p states, notably at the upper edge, with a total band width of 7.7eV. It is separated from the mainly oxygen 2s band by a gap of 14eV. These compare with experimental values of ~6eV and ~14eV respectively which suggest that overall figure 9.1 is in good agreement with the experimentally measured bands of TiO_2 ⁴. Titanium 3d states contribute to both bands thus indicating the presence of partial covalent bonding. This is confirmed by the Mulliken population analysis, which lead to total charges of +2.8e and -1.4e for Ti and O respectively.

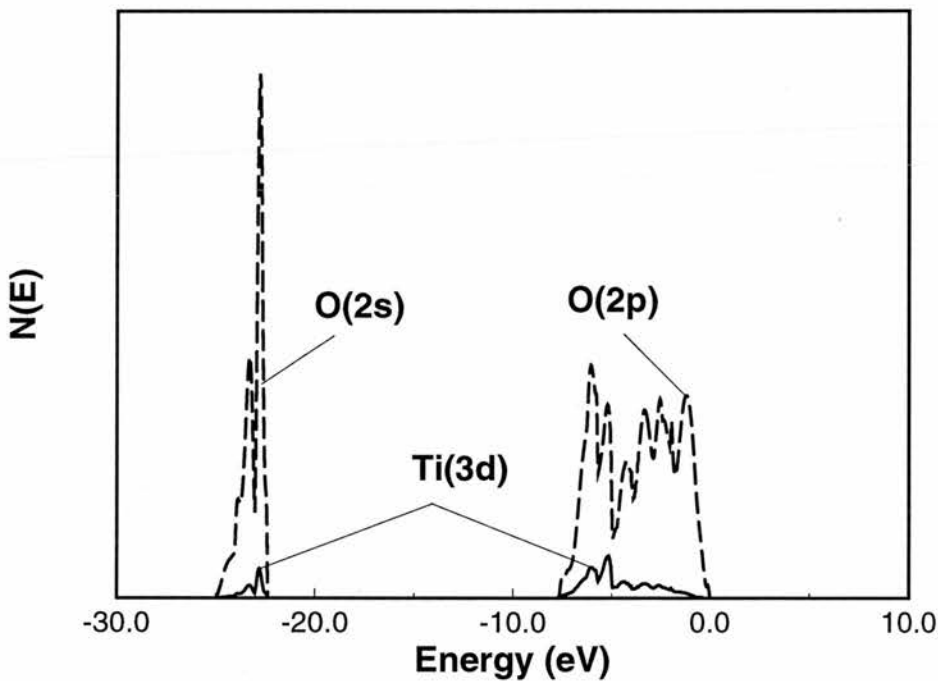


Figure 9.1 Calculated upper and lower valence band DOS of bulk TiO_2

9.2.2 Non-defective {110}, {100} and {001} surfaces

Figure 9.2 shows the calculated gap region of the non defective {001}, {100} and {110} surfaces and 3D bulk. While there are small differences, which result largely from different computational conditions, eg number of k points, it is clear that the surface DOS are broadly similar to that for the bulk. Small differences in atomic charge occur for the fully relaxed non defective slabs which are mainly associated with low coordination surface atoms. In particular, the charge on the outermost oxygens of the {100} and {110} slabs is decreased by ~0.2e with a

small amount of redistribution over all other atoms. The main difference in atomic charge for the {001} surface is an increase of $\sim 0.3e$ on to the outermost titanium atom. This is accompanied again by charge redistribution. However, the important point is that no states occur in the band gap for any of the non defective surfaces or the 3D bulk. This is in full agreement with previous experimental^{1,2,3,4} and theoretical^{13,14,15} studies.

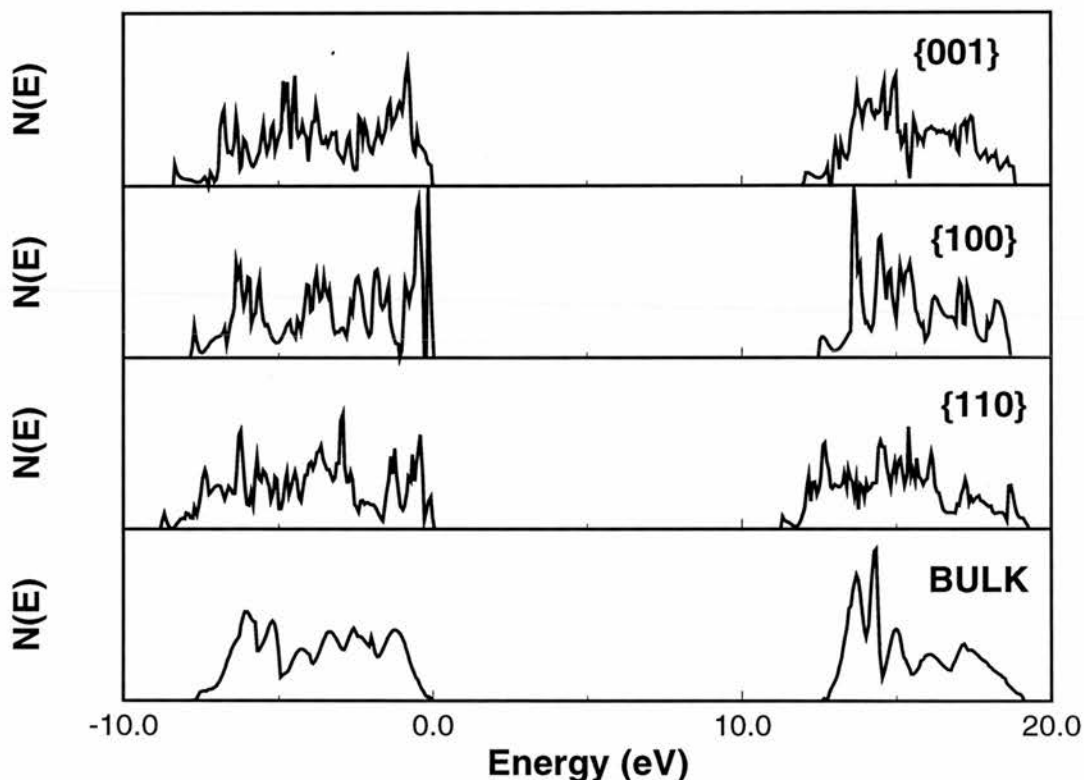


Figure 9.2 Calculated upper valence band DOS of the relaxed {110}, {100} and {001} surfaces of TiO_2 compared with the bulk

9.2.3 One electron addition

UHF calculations were carried out for a one electron addition to the 3D bulk, the {110} slab and the {100} slab. The symmetry of the systems was broken to allow, but not force, the localisation of spin and/or charge. No subsequent surface relaxations were carried out after electron addition. The second and third columns of tables 9.1 and 9.2 summarise the changes in total Mulliken charge (δq) and spin (δs) populations for the {110} and {100} surfaces respectively, which result from one electron addition.

Atom	1 electron addition		2 electron addition		oxygen vacancy	
	δq	δs	δq	δs	δq	δs
O(1)	0.25	0.00	0.57	0.01	-	-
Ti(1)	0.08	0.06	0.05	0.01	0.30	-1.01
Ti(2)	-0.06	0.00	0.29	0.99	0.37	1.00
O(2)	0.07	0.00	0.07	0.00	0.19	0.00
O(3)	0.07	0.00	0.07	0.00	0.19	0.00
O(4)	-0.06	0.00	0.00	0.00	0.03	-0.01
O(5)	-0.08	-0.04	-0.04	0.00	0.04	0.01
Ti(3)	-0.01	0.00	0.01	0.00	0.04	0.03
Ti(4)	0.39	0.98	0.01	0.00	0.00	0.00
O(6)	0.03	-0.01	-0.01	0.00	-0.02	0.00

Table 9.1 Changes in the total Mulliken population, $\delta q(e)$, and $\alpha - \beta$ spin population, $\delta s(e)$, resulting from 1 and 2 electron additions to and surface oxygen removal from a relaxed 9 layer {110} slab (Atom numbering corresponds to figure 8.2(a))

Atom	1 electron addition		2 electron addition		oxygen vacancy	
	δq	δs	δq	δs	δq	δs
O(1)	0.35	0.00	0.66	0.00	-	-
Ti(1)	0.00	0.03	0.31	1.00	0.85	1.72
O(2)	0.03	-0.01	0.04	-0.01	0.01	-0.18
O(3)	-0.07	-0.02	-0.01	0.00	0.16	-0.06
Ti(2)	0.38	0.98	-0.02	0.01	0.30	-0.97

Table 9.2 Changes in the total Mulliken population, $\delta q(e)$, and $\alpha - \beta$ spin populations, δs , resulting from 1 and 2 electron additions to and surface oxygen removal from a relaxed 9 layer {100} slab (Atom numbering corresponds to figure 8.2(b))

For the {100} and {110} slabs the charge associated with the added electron appears mainly on one oxygen atom at the surface and one titanium in the bulk. Here the term 'bulk' refers to the atoms in the middle layers of the slab, which in the non defective case have electron distributions which are identical to those of the 3D bulk. The {100} slab contains an additional charge of 0.35e on O(1) at the surface, and 0.38e on Ti(2) in the bulk, where the numbering of the atoms refers to figure 8.2(b). A slight redistribution of charge occurs throughout the remaining atoms of the slab. Similarly for the {110} slab, additional charges of 0.25e and 0.39e localise at O(1) of the surface and Ti(4) of the bulk respectively. For comparison, the addition of one electron to the 3D bulk results in 0.48e localising on one titanium atom with the remaining 0.52e being equally distributed over the remainder of the unit cell. Analyses of the corresponding spin densities indicate localisation of the added spin solely at the Ti sites, with spin populations of 0.98 on Ti(2) of the {100} surface, 0.98 on Ti(4) of the {110} surface and 1.00 in the 3D bulk, with very little dispersion of spin elsewhere.

The calculated DOS for one electron addition are shown in figure 9.3. The presence of new states above the valence band edge is clearly evident in all cases. These states are not part of the conduction band, which although not shown here, lies at higher energy above the electron excess states. These new gap states are 1.7eV, 1.3eV and 1.1eV above the valence band edges of the {100} slab, {110} slab and 3D bulk respectively. These values are close to the experimentally determined position which is ~2eV above the valence band edge.

A more detailed plot of the DOS for a one electron addition to the {110} surface is shown in figure 9.4. In the upper panel, the spin projected DOS shows quite clearly a near complete spin pairing of the oxygen 2p band and the spin polarised nature of the gap states. The lower panel shows that exactly the same type of spin localisation occurs for gap states in the 3D bulk.

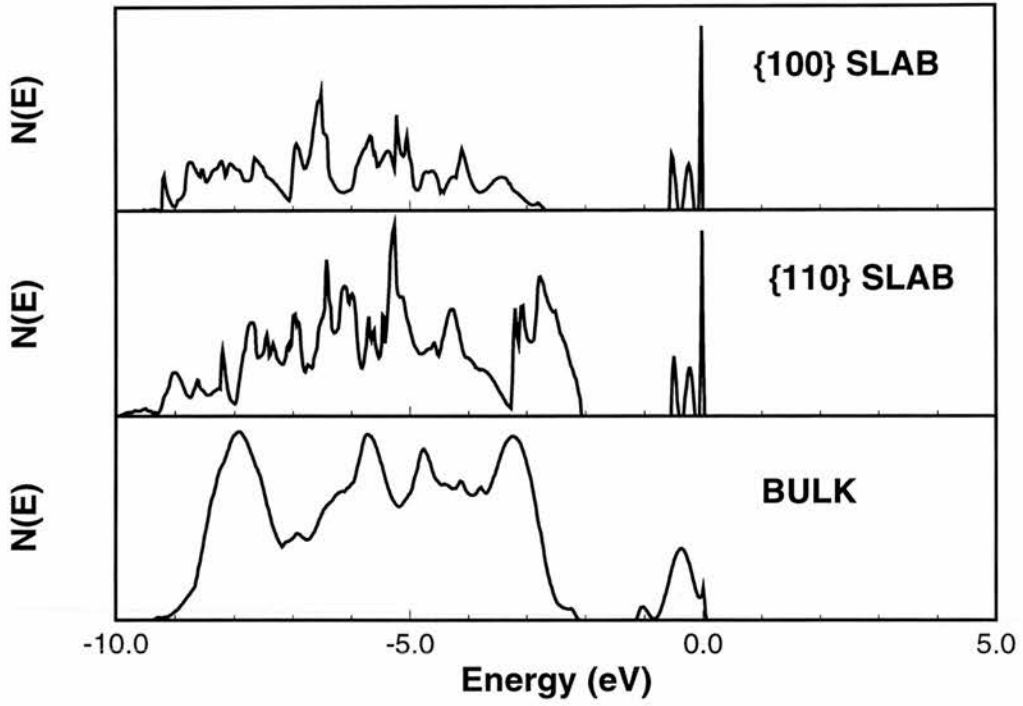


Figure 9.3 Calculated upper valence band DOS of the 3D bulk, {110} and {100} slab one electron addition states.

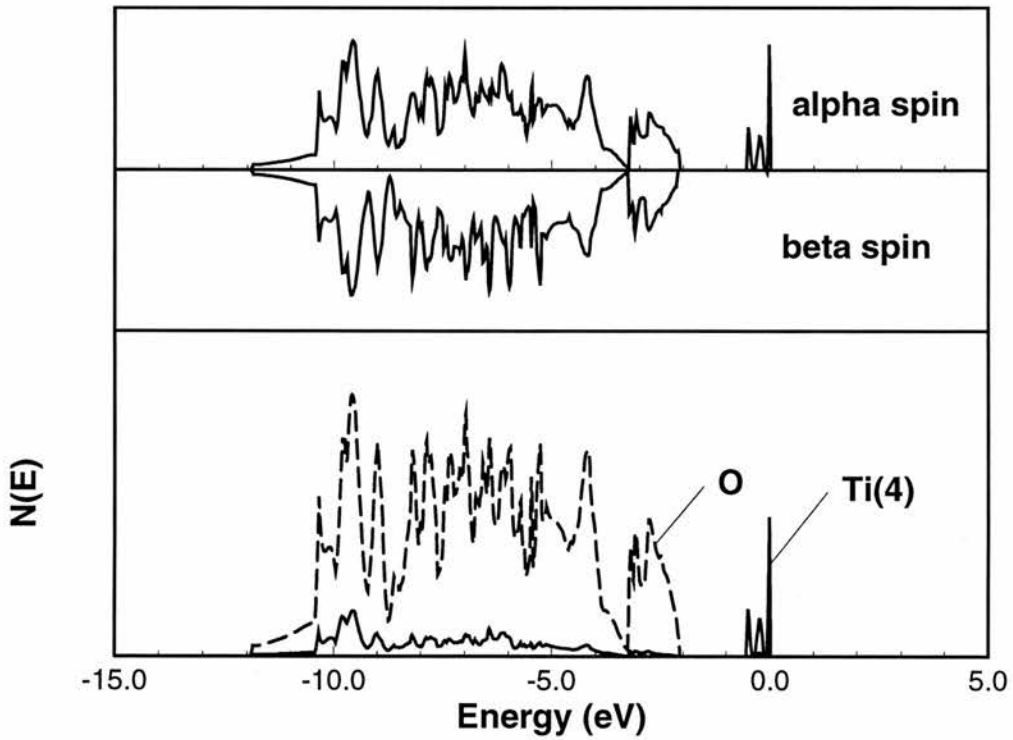


Figure 9.4 Calculated upper valence band spin- and atom-projected DOS of {110} slab one electron addition

9.2.4 Two electron addition

UHF calculations were also carried out for a two electron addition to the {001}, {100} and {110} slabs, where in general, the majority addition of charge occurs on the atoms of the surface layers. For the {001} slab, with the relaxed structure of Ramamoorthy *et al*²⁷, additional density was found on all surface atoms, with a net loss in the lower layers and the bulk. Unrelaxed and relaxed {100} slabs with the Ramamoorthy structure show almost identical charge redistribution. Again, additional charge is found on the surface atoms, with $\sim 0.6e$ on O(1) and $\sim 0.3e$ on Ti(1), with depletion in the bulk, see table 9.2 for details. However, a significant difference occurs in the DOS. The middle panel of figure 9.5 shows that lattice relaxation opens up a gap of $\sim 0.7eV$ at the valence band upper edge leading to occupied states. Similar results were obtained for the {110} slab, where most of the additional charge in the unrelaxed structure resides at O(1) and Ti(1) of the surface layers. Relaxation leads to a redistribution of added surface density which now localises at O(1) and Ti(2) as shown in table 9.1 previously. As in the case of the {100} slab, relaxation opens up a gap with occupied states $\sim 1.43eV$ above the valence band edge, as shown in figure 9.5. In all cases, the spin associated with the addition of two electrons localises at a single surface Ti site which is Ti(1) for the {001}, {100} and unrelaxed {110} slabs and Ti(2) for the relaxed {110} slab.

The {110} slab was investigated in more detail, and the spin and atom projected DOS shown in figure 9.6. As in the case of one electron addition, near complete spin pairing of the oxygen 2p band is evident from the near mirror image of the alpha and beta states. The gap states, on the other hand, which lie above the O(2p) states are unquestionably spin polarised. The atom projected DOS reveal that these states are largely associated with Ti(2).

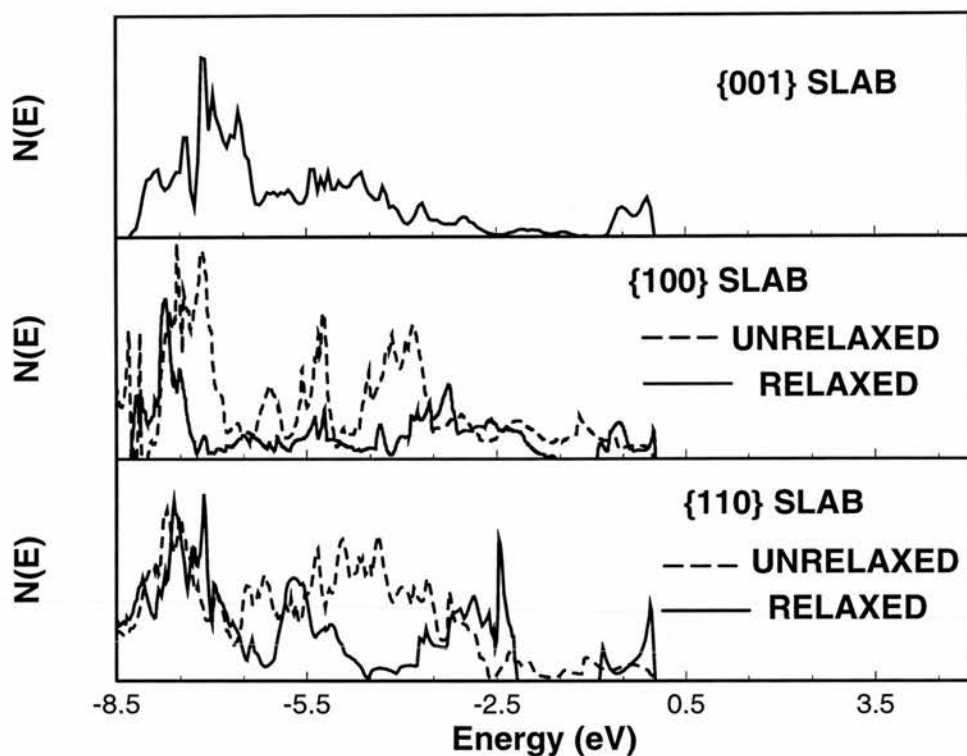


Figure 9.5 Calculated upper valence band DOS of {110}, {100} and {001} slab two electron addition states

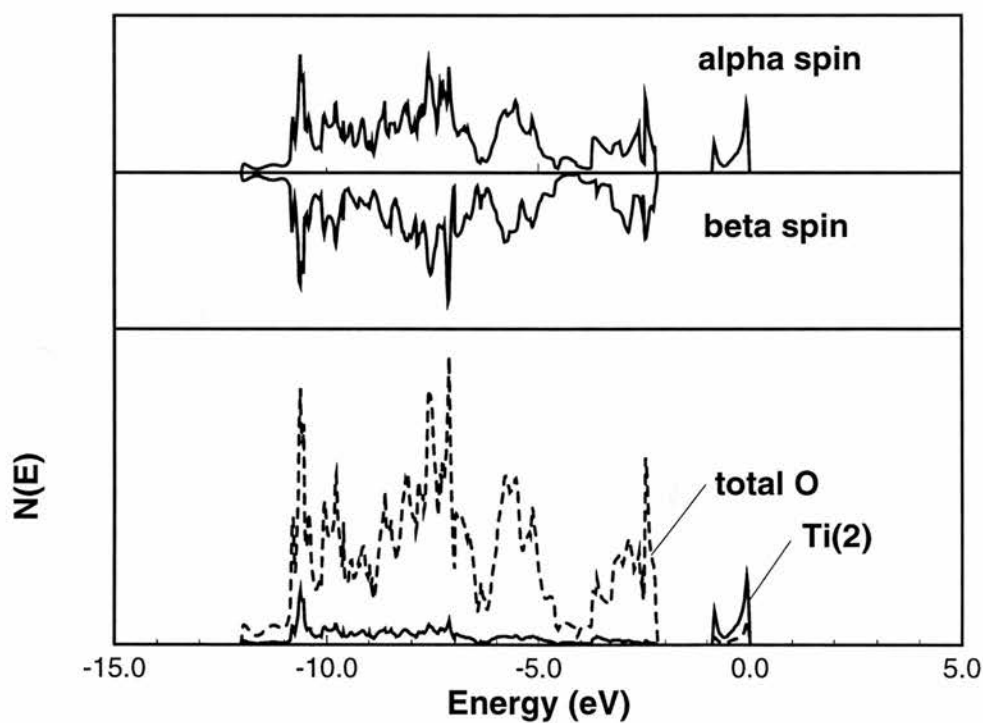


Figure 9.6 Calculated upper valence band spin- and atom-projected DOS of {110} slab two electron addition states

9.2.5 Oxygen deficient bulk and surface

The reduced bulk structure was constructed by the removal of one oxygen atom from Ti_8O_{16} supercells, for which two types of calculation were carried out. The first included the complete oxygen basis set at the vacancy position to allow for the possible localisation of excess electron density at the vacancy site: the second type of calculation neglected the vacancy functions altogether. For both types of calculation converged magnetic insulating solutions were obtained with the former lower in energy by 1.36eV. Table 9.3 contains details of the Mulliken population analyses of these solutions, which not surprisingly, show somewhat different electron distributions. The inclusion of vacancy site functions leads to substantial localisation of electron density at the vacancy at the expense of the next nearest neighbour Ti atoms. At the nearest neighbour Ti sites, on the other hand, both the charge and spin density populations are nearly identical for the two types of calculation. The corresponding valence band DOS are shown in figure 9.7 where gap states are predicted for both types of calculation despite evident differences between the electron distributions.

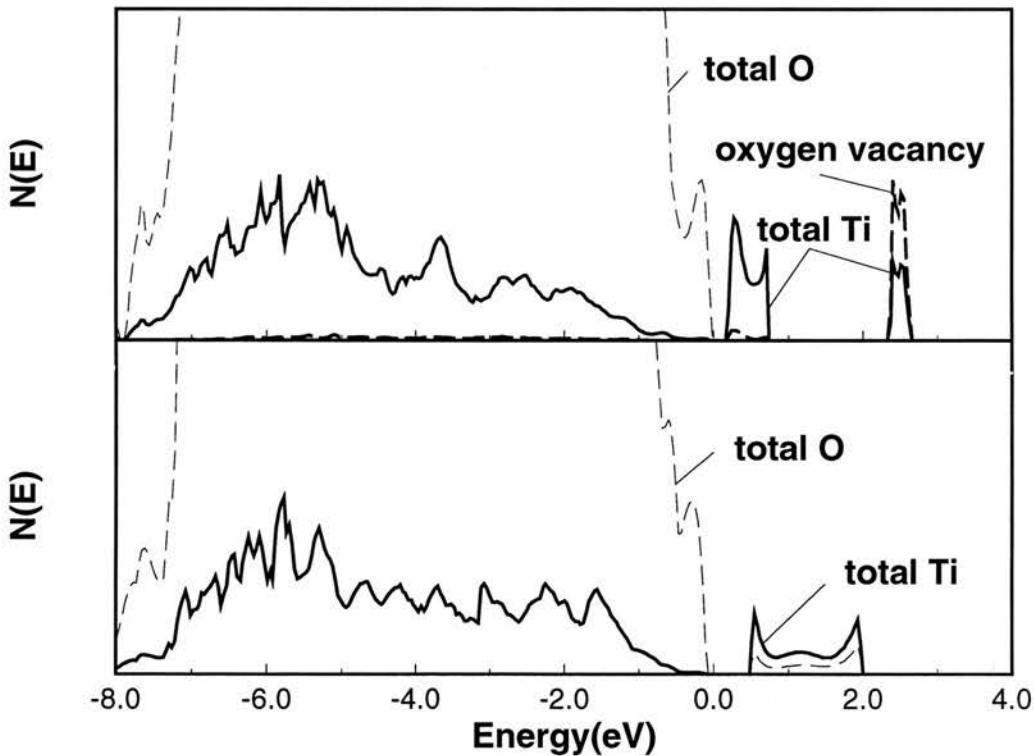


Figure 9.7 Calculated upper valence band DOS of Ti_8O_{15} : upper panel with vacancy functions; lower panel without vacancy functions.

A similar approach was adopted for the reduced {110} surface, where two types of calculation were also carried out, with and without oxygen functions at the site of the surface oxygen vacancy. The redistribution of Mulliken charge at the surface was found to be similar to that of the reduced bulk, but in this case the solution without vacancy functions was found to be lower in energy. The explanation for this is that, for reasons which remain unclear, the calculations which included vacancy functions constantly converged to an excited state. This was subsequently shown by more extensive calculations which were carried out at Daresbury by J. Muscat and N.M. Harrison²⁸. For this reason, all subsequent calculations for reduced surfaces were carried out without the addition of any vacancy functions.

$\delta q / \delta s$	with vacancy functions	without vacancy functions
δq (vac)	-0.81	-
δs (vac)	0.70	-
$\delta q(\text{Ti}(\mathbf{n}))$	-0.41	-0.53
$\delta s(\text{Ti}(\mathbf{n}))$	1.05	1.01
$\delta q(\text{Ti}(\mathbf{nn}))$	-0.08	-0.46
$\delta s(\text{Ti}(\mathbf{nn}))$	0.25	1.00

Table 9.3 Differences in the total Mulliken population, δq and $\alpha - \beta$ spin population, δs , between Ti_8O_{15} with and without vacancy functions.

The most extreme case of surface oxygen deficiency is the removal of a complete surface oxygen layer from a {100} slab, O(1) in the notation of figure 8.2(b), leading to an excess of $\sim 2.4e$ per slab unit cell. This redistributes mainly at Ti(1), in an approximate high spin d^2 configuration, with much less at Ti(2) and only a minor increase at O(3). A full analysis is detailed in columns 6 and 7 of table 9.2. The oxygen deficient {110} slab was considered in greater detail. Here the reduced surface corresponds to complete removal of bridging oxygens, O(1) in the notation of figure 8.2(a). In view of the experimental importance of this surface, a complete structural relaxation was carried out by direct energy minimisation. Small inward displacements of 0.02 Å and 0.01 Å were found for

the five fold (Ti(1)) and four fold (Ti(2)) coordinated Ti atoms respectively. Both surface oxygens, O(2) and O(3) relaxed outward by 0.39 Å. These relaxations were similar to the values found by Ramamoorthy *et al*¹⁵ which were 0.05 Å, 0.13 Å and 0.35 Å respectively. This relaxed structure is lower in energy by 0.13eV than that obtained from LDA calculations¹⁵, with a relaxation energy of 5.87eV compared with the unrelaxed structure. Mulliken population analyses show that the oxygen deficient {110} slab differs from the oxygen deficient {100} slab and 3D bulk in the distribution of charge after the creation of an oxygen vacancy. On removal of a surface oxygen from a {110} slab the electron excess, ~1.3e is confined to the top two surface layers, with the majority of the charge not confined to a single Ti, as found for the {100} slab, but redistributed throughout the surface, with 0.30e on Ti(1), 0.37e on Ti(2) and 0.19e on O(2) and O(3). However, the most significant difference is found in the spin analysis for oxygen deficient {110}, where UHF calculations predicted an antiferromagnetic arrangement of the electron configurations at Ti(1) and Ti(2). In each case, δs was close to ± 1 and very little spin dispersion was found elsewhere. The DOS corresponding to these oxygen deficient structures are shown in figure 9.8.

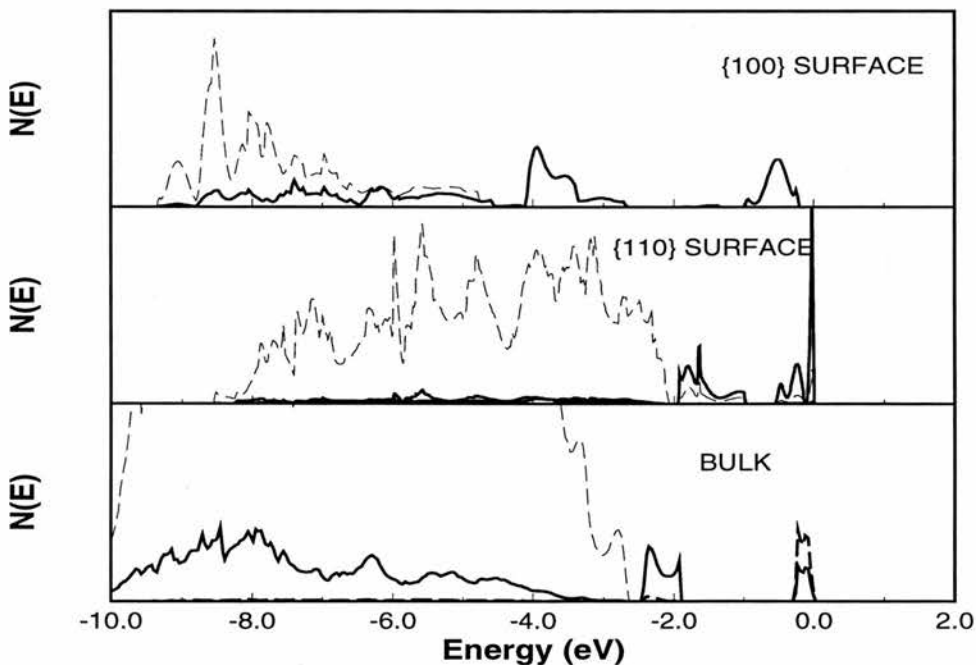


Figure 9.8 Calculated upper valence band DOS of 3D bulk, {110} and {100} surface oxygen deficient states

Once again, the most significant features of the reduced structure are the appearance of gap states $\sim 1.6\text{eV}$, $\sim 0.5\text{eV}$ and $\sim 2.25\text{eV}$ above the valence band upper edges of the $\{100\}$ and $\{110\}$ surfaces and 3D bulk respectively. A more detailed spin and atom projected DOS for the $\{110\}$ slab is shown in figure 9.9. Here the atom projection illustrates the essentially Ti 3d nature of the gap states, although a small contribution from oxygen 2p states exists. The spin projection shows incomplete spin pairing of the O(2p) band, but clearly illustrates the alpha and beta spin polarisation of these two gap states.

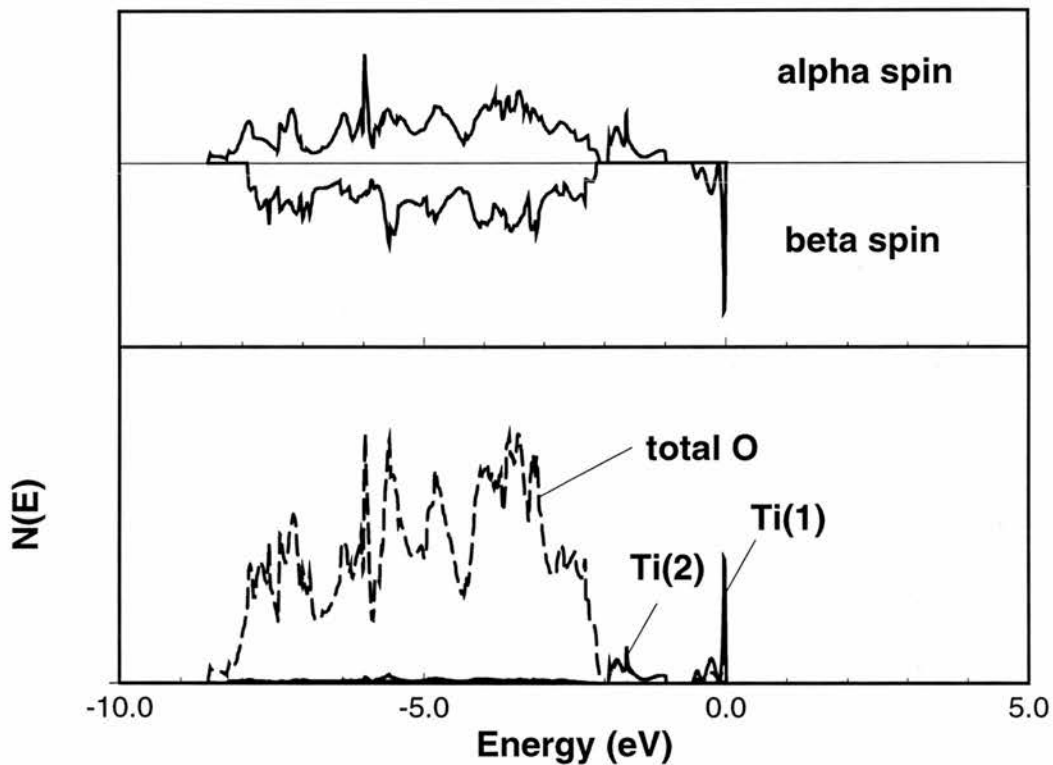


Figure 9.9 Calculated upper valence band spin- and atom-projected DOS of oxygen deficient $\{110\}$

9.3. Discussion

All electron, periodic Hartree-Fock calculations have been carried out to determine the electronic structure of the stoichiometric and reduced 3D bulk and stoichiometric and defective $\{110\}$, $\{100\}$ and $\{001\}$ surfaces of TiO_2 . For the non defective structures no gap states were found in agreement with previous experimental^{1,2,3,4} and theoretical studies^{13,14,15}. In every case UHF calculations

lead to insulating solutions for the reduced surface whereas the corresponding RHF calculations gave solutions which were higher in energy and in most cases conducting. For the {110} slab, the addition of an electron to the bulk, or to the surface, or the creation of a surface oxygen vacancy, lead to occupied states within the band gap, as shown in figure 9.10.

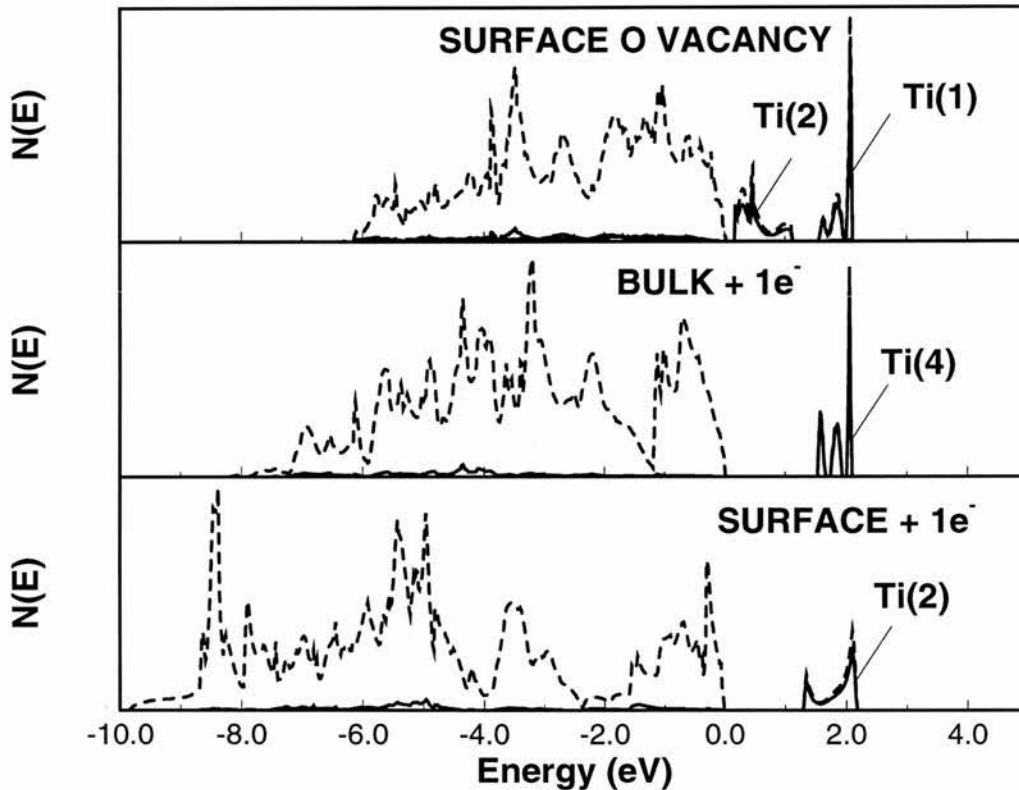


Figure 9.10 Comparison of calculated upper valence band DOS of the {110} slab one and two electron addition and surface oxygen deficient states

This is in agreement with previous experimental^{5,6,7}, and some theoretical^{15,19} findings for the oxygen deficient {110} surface. Spin polarisation is particularly important and is evident in every case where the electron configuration differs from that of the stoichiometric material. It should be noted that UHF theory allows for the effects of spin polarisation, which many other theoretical methods fail to address. This issue was investigated recently by Lindan *et al*²¹ using spin polarised and non spin polarised plane wave pseudopotential density functional theory calculations on the reduced {110} surface of TiO₂ rutile. It was found that

the non spin polarised calculation resulted in a solution 2.77eV higher in energy than the corresponding spin polarised solution which failed to detect any gap states. The exclusion of spin polarisation could account for the findings of Munnix and Schmeits²⁰ who only found gap states resulting from a sub surface oxygen vacancy and Ramamoorthy *et al*¹⁵ who found the states to be conducting, and thus appearing at the edge of the conduction band.

Figure 9.11 shows the calculated DOS of the defective {100} surface. As found previously for the defective {110} slab, gap states were observed both for the reduced surface and that containing electron excess.

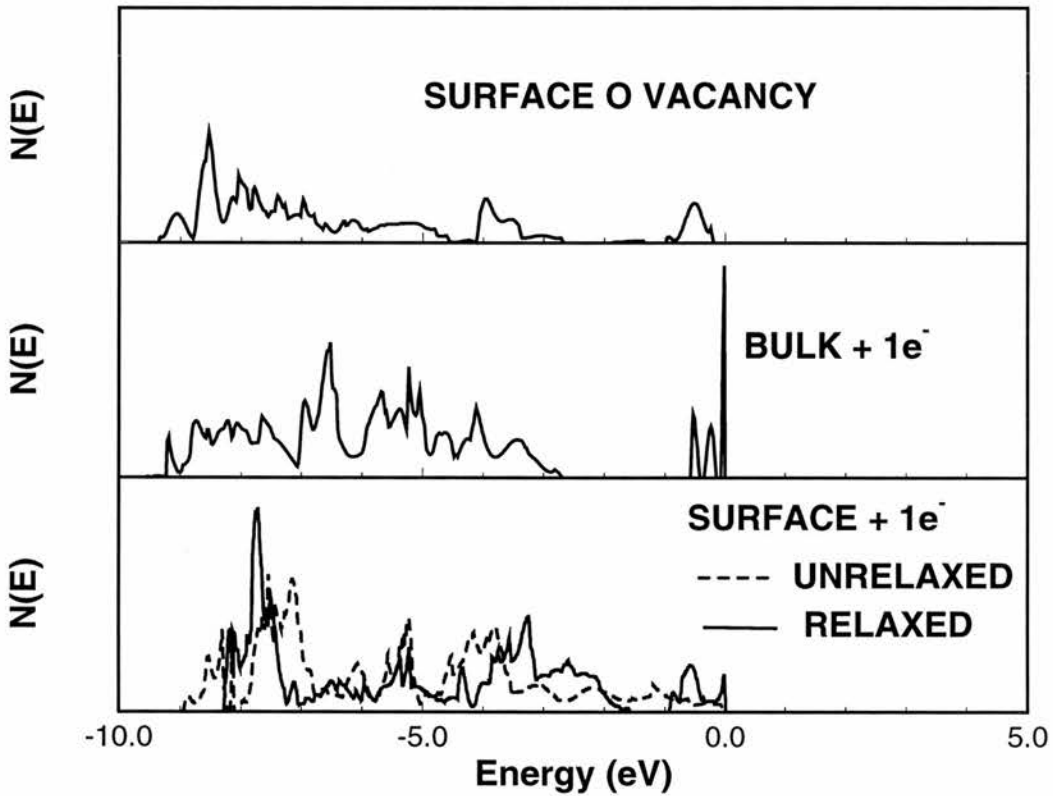


Figure 9.11 Comparison of calculated upper valence band DOS of the {100} slab one and two electron addition and surface oxygen deficient states

Also for the 3D bulk it was found that the creation of an oxygen vacancy resulted in the emergence of a gap state. This is in agreement with Ramamoorthy *et al*¹⁵ using LDA and Halley *et al*²⁵ using tight binding calculations, but in disagreement with Munnix and Schmeits²⁶ using the scattering theoretic method,

who found no states in the gap. The electron excess associated with the reduced bulk is localised at the site of the oxygen vacancy, the location of electron excess previously reported for reduced SnO_2 ¹⁶ and MgO by Manassidis *et al*²², but contrary to Lindan *et al*²¹ who found the gap states to be localised in Ti(3d) orbitals surrounding the oxygen vacancy.

9.4. Conclusion

The main conclusions of this chapter are that UHF calculations find: (1) that for the non defective bulk and surfaces of TiO_2 there are no gap states; (2) gap states for the reduced and electron excess bulk and surfaces of TiO_2 ; (3) that all gap states are insulating; (4) that for the surfaces, these gap states are spin polarised in Ti(3d¹) or Ti (3d²) configurations; and (5) that in the reduced bulk the gap states are associated mainly with electron density at the oxygen vacancy.

References

1. Henrich and Kurtz, *Physical Review B*, 1981, **23**(12), 6280
2. A.K.See, M.Thayer and R.A.Bartynski, *Physical Review B*, 1993, **47**(20), 13722
3. K.Prabhakaran, R.Casanova and G.Thornton, *Journal of Physics: Condensed Matter*, 1991, **3**, S91
4. V.E. Henrich, *Reports of Progress in Physics*, 1985, **48**, 1494
5. R.G. Egdell, S. Eriksen and W.R.Flavell, *Solid State Communications*, 1986, **60**(10), 835
6. Y.Aiura, Y.Nishihara, Y.Haruyama, T.Komeda, S.Kodaira, Y.Sakisaka, T.Maruyame and H.Kato, *Physica B*, 1994, **194-196**, 1215
7. M.H. Mohamed, H.R. Sadeghi and V.E. Henrich, *Physical Review B*, 1988, **37**(14), 8417
8. D. Purdie, B. Reihl, A. Thomas, P.J. Hardman, C.A. Muryn and G. Thornton, *Journal De Physique IV*, 1994, **4**, C9-163
9. T. Okamura, and H. Okushi, *Japanese Journal of Applied Physics*, 1993, **32**, L454
10. A.K. See, M. Thayer and R.A. Bartynski, *Physical Review B*, 1994, **50**(16), 12064
11. K. Prabhakaran, D. Purdie, R. Casanova C.A. Muryn, P.J. Hardman, *Physical Review B*, 1992, **45**(12), 6969
12. K.M. Glassford and J.R. Chelikowsky, *Physical Review B*, 1993, **47**(19), 12550
13. S.Munnix, M.Schmeits, *Physical Review B*, 1983, **28**(12), 7342
14. C.R.Wang and Y.S.Xu, *Surface Science*, 1989, **219**, L537
15. M.Ramamoorthy, D.Vanderbilt and R.D.King-Smith, *Physical Review B*, 1994, **49**(11), 7709
16. J.Goniakowski and M.J.Gillan, *Surf. Science*, 1996, **350**, 145
17. D.Vogtenhuber, R.Podloucky, A.Neckel, S.G.Steinemenn and A.J.Freeman, *Physical Review B*, 1994, **49**, 2099
18. P.Reinhardt and B.A.Hess, *Phys.Rev. B*, 1994, **50**, 12015

19. M.Tsukada, H.Adachi, C.Satoko, *Progress in Surface Science*, 1983, **14**(2), 113
20. S.Munnix, M.Schmeits, *Journal of Vacuum Science Technology A*, 1987, **5**(4), 910
21. P.J.D.Lindan, N.M.Harrison, M.J.Gillan and J.A.White, *Physical Review B*, 1997, **55**(23), 15919
22. I.Manassidis, J.Goniakowski, L.N.Kantorovich and M.J.Gillan, *Surf.Sci.*, 1995, **339**, 258
23. A.M.Ferrari and G.Pacchioni, *J.Phys.Chem.*, 1995, **99**, 17010
24. N.Tit, J.W.Halley and M.T.Michalewicz, *Surface and Interface Analysis*, 1992, **18**, 87
25. J.W.Halley, M.T.Michalewicz and N.Tit, *Physical Review B*, 1990, **41**(14), 10165
26. S.Munnix, M.Schmeits, *Solid State Communications*, 1984, **50** (12), 1087
27. M.Ramamoorthy, D.Vanderbilt and R.D.King-Smith, *Physical Review B*, 1994, **49**(23), 16721
28. J.Muscat and N.M.Harrison - private communication

Appendix

This appendix contains details of the exponents and contraction coefficients of the Li, O, Ti, Mn and Fe basis functions, tables 1-5 respectively, which have been used throughout this thesis.

Shell Type	Exponents	Coefficients	
		s	p
1s	840.0	0.00264	0.0
	217.5	0.00850	0.0
	72.3	0.03350	0.0
	19.66	0.18240	0.0
	5.044	0.63790	0.0
	1.5	1.0	0.0
2sp	0.51	1.0	1.0

Table 1. The exponents (bohr^{-2}) and contraction coefficients of the Gaussian functions used to represent the Li basis set

For O and Ti, enlarged basis sets were used which were simply constructed from the same inner shells as the normal basis sets but with additional outer shells. For example, the enlarged basis set for O was constructed from the same 1s 2sp 3sp shells as the normal basis set plus new 4sp and 3d shells, the exponents and contraction coefficients of which are shown at the bottom of table 2. Similarly for Ti, its enlarged basis set was constructed from the same 1s 2sp 3sp 4sp 5sp shells as the normal basis plus new 3d and 4d shells, the exponents and contraction coefficients of which are shown at the bottom of table 3.

Shell Type	Exponents	Coefficients	
		s	p / d
1s	8020.0	0.00108	0.0 / 0.0
	1338.0	0.00804	0.0 / 0.0
	255.4	0.05324	0.0 / 0.0
	69.22	0.1681	0.0 / 0.0
	23.9	0.3581	0.0 / 0.0
	9.264	0.3855	0.0 / 0.0
	3.851	0.1468	0.0 / 0.0
	1.212	0.0728	0.0 / 0.0
2sp	49.43	-0.00883	0.00958 / 0.0
	10.47	-0.0915	0.0696 / 0.0
	3.235	-0.0402	0.2065 / 0.0
	1.217	0.379	0.347 / 0.0
3sp	0.4763	1.0	1.0 / 0.0
4sp	0.176	1.0	1.0 / 0.0
4sp	0.20	1.0	1.0 / 0.0
3d	0.570	0.0	0.0 / 1.0

Table 2. The exponents (bohr^{-2}) and contraction coefficients of the Gaussian functions used to represent the O basis sets

Shell Type	Exponents	Coefficients	
		s	p
1s	225338	0.000228	0.0
	323215	0.001929	0.0
	6883.61	0.0111	0.0
	1802.14	0.05	0.0
	543.063	0.1701	0.0
	187.549	0.369	0.0
	73.2133	0.4033	0.0
	30.3718	0.1445	0.0
2sp	554.042	-0.0059	0.0085
	132.525	-0.0683	0.0603
	43.6801	-0.1245	0.2124
	17.2243	0.2532	0.3902
	7.2248	0.6261	0.4097
	2.4117	0.282	0.2181
3sp	24.4975	0.0175	-0.0207
	11.4772	-0.2277	-0.0653
	4.4653	-0.7946	0.1919
	1.8904	1.0107	1.3778
4sp	0.8126	1.0	1.0
5sp	0.3297	1.0	1.0
3d	7.935	0.1127	0.0
	1.8324	0.3927	0.0
	0.4681	0.5206	0.0
3d	16.2685	0.0675	0.0
	4.3719	0.2934	0.0
	1.464	0.5658	0.0
	0.5485	0.545	0.0
4d	0.26	1.0	0.0

Table 3. The exponents (bohr^{-2}) and contraction coefficients of the Gaussian functions used to represent the Ti basis sets

Shell Type	Exponents	Coefficients		
		s	p	d
1s	292600.0	0.000227	0.0	0.0
	42260.0	0.0019	0.0	0.0
	8947.0	0.0111	0.0	0.0
	2330.0	0.0501	0.0	0.0
	702.0	0.1705	0.0	0.0
	242.9	0.3691	0.0	0.0
	94.95	0.4035	0.0	0.0
	39.58	0.1437	0.0	0.0
2sp	732.1	-0.0053	0.0086	0.0
	175.6	-0.0673	0.0612	0.0
	58.51	-0.1293	0.2135	0.0
	23.13	0.2535	0.4018	0.0
	9.754	0.6345	0.4012	0.0
	3.454	0.2714	0.2222	0.0
3sp	38.39	0.0157	-0.0311	0.0
	15.44	-0.2535	-0.0969	0.0
	6.178	-0.8648	0.2563	0.0
	2.824	0.9337	1.655	0.0
4sp	1.209	1.0	1.0	0.0
5sp	0.4986	1.0	1.0	0.0
3d	22.59	0.0	0.0	0.0708
	6.167	0.0	0.0	0.3044
	2.064	0.0	0.0	0.5469
	0.7401	0.0	0.0	0.5102
4d	0.249	0.0	0.0	1.0

Table 4. The exponents (bohr^{-2}) and contraction coefficients of the Gaussian functions used to represent the Mn basis set

Shell Type	Exponents	Coefficients		
		s	p	d
1s	315400	0.000227	0.0	0.0
	45690	0.0019	0.0	0.0
	9677	0.0111	0.0	0.0
	2521	0.0501	0.0	0.0
	759.7	0.1705	0.0	0.0
	263.0	0.3692	0.0	0.0
	102.8	0.4033	0.0	0.0
	42.97	0.1434	0.0	0.0
2sp	798.3	-0.0052	0.0085	0.0
	191.2	-0.068	0.0608	0.0
	63.69	-0.1314	0.2114	0.0
	25.36	0.2517	0.3944	0.0
	10.73	0.6433	0.398	0.0
	3.764	0.2825	0.2251	0.0
3sp	48.14	0.0122	-0.0215	0.0
	17.46	-0.2278	-0.085	0.0
	6.997	-0.8801	0.201	0.0
	3.079	0.9755	1.302	0.0
4sp	1.314	1.0	1.0	0.0
5sp	0.5532	1.0	1.0	0.0
3d	30.48	0.0	0.0	0.0583
	8.692	0.0	0.0	0.2591
	3.101	0.0	0.0	0.5162
	1.171	0.0	0.0	0.5656
4d	0.4298	0.0	0.0	1.0

Table 5. The exponents (bohr^{-2}) and contraction coefficients of the Gaussian functions used to represent the Fe basis set

Publications

Based on this thesis a number of papers have been published or are in press.

Cation valence charge states of MnFe_2O_4 : An *ab initio* Hartree-Fock study

W.C.Mackrodt and E-A.Simson, *Journal of the Chemical Society, Faraday Transactions*, 1996, **92**(12), 2043

First-principles Hartree-Fock description of the electronic structure and magnetism of hole and electron addition in MnO

W.C.Mackrodt and E-A.Williamson, *Journal of Physics: Condensed Matter*, 1997, **9**, 6591

First-principles description of the valence charge states in rutile MnO_2

W.C.Mackrodt and E-A.Williamson, *Journal of the Chemical Society, Faraday Transactions*, 1997, **93**(18), 3295

An *ab initio* Hartree-Fock study of the electron-excess gap states in oxygen-deficient rutile TiO_2

W.C.Mackrodt and E-A.Simson, N.M.Harrison, *Surface Science*, 1997, **384**(1-3), 192

First-principles description of the valence states in manganese oxides

W.C.Mackrodt and E-A.Williamson, *Berichte der Bunsen-Gesellschaft für Physikalische Chemie*, 1997, **101**(9), 1215

First-principles Hartree-Fock description of the electronic structure of monoclinic $\text{C2/m Li}_x\text{MnO}_2$ ($1 \geq x \geq 0$)

W.C.Mackrodt, E-A.Williamson, *Philosophical Magazine B*, - in press

A First-principles Hartree-Fock description of MnO at high pressures

W.C.Mackrodt, E-A.Williamson D.Williams and N.L.Allan, *Philosophical Magazine B*, - in press